AN ABSTRACT OF THE THESIS OF

Jeromy W. Jenks for the degree of Master of Science in Mechanical Engineering presented on July 20, 2007.

Title: An Experimental Study of Ammonia-Water Bubble Absorption in a Constrained Microscale Film

Abstract approved:

Vinod Narayanan

An experimental study of absorption of ammonia into a constrained thin film of ammonia-water solution is presented. A large aspect ratio microchannel with one of its walls formed by a porous material is used to constrain the thickness of the liquid film. Experiments were performed at a pressure of 1, 2.5 and 4 bar absolute and a fixed weak solution inlet temperature. Weak solution flow rates were varied from 10 to 30 g/min, inlet mass concentrations from 0 to 15 percent, and gas flow rates between 1 and 3 g/min. Six geometries, including three smooth-bottom-walled channels of differing depths and three channels with structured bottom walls are considered. Results indicate that for identical rates of vapor absorption, the overall heat transfer coefficient for the 400 μm smooth microchannel is significantly larger than of the 150 μm and 1500 μm smooth channels. For the 150 μm channel, the largest overall heat and mass transfer coefficients were achieved for the highest vapor

to solution flow rate ratio, where the ratio of heat generated to heat removed was unity.

A numerical model is also presented that predicts temperature and concentration profiles along the length of the absorber. In the present state, the model is not adequate for realistic sizing due to assuming instantaneous absorption of ammonia vapor. An updated model is proposed that accounts for local mass transfer phenomena that accounts for bubble size reduction and eventual absorption.

Finally, sizing estimates are introduced by scaling up the absorber using the highest flow rate ratio case, 3/10. The magnitude of the scale is dependent upon the application (residential or vehicular). Absorber dimensions for a vehicle are estimated at 4 cm x 14 cm x 28 cm, and the residential absorber dimensions, 4 cm x 29 cm x 58 cm.

An Experimental Study of Ammonia-Water Bubble Absorption in a Constrained Microscale Film

by

Jeromy W. Jenks

A THESIS

submitted to

Oregon State University

in partial fulfillment of
the requirements for the
degree of

Master of Science

Presented July 20, 2007
Commencement June 2008

Master of Science thesis of Jeromy W. Jenks presented on July 20, 2007.

APPROVED:

Major Professor, representing Mechanical Engineering

Head of the Department of Mechanical Engineering

Dean of the Graduate School

I understand that my thesis will become part of the permanent collection of Oregon State University libraries. My signature below authorizes release of my thesis to any reader upon request.

Jeromy W. Jenks, Author

ACKNOWLEDGEMENTS

I would like to express gratitude to my advisor, Dr. Vinod Narayanan, for allowing me the opportunity to take part in this research. Additionally, I would like to thank Dr. Jim Liburdy and Dr. Murty Kanury for insightful discussions during the course of my collegiate study. I am fortunate to have ventured down a path of deeper understanding lead by such men.

I am also indebted to the services and machining advice provided by Manfred Dietrich and Steve Adams. Thanks to Jason Tobias and Dan Krebs for allowing me the pleasure of their company, in addition to listening to my incessant H-O-N-Cl-Br-F'n.

Thanks to my family: my father Rick and mother Kate, for immersing me in culture and change and encouraging me to challenge myself; my siblings, Justin, Brett, Jenny, Zack, and Tiff for allowing me to learn from their experiences, the privilege of being the youngest; most of all, my wife Erin Elizabeth, for never letting me forget what I'm capable of, for being a shoulder to lean on, for laughing and crying with, and for living this crazy life with me.

TABLE OF CONTENTS

Page

TABLE OF CONTENTS (Continued)

Page

LIST OF FIGURES

LIST OF FIGURES (Continued)

LIST OF FIGURES (Continued)

Figure Page

LIST OF TABLES

LIST OF APPENDICES

Page

LIST OF APPENDIX FIGURES

LIST OF APPENDIX TABLES

NOMENCLATURE

A	Heat exchange area (m^2)
A_b	Mass transfer area between the bubble and the solution (m^2)
A_c	Micro-channel cross-sectional area (m^2)
c_p	Specific heat at constant pressure (J/kg-K)
D	Mass diffusivity (m^2/s)
D_h	Micro-channel hydraulic diameter (m)
D_l	Liquid phase ammonia diffusivity (m^2/s)
d_o	Injection orifice diameter (m)
d_b	Bubble diameter (m)
g	Gravitational acceleration (m/s^2)
$\dot{g}'''$	Volumetric generation of heat (W/m^3)
h	Specific enthalpy of fluid stream (kJ/kg), convective heat transfer coefficient (W/m^2-K)
h_c	Coolant heat transfer coefficient (W/m^2 K)
h_m	Mass transfer coefficient (kg/m^2-s)
h_s	Solution heat transfer coefficient (W/m^2 K)
k	Thermal conductivity (W/m-K)
k_{ss}	Stainless steel thermal conductivity (W/m^2 K)

K_l	Overall mass transfer coefficient between liquid & gas phase (m/s)
L	Length of the microchannel (m)
$\dot{m}$	Mass flow rate (kg/s, g/min)
n_b	Number of bubbles (-)
N	Number of Control Volumes
Nu	Nusselt number (-)
P	Pressure (Pa)
$\dot{q}$	Heat rate (W)
q''	Heat flux (W/m^2)
R	Specific gas constant (kJ/kg K)
Re	Reynolds number
Re_b	Bubble Reynolds number (-)
Re_o	Orifice Reynolds number (-)
$\dot{s}$	Source rate (W)
s'''	Volumetric heat source term (W/m^3)
Sc	Liquid phase Schmidt number (-)
Sh_l	Liquid phase Sherwood number (-)
T	Temperature (K)
t	Time (s); thickness (m)
T_{ci}	Coolant inlet temperature (K)
T_{ce}	Coolant exit temperature (K)
T_{lb}	Bulk liquid temperature (K)

T_m	Mean temperature between bulk liquid and vapor (K)
T_{si}	Solution inlet temperature (K)
u	Specific internal energy (kJ/kg); fluid velocity (m/s)
u_l	Liquid velocity (m/s)
U	Overall heat transfer coefficient (W/m^2-K)
v_{slip}	Bubble slip velocity (m/s)
V_b	Bubble volume (m^3)
V_{tot}	Total vapor volume (m^3)
$\dot{V}$	Volumetric flow rate (m^3/s)
$\dot{V}_{vap}$	Vapor volumetric flow rate (m^3/s)
W	Width of the microchannel (m)
X_i	Mass fraction at interface
X_l	Mass fraction of the solution
X_{lb}	Bulk liquid mass fraction (-)

Greek

ΔT_{lm}	Log-mean temperature difference (K)
ΔX_{lm}	Log-mean concentration difference (unitless)
ρ	Density (kg/m^3)
ρ_l	Solution density (kg/m^3)
ρ_v	Vapor density (kg/m^3)

μ_b	Bubble dynamic viscosity (N s/m^2)
ν	Momentum diffusivity (m^2/s)

Subscripts

abs	absorber
c	coolant
e	exit of the microchannel
h	hot
i	inlet of the microchannel
m	mass transfer
mod	modified
s	solution
i	element number/in
ss	strong solution
v	vapor (anhydrous ammonia gas)
ws	weak solution

An Experimental Study of Ammonia-Water Bubble Absorption in a Constrained Microscale Film

1 INTRODUCTION

The advent of microscale heat and mass transfer devices has been the focus of much research over the past two decades. Due to the increased demand for more efficient heat removal from small scale, high performance electronics, the drive to conceive, develop, and produce compact and efficient heat exchangers has never been stronger. In the wake of such innovation, microscale technology has been utilized to benefit many chemical, biological, and mechanical systems, to name a few. One such system is absorption refrigeration, and the focus of this research is the miniaturization of an absorption cycle refrigeration component.

1.1 Historical Perspective of Absorption Refrigeration

Vapor absorption refrigeration cycles have existed for decades; the very first one was conceived by Ferdinand Carre in 1846. Carre and his brother Edmund developed the cycle and managed to sell the absorption refrigerator to the U.S. government during the Civil War for the purpose of making ice. Alterations to the heat-actuated cycle were made by Carl Munters, and Baltzen Platen in 1922, using ammonia, water, and hydrogen as the working fluids. Albert Einstein received a patent for another version of the cycle in 1930 and the Servel company, an acronym for "Serving Electricity," bought the rights for the two aforementioned designs. Servel received over 250 patents in absorption refrigeration in the years that followed, with total sales exceeding four million units by 1955. Servel's absorption refrigeration

cycles required combustion of fuel. During the 1970s-80s, sales dropped due to the ever increasing concern for fuel shortages and high fuel prices.[1]

A renewed interest in absorption refrigeration technology has been witnessed over the past several years due to global concern for human contribution to climate change. Using heat as the primary input and ammonia-water as the working fluid pair, absorption refrigeration technology proves to be a more environmentally friendly solution to the conventional vapor-compression refrigeration cycle. The latter cycle not only requires/consumes more electricity, but also generally uses ozone depleting chlorofluorocarbons (CFCs) as refrigerant.[2]

1.2 Refrigeration Cycles

The vapor-absorption refrigeration cycle, also known as a heat-actuated refrigeration cycle, differs from the typical vapor-compression cycle in that it utilizes a pump as opposed to a compressor to convey the working fluid to a higher pressure. The benefit of using a pump is the reduction of electrical power consumption. Figures 1 and 2 show schematics of the basic vapor compression and absorption refrigeration cycles, respectively. In both cycles, the refrigerant in liquid form is expanded to its saturation state at the evaporator pressure in process 1-2 . As the refrigerant evaporates at constant pressure in process 2-3, heat is removed from the cooling area in the amount equal roughly to the latent heat of vaporization of the refrigerant at that saturation pressure. The vapor is then compressed in process 3-4 and condensed into liquid in process 4-1. The difference between the two cycles occurs in the compression process 3-4, both achieving the same end result, but through a different process.

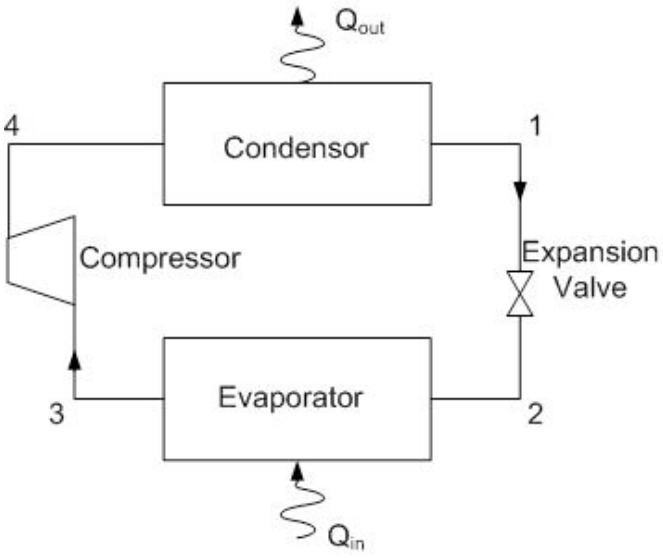

Fig. 1: Vapor-compression cycle, 1→2: expansion to saturation state, 2→3: evaporation of saturated liquid to saturated vapor (heat removed from desired cooling location), 3→4 vapor compression, 4→1: vapor condensed to liquid (heat rejected to environment)

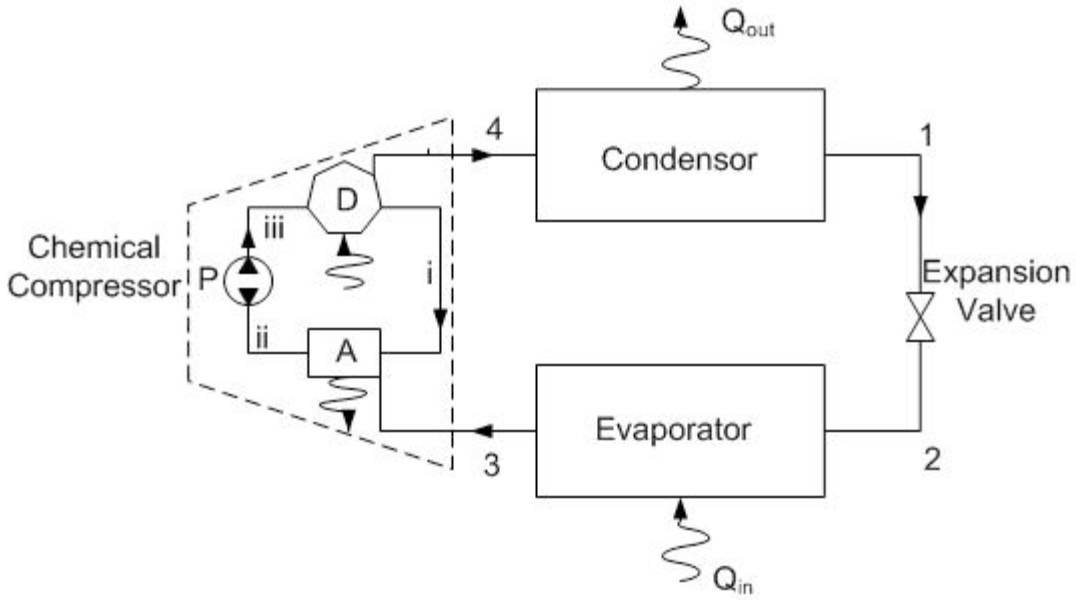

Fig. 2: Vapor-absorption cycle. 1→2: expansion to saturation state, 2→3: evaporation of saturated liquid to saturated vapor (heat removed from desired cooling location) , 3→4: vapor chemical compression, at (A) vapor is absorbed into weak solution (i), is pumped to and desorbed at (D), 4→1: vapor is condensed to liquid (heat rejected to environment)

The compressor in the vapor-compression cycle (see Fig. 1) is replaced in the absorption cycle (see Fig. 2) with a combination of an absorber (A), pump (P), and desorber (D), all of which together are termed the "chemical compressor". As shown in Fig. 2, vapor refrigerant (an absorbate) enters the absorber at point 3 along with a weak liquid solution mixture of the refrigerant, the absorbent, at point i. The process of absorption of the vapor into the weak solution mixture in an exothermic chemical reaction, that results in a more concentrated solution, which will be called a "strong solution". The strong solution at the exit of the absorber (ii) is pumped to a high pressure, in a process from ii→iii, whereupon it is introduced to the desorber. Heat is added to the desorber, also known as a generator, causing the refrigerant to vaporize. The vapor leaving the desorber, at point 4, flows into the condenser. The weak solution leaving the desorber flows to the absorber at point i, where it is throttled to the absorber pressure, and the cycle is repeated. Typically, a heat exchanger is placed between the strong and weak solution flow paths, i and ii, to reduce the heat addition at the desorber and removal at the absorber.

2 LITERATURE REVIEW

As mentioned previously, ammonia-water absorption refrigeration cycles are appealing due to the environmentally benign working fluids used, in addition to the requirement of less electrical power for the pump compared with that for the compressor in vapor compression cycles. The size of the absorber in a heat-actuated refrigeration system significantly impacts its overall size; hence several designs to reduce absorber size have been proposed.

2.1 Classification of Absorbers

The primary focus of this study is the heat and mass transfer performance of an ammonia-water absorber, a component of the chemical compressor discussed in the previous chapter. Thus far, the absorption process has been predominantly conceived using one of three techniques, namely, falling film mode, bubble mode, and spray mode. The falling film absorber, shown schematically in Fig. 3a, consists of gravity driven weak solution, s (red) flowing downwards along cooling surfaces, c_L (blue). Refrigerant vapor, v (white), flows upwards and is absorbed into the falling film. Bubble absorbers, as shown in Fig. 3b, require injection of refrigerant vapor bubbles into a weak solution liquid mixture, whereupon heat must be removed in some manner. In a spray absorber, shown schematically in Fig. 3c, weak solution is sprayed into refrigerant vapor to achieve mass transfer. Heat is typically removed in a second stage separate from the spray absorber using, for example a plate heat exchanger.

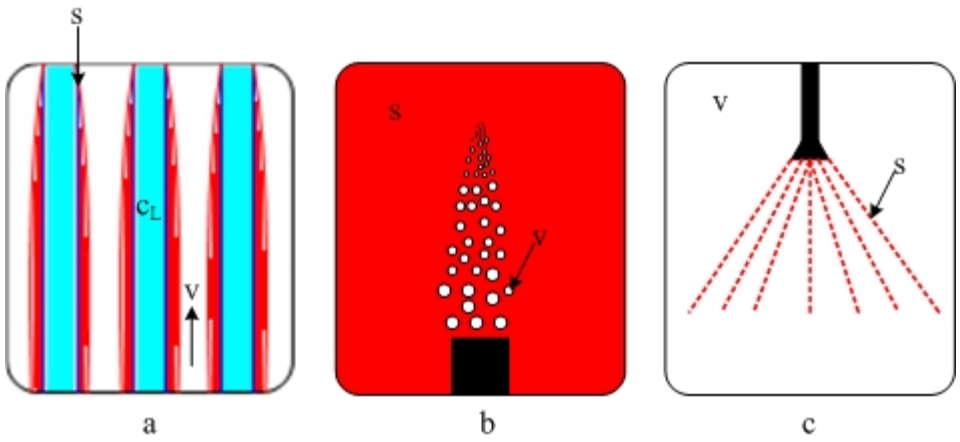

Fig. 3: Primary absorber types, (a) falling film, (b) bubble, (c) spray

2.2 Falling Film Absorption

Meachum *et al.* [3], conducted an experimental study of a falling film absorber with microchannel cooling tubes. These experiments used small diameter cooling tubes with the falling film forming along the outside. Vapor flowed upwards, countercurrent to the falling film, which wetted the array of coolant tubes. They reported a 15.1 kW heat load for an NH_3-H_2O microchannel falling film absorber with a 0.456 m^2 surface area. The major dimensions were 0.162 × 0.157 × 0.150 m. Peak solution-side heat transfer coefficients of 1,648 W/(m^2K) were reported, however, mass transfer coefficients were not reported. The absorber was an improvement to an older design, yielding improved surface wetting and flow distribution that were confirmed through high speed video capture.

Analytical studies by Goel *et al.* [4] suggest further reduction in falling-film absorber size with the addition of a mesh/fabric screen woven between the unused spacing of the tubes. Their numerical investigation concluded a size reduction of about

25 percent with the inclusion of the screen, primarily attributed to the increased mass transfer surface area. Recently, Goel *et al.* [5] found good agreement between their numerical model and an experimental study. The experiments showed that the mesh/fabric modification resulted in 17 to 26 percent higher heat loads compared to the microchannel design without a mesh screen. The 6.35 cm × 12 cm × 63.5 cm test section was also found to have a 50 percent increase in UA, the product of the overall heat transfer coefficient and the wetted tube surface area. Typically, results are presented using U alone, however, results were presented in this form because the authors could not estimate the wetting area of the solution where heat transfer occurred, and thus, U could not be obtained directly.

2.3 Bubble Absorption

Bubble absorption has been recommended by several researchers over the last decade due to its enhanced mass transfer performance over falling film while still maintaining a high heat transfer coefficient for some configurations. Typically, these configurations consist of bubble absorption occurring in a plate-type heat exchanger to achieve enhanced heat transfer.

Staicovici [6] developed a theory for absorption for multicomponent mixtures. A linear phenomenological theory of physical mono-,bi- and polycomponent gas-liquid interactions was proposed. Expressions were presented for entropy source, force and heat/mass transfer "currents." It was concluded that absorption was a mass transfer phenomena rather than a surface one, and the bubble absorber was proposed to be an efficient means of absorption.

Helbing *et al.* [7] compared falling film and bubble/slug flow ammonia-water absorbers and found the latter to have improved heat and mass transfer in the solution. Using a plate apparatus with a corrugated surface area for heat transfer, bubbles were injected at the bottom of the vertically-arranged absorber and strong solution was removed at the top portion. It was found that improving gas distribution, as dictated by the mass flow rate of the vapor and gas distributor, is a key element and improves heat transfer for this type of bubble absorber. Due to the enhanced interaction of both phases in the bubble/slug flow, improvement in heat transfer coefficients over the falling film were achieved. The authors made no mention of an ideal operating vapor mass flow rate range in terms of heat and mass transfer performance.

Kang *et al.* [8] analytically compared falling film and bubble ammonia-water absorbers and found the absorption rates to be higher in the bubble mode. They attributed this to the enhanced vapor-liquid interfacial area and greater mixing, which yielded a 48.7 percent smaller size absorber than the falling film. It was concluded that for the falling film flow, mass transfer resistance in the liquid flow was largest; however, both heat and mass transfer resistance were large in the vapor region. The bubble flow showed the highest mass transfer resistance in the liquid with heat transfer resistance being largest in the vapor. The convective heat transfer coefficients for both the solution and coolant sides was found to be the dominant contributor to the falling film absorber size, whereas the mass transfer coefficients for the liquid and vapor dominated the bubble absorber size prediction. The authors did not provide any insight as to the physics behind why these factors dominated the respective absorber size predictions.

Lee *et al.* [9] performed a comparative experimental analysis of plate-type falling film and bubble absorbers. It was found that the bubble absorber had improved mass transfer over the falling film. Heat transfer performance for the bubble mode was found to increase for an increase in either solution flow or vapor flow. Although more heat generation occurred in the bubble mode, they found that for low vapor flow and high solution flow, more heat was transferred in the falling film mode. However, for increased vapor flow rates, the bubble absorber exhibited a larger heat transfer coefficient. In a subsequent study, Lee *et al.* [10] presented experimental results on a bubble absorber with a plate-type heat exchanger. They found that increasing the weak solution flow rate seldom affected the mass transfer but improved the heat transfer. Also, they found increasing the gas flow rate produced slugging in the bubble mode, with the production of large bubbles filling the periphery of the solution channel.

J. Lee *et al.* [11] completed a numerical and experimental study of a tubular type bubble absorber without cooling. It was found that absorption regions were dependent upon the input flow rates, concentration, and temperature, in addition to the relative direction of flow between the vapor and liquid. The absorber height could be estimated through a numerical model which compared well with experimental results.

2.4 Spray Absorption

Spray absorption is another type of absorber that uses a fine spray of weak solution into the refrigerant vapor, essentially the opposite concept of a bubble absorber. To date, most research has indicated that the absorption of ammonia into water is governed by the mass transfer resistance on the liquid side. As ammonia

vapor absorbs into a weak liquid mixture of ammonia and water, the concentration and temperature near the liquid-vapor interface rises substantially, ultimately approaching the saturation condition. Higher concentration liquid must advect and/or diffuse away from the interface through the solution in order to achieve consistent mass transfer rates. However, because the higher concentrations of ammonia reside at and near the interface, mass transfer is less rapid [12]. Therefore, it would seem beneficial to reduce the liquid volume to the size of a fine spray, effectively reducing the resistance on the liquid side; herein lies a potential benefit for spray absorption.

Huang, *et. al.* [13] proposed a theoretical model for the absorption of ammonia vapor into a fine spray of water. The model enabled characterization of parameters that influenced absorption efficiency. Model simulation resulted in an increase in absorption for reducing the droplet diameter, decreasing the weak solution concentration, and increasing the ammonia vapor concentration.

The use of a spray absorber in a refrigeration cycles is actually a two-part system, in that it separates the heat and mass transfer into different components as detailed by Summerer, *et. al.* [14]. Initially, the weak solution is cooled well below the saturation state, possibly in a plate heat exchanger. The solution than enters an adiabatic spray absorber where the mass transfer occurs. Venegas, *et al.* [15] proposed the absorption of ammonia vapor by lithium nitrate-ammonia solutions. Using a plate heat exchanger, heat transfer coefficients of 5.8 kW/m^2-K were realized, from which it was considered an order of magnitude higher than falling film absorbers. Literature was not found that compared spray absorbers with bubble absorbers.

3 MOTIVATION AND OBJECTIVES

3.1 Motivation

Given the renewed interest in absorption refrigeration, it is desirable to achieve a cycle that is sufficiently small and cost-efficient in order to be implemented on a residential, or even smaller scale for portable applications. The performance of the absorber is one of the key elements in making a viable absorption-refrigeration cycle, and has been dubbed the "bottleneck" for the entire system [3]. Thus far, absorption refrigeration has been relegated to industrial applications where waste heat is used for the desorber input and unit size is of not much concern. In order to compete in the residential and other markets, absorption technology must scale-down, while still maintaining adequate cycle performance [2].

3.1.1 Proposed Concept

In order to combine the enhanced heat and mass transfer attributes of the falling film and bubble absorbers, respectively, it may be beneficial to reduce the flow-paths of a plate-type bubble absorber to the microscale. Also, instead of a co-flowing vapor stream that absorbs into the weak solution, it may be beneficial to have microbubbles of vapor impinge on a weak solution thereby increasing mixing and liquid-vapor interface area. Consider one such absorber, shown in Fig. 4., that incorporates the above characteristics. Refrigerant vapor (ammonia) is introduced through a microporous wall thereby injecting small bubbles in a large aspect ratio microchannel. The combination of small bubbles and the microchannel ensure a large absorption surface area per unit volume of solution flow. Cooling water flows

countercurrent to the solution, achieving high heat transfer rates due to the large cross-stream temperature gradients that exist in microscale flows. It is conjectured that with this type of arrangement, absorber performance will be enhanced and thus, the overall size dramatically reduced. An additional benefit to this type of bubble absorber is that it may be orientation independent, and can still function regardless of its position with respect to gravity. Given this attribute, the bubble absorber would be beneficial to portable refrigeration cycles. One additional benefit could be the use of such an absorber in a micro- or zero-gravity environment.

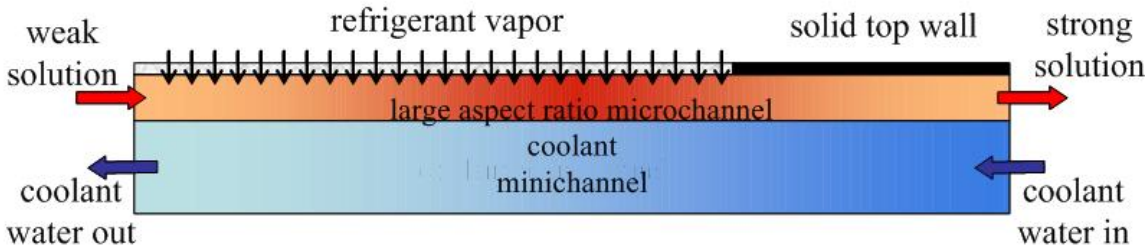

Fig. 4: Schematic of a microscale constrained film bubble absorber

Research summarized thus far corroborates the claim that bubble absorption shows promise compared with the falling film mode. However, it should be noted that bubbles were injected on only one end of the absorber, the entrance, and flowed along the absorption channel where mass/heat transfer occurred. A drawback to such a design is the limit to the amount of small bubbles that can be introduced in the absorber, as the introduction can only occur at one point. The current absorber is original in that, aside from being microscale technology, ammonia refrigerant impinges upon the flowing solution throughout much of the absorption channel, thereby enhancing the number of small bubbles dispersed throughout the solution.

3.2 Objectives

The purpose of this study is primarily to characterize the performance of a constrained microscale film bubble absorber by experimental studies. A preliminary model that predicts absorber performance and size is also developed.

Experiments detailed herein are such that the effect of variations in channel geometry, system pressure, inlet weak solution concentration, and vapor/solution mass flow rates on the heat and mass transfer characteristics of the constrained thin film absorber are determined. Experiments are performed at an operating pressure range of 1, 2.5 and 4 bar absolute, and fixed weak solution mass concentrations of 0, 5, 10 and 15 percent. Weak solution flow rates of 10, 20 and 30 g/min as well as vapor flow rates of 1, 2 and 3 g/min were also studied. Both the weak solution and ammonia vapor flow rates are varied and these fluid streams enter the absorber nominally at 25^{o}C.

In addition to an experimental study, it is desirable to develop a predictive model that encompasses both heat and mass transfer effects. A validated model can provide information on local temperature and concentration profiles along the length of the absorber. Also, a validated model can be beneficial in parametric studies. Ultimately, results obtained from the model will aid in the design, performance and sizing estimates of constrained-thin-film bubble absorbers. In the present study, the scope is limited to development of a model for complete and instantaneous absorption within the microchannel. Such a process is not physically accurate, and thus, a proposal is given to improve the model for future use.

4 EXPERIMENTAL FACILITY AND PROCEDURE

The following chapter describes in detail the absorber test section under scrutiny, the experimental facility and the critical components. In addition, a summary of the experimental procedure and test conditions is given.

4.1 Test Section

Figure 5 shows a solid model of the test section. Anhydrous ammonia entered the gas plenum, fabricated using PEEK^{TM}, through both sides of the test piece. Weak solution entered the absorber at the inlet plenum and flowed along the microchannel to the exit plenum. The gas flowed through a stainless steel sintered porous plate of 0.5 μm pore size and impinged upon the liquid solution that flowed in a 10 cm long x 2 cm wide stainless steel microchannel. The latter third of the gas plenum was blocked such that ammonia gas could not bubble through the sintered plate into the microchannel in this section. This was a modification made from the work presented in Jenks and Narayanan [10] to ensure complete absorption within the test section. The major dimensions of the absorber were 0.145 m x 0.09 m x 0.06 m. Note that this size would be significantly reduced in the absence of measurement devices. The coolant minichannel was located on the backside of the microchannel and coolant flowed counter to the solution flow direction as indicated in Fig. 5. The heat released during absorption on the solution side was removed by the coolant (water). A recirculation chiller (ThermoHaake C30P) supplied the coolant water at the prescribed inlet temperature. Mass flow rate of the water was measured by a correlated rotameter

(Gilmont GF1360)**.** The coolant side channel had the same dimensions for all absorber configurations/geometries studied (10 cm x 2 cm x 0.88 mm).

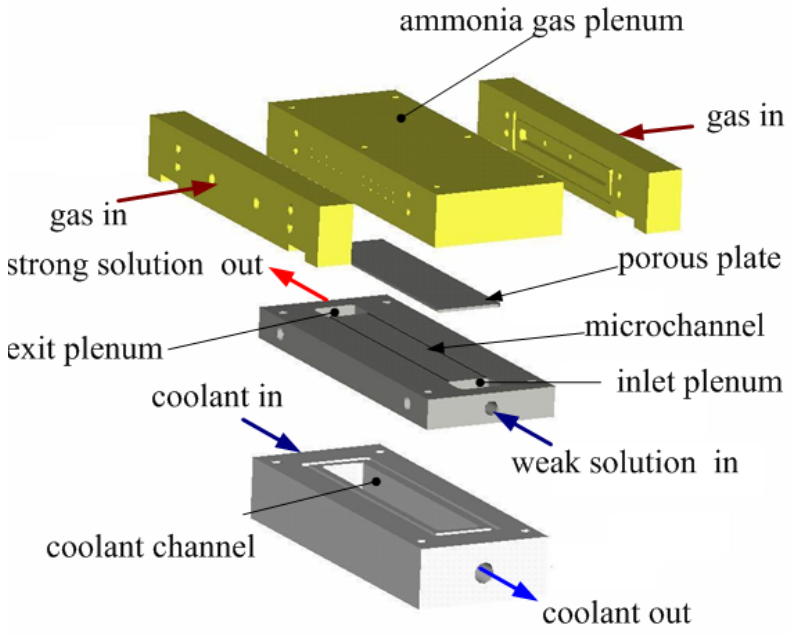

Fig. 5: Schematic of the absorber test section

Table 1 summarizes the six basic geometries of the absorber microchannels used in this study. The first channel geometry is a 150 µm deep channel with a smooth bottom wall that was used in preliminary work [16], and its performance is compared with the five other channel geometries. The second and third channels are 400 µm and 1500 µm deep with a smooth bottom wall. Comparatively, the film thickness reported for falling film ranged from 200-530 µm for a computational fluid dynamics study performed by Garimella, *et. al.* [2]. The other three channels have a nominal depth of 150 µm and have on their bottom walls either cross-ribs (CR), 45 degree angled cross ribs (ACR) or streamwise fins (SF); these geometries are indicated in the photographs in Figs. 6a, b & c, respectively. The intent of the CR and ACR structured surface designs was primarily to cause bubbles to reside in the valleys between the ribs and

thereby increase the residence time for absorption. The SF channel was designed with the intent of heat transfer surface area enhancement.

Table 1. Microchannel Geometry

Channel	**Nominal Channel Depth (μm)**	**Additional Microchannel Geometry**
1-Smooth	150	none
2-Smooth	400	none
3-Smooth	1500	none
4-Cross Ribbed (CR)	150	250-μm steps (22) machined into base surface of microchannel
5-Angled Cross Ribbed (ACR)	150	250-μm 45^{o} steps (n=13) machined into base surface of microchannel
6-Streamwise Finned (SF)	150	~150-μm tall fins (n=9) protruding from the base of the microchannel

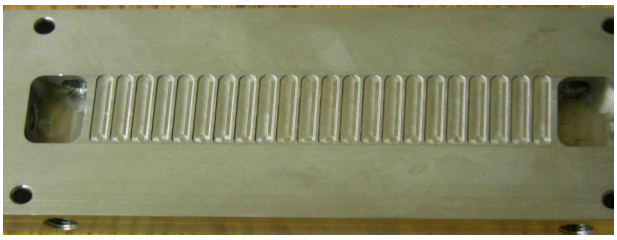

(a)

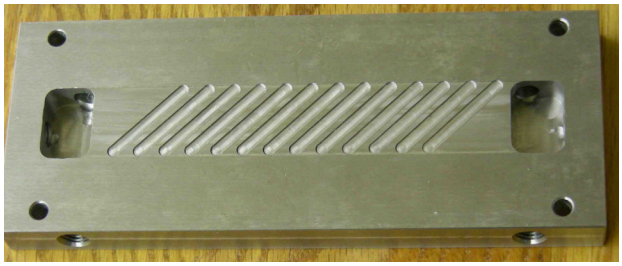

(b)

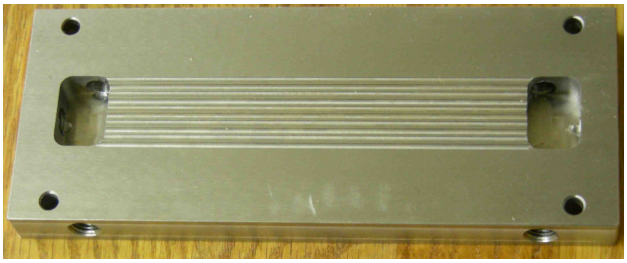

(c)

Fig. 6. Photographs of the three structured microchannels. (a) cross-ribbed (CR) channel, (b) 45^{o} angled cross-ribbed (ACR) channel, and (c) streamwise-finned (SF) channel

The structures acted like fins on the bottom wall. A preliminary estimation of fin effectiveness of a 250-μm-long stainless-steel fin, based on a heat transfer coefficient of 1814 W/m^2-K, indicated that the fin efficiency was 99.9 percent. Hence, the entire fin area can be treated to be at the same temperature as the bottom wall.

4.2 Flow Loop and Instrumentation

The experimental facility was an open loop system that supplied the necessary operating conditions to the absorber. Figure 7 presents a schematic of the experimental facility used in this study and Table 2 lists the major components used. The facility was constructed using materials compatible with ammonia, and necessary safety precautions were taken during the course of experimentation. Anhydrous ammonia was regulated and supplied from a gas tank to the gas plenum of the absorber through a mass flow controller (Sierra Instruments, model C100L), which also measured the gas flow rate. The system pressure was maintained by pressurizing the inlet and exit solution reservoirs using compressed air. The flow rate of inlet weak solution was controlled using a variable speed gear pump. A Coriolis flow meter (Micromotion, CF010 sensor and 2700 transmitter) was used to measure the mass flow rate and density of the incoming weak solution. A translucent Teflon® PFA visualization section was located at the exit of the absorber to monitor the level of absorption within the test section. A three-way solenoid valve, located at the exit of this visualization section was used to divert the strong solution into alternate paths. During the data collection at steady state, the valve directed the flow to a sample reservoir, which was a closed container to prevent evaporative loss. At all other times, the strong solution was directed to a discharge reservoir.

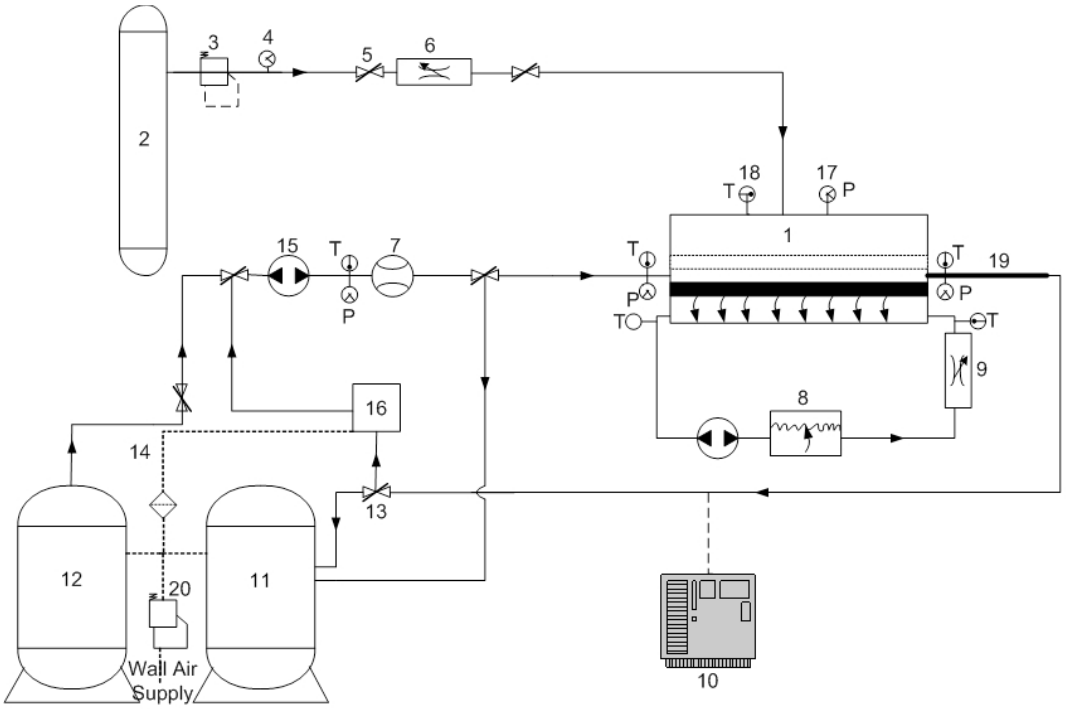

1. Absorber	6. Gas Flow Controller	11. Discharge Reservoir	16. Sample Reservoir
2. NH_3 Tank	7. Corriolis Flow Meter	12. Weak Solution Reservoir	17. Pressure Transducer
3. Pressure Regulator	8. H_2O Chiller/Recirculator	13. 3-way Solonoid Valve	18. Thermocouple
4. Pressure Guage	9. Rotameter	14. Filter	19. Visualization Section
5. Manual Valve	10. Data Acquisition	15. Gear Pump	20. Air Pressure Regulator

Fig. 7: Schematic of test facility

Table 2. Instrumentation Specifications

Instrumentation (Qty)	Make/Model/Specifications/Range
Mass Flow Controller (1)	Sierra Instruments, model C100L Range/Output: 0-10 SLPM/0-5 VDC
Variable Speed Gear Pump (1)	Micromotion Series 180 Max pressure differential: 5.2 Bar
Coriolis Flow Meter (1)	Micromotion Sensor/Transmitter: CF010/2700 Mass Flow Range: 0-1370 g/min
Three-way Solenoid Valve (1)	Burkert Supply/Max Pressure: 24 VDC/1000 kPa
Thermocouples (9)	Omega Type: T Range: (23-623 K)
Pressure Transducers (4)	Omegadyne Model PX302: (Range 0-690 kPa) Model PX32B1: (Range 0-690 kPa)
Recirculation Chiller (1)	ThermoHaake C30P Supply: 220V/10A T-range: 243-473 K Max P/Flow: 560 mBar/24 l/min
Rotameter (1)	Gilmont GF1360 Tube size: 3 (shielded) Range: 0.6-780 mL/min
Pressure Regulator (2)	(1)-Fairchild (Air) Range: 0.15-10 Bar (2)-Swagelok (Ammonia) Low pressure (LP) Side: 0-690 kPa High pressure (HP) Side: 0-24.8 MPa

Temperature and pressure were monitored at the absorber inlet and exit for the solution, the gas inlet, and at the Coriolis flowmeter, as indicated in Fig. 7. The temperatures were measured using calibrated T-type thermocouples, while the pressures were measured using calibrated capacitance-type absolute pressure transducers (Omegadyne, models PX302 and PX32B1). Data from all instruments were recorded real-time through data acquisition boards (National Instruments) using a LabVIEW® program.

4.3 TEST PLAN AND PROCEDURE

In order to determine the effects of pressure, inlet concentration, vapor/solution mass flow rates, and geometry on the performance of the absorber, a systematic test plan was developed. Table 3 details the variables used for two primary data sets; a data set consisted of dozens of individual experiments. All experiments were completed using the same nominal coolant flow rate, 268.5 g/min ±3.5 g/min.

Table 3. Summary of variables used for data collection

Data Set	Nominal absorber Pressure (absolute, Bar)	Weak solution Concentration (%)	Vapor/Solution Flow Rate (g/min)	Geometry
1	1, 2.5, 4	0, 5, 10, 15	$\dot{m}_v$: 1, 2, 3 $\dot{m}_{ws}$:10, 20, 30	Fixed: 150μm
2	4	15	$\dot{m}_v$: 1, 2, 3 $\dot{m}_{ws}$:10, 20, 30	150μm 400μm 1500μm Cross Ribbed (CR) Angled Cross Ribbed (ACR) Streamwise Finned (SF)

Table 4 details a typical test matrix for a fixed system pressure, inlet concentration, and geometry. A total of 110 experimental runs were used in this study.

Table 4. Test matrix for a given geometry, system pressure, and inlet concentration

Run	Pressure (Bar)	X_{ws} (%)	$\dot{m}_v$	$\dot{m}_{ws}$
1	4	15	1	10
2	4	15	2	10
3	4	15	3	10
4	4	15	1	20
5	4	15	2	20
6	4	15	3	20
7	4	15	1	30
8	4	15	2	30
9	4	15	3	30

In the interest of consistent data collection, a standard operating procedure was developed. During the startup procedure, the test facility was first pressurized with compressed air supplied to the inlet, exit, and sample reservoirs. Upon reaching the desired system pressure, cooling water at a fixed temperature of 10^{o}C and flow rate of 268.5 g/min was then supplied to the test section. The cooling water flow rate was monitored at the rotameter periodically during data collection to ensure it remained constant. A weak solution at a fixed flow rate and concentration mass fraction was then introduced into the absorber. In between experiments, the inlet density was monitored at the corriolis flow meter. When the inlet reached a steady value, the flow rate was adjusted as dictated by the test matrix. This was done by setting the power of the gear pump to a prescribed setting for the given flowrate, and then adjusting a needle valve to fine tune the flow rate. The solution flow rate could be monitored on the Corriolis flow meter display. With the weak solution flow rate set, power was then shut off to the pump and vapor introduced to the absorber. This involved the input of the vapor flow rate through a software program on the computer that governed the gas flow controller. This was an effort to remove excess solution that may have leaked into the gas plenum in between experiments, and was essentially purging the absorber with ammonia. When the system was purged, as indicated by only ammonia vapor flowing in the visualization section, the gear pump was switched on and solution flowed at the desired previously set rate. The inlet and exit temperatures of the coolant and solution were then monitored. At steady state, the 3-way solenoid valve was opened to permit strong solution to flow into the clear sample reservoir, at which point data collection via LabView® was initiated. Steady state was considered attained

when the inlet and exit solution and coolant temperatures, as well as weak solution and vapor mass flow rates, were constant. Strong solution was collected in the sample reservoir for the duration of the steady state run. The sample reservoir was pressurized and kept equalized at the nominal system pressure. Upon completion of each experiment, the vapor flow was shut off and the pump was switched from the weak solution inlet tank, to the sample reservoir. This was achieved via a 3-way valve that introduced the strong sample solution into the Coriolis flowmeter. Upon attainment of a steady value for the pressure, temperature, and density of the strong solution, these data were recorded to determine the exit concentration.

5 DATA REDUCTION AND ANALYSIS

5.1 Mass Balance

An overall mass balance for the absorber was used to determine the mass flow rate of the exiting strong solution

$$\dot{m}_{ss} = \dot{m}_{ws} + d\dot{m}_{v} \tag{1}$$

Inlet and exit concentrations were determined from the measurements of strong solution density, pressure, and temperature using the NH3H2O call function in Engineering Equation Solver®, which utilizes correlations from Ibrahim *et al.* [17].

$$x = f(T, P, v) \tag{2}$$

A species mass balance yields a check for the measured exit concentration

$$x_{ss} = \frac{\dot{m}_{ws} x_{ws} + \dot{m}_{v}}{\dot{m}_{ss}} \tag{3}$$

5.2 Heat Transfer

The required enthalpies can be found from the aforementioned correlations from Ibrahim, *et al.*

$$h_{s} = f(T_{s}, P_{s}, x_{s}) \tag{4}$$

$$h_{v} = f(T_{v}, P_{v}) \tag{5}$$

The heat transferred to the coolant, or heat duty, can be found from an energy balance on the solution side

$$\dot{q}_{abs} = \dot{m}_{ws} h_{ws} + \dot{m}_{v} h_{v} - \dot{m}_{ss} h_{ss} \tag{6}$$

where $\dot{q}_{abs}$ was also compared with the absorber heat load as calculated from the coolant side,

$$\dot{q}_c = \dot{m}_c c_p (T_{co} - T_{ci}) \tag{7}$$

to quantify any losses.

The overall heat transfer coefficient, U, with the absorber as the hot side and coolant flow as the cold side of the heat exchanger is given by

$$\mathrm{U} = \frac{\dot{q}_c}{A \Delta T_{lm}} \tag{8}$$

where the log-mean temperature difference, LMTD, is determined as

$$\Delta T_{lm} = \frac{(T_{ws} - T_{ce}) - (T_{ss} - T_{ci})}{\ln\left(\frac{(T_{ws} - T_{ce})}{(T_{ss} - T_{ci})}\right)} \tag{9}$$

Note that the heat exchanger analysis performed in this study is mostly based on the traditional heat exchanger analysis definition of U. However, as detailed by Narayanan, *et al.* [18], unlike typical heat exchangers, there is a source term, that of heat of absorption, which increases the temperature of the hot stream that flows through the absorber. An energy balance on a control volume enclosing the solution (hot) side with the inclusion of a source term, yields

$$\mathrm{d\dot{s}} = \dot{m}_s c_s \mathrm{d}T_s + \mathrm{d\dot{q}} \tag{10}$$

The term $\mathrm{d\dot{s}}$ refers to the source rate term per control volume, which accounts for the additional heat generation due to the heat of absorption within the hot side of

the heat exchanger. The term $d\dot{q}$ represents heat transferred to the counter flowing coolant.

Expressing the same energy balance in terms of enthalpies

$$\dot{m}_{ws} h_{ws} + d\dot{m}_v h_v = \dot{m}_{ss} h_{ss} + d\dot{q} \tag{11}$$

Representing $\dot{m}_{ss}$ in terms of the two inlet fluid streams (vapor and inlet weak solution) by a mass balance, Eq 11 becomes

$$\dot{m}_{ws} h_{ws} + d\dot{m}_v h_v = (\dot{m}_{ws} + d\dot{m}_v) h_{ss} + d\dot{q} \tag{12}$$

Expressing h_{ss} in terms of h_{ws} using a Taylor series expansion, and truncating the resultant expression to the first order terms results in

$$d\dot{m}_v (h_v - h_{ws}) = \dot{m}_{ws} dh_{ws} + d\dot{q} \tag{13}$$

A comparison of Eq. 13 with Eq. 10 reveals that the left side of Eq. 13 is identically equal to the source term within the control volume, and thus

$$\dot{s} = \dot{m}_v (h_v - h_{ws}) \tag{14}$$

where $\dot{s}$ refers to the generation over the entire absorber.

5.3 Mass Transfer

The overall mass transfer coefficient was determined using the vapor flow rate and the heat exchange surface area,

$$h_m = \frac{\dot{m}_v}{\Delta X_{lm} A} \tag{15}$$

where ΔX_{lm} denotes the log-mean concentration difference between the liquid at the liquid-bubble interface and the bulk solution from the inlet to the exit,

$$\Delta X_{lm} = \frac{(X_{ws,sat} - X_{ws}) - (X_{ss,sat} - X_{ss})}{\ln\left(\frac{X_{ws,sat} - X_{ws}}{X_{ss,sat} - X_{ss}}\right)} \tag{16}$$

5.4 Uncertainty Analysis

Uncertainty analysis was performed on all measured variables and propagated through the calculations to the reported variables for all experimental conditions. Values of uncertainty are represented as error bars in most of the figures presented in the Results and Discussion section. Figures where error bars do not exits are re-representations of data where error bars are included elsewhere. For each trend line or test condition an averaged error bar is presented in the figures for visual clarity of data trends.

Thermocouples and pressure transducers were calibrated using a NIST-traceable reference standard. The Coriolis mass flowmeter was calibrated using a computer-controlled catch-and-weigh method. Manufacturer's calibration was used to determine the bias error in the gas flow controller and Coriolis flowmeter density. Uncertainty in mass concentration and ΔT_{lm} were determined using a sequential perturbation technique [13] in EES® based on the measurement uncertainties in temperatures, pressures, and densities. The propagation of errors method [19] was used to determine uncertainties in other calculated quantities. Uncertainty in $\dot{q}_{abs}$ was determined using Eq. 6 and includes uncertainties in mass flow rates and enthalpies.

The preceding errors where then finally propagated into Eq. 8 and Eq. 15 to find the uncertainty in U and h_m, respectively.

Figure 8 shows the difference between the heat load using Eq. 6 and Eq. 7 for the 150-μm smooth channel absorber for experiments used in the next chapter. Considering all 110 experiments, inclusive of the other smooth channels and structured absorbers, this difference was 7.51 percent. The heat load, $\dot{q}_{abs}$, found from Eq. 6 was used in the heat transfer results presented in the next chapter. Differences in the two heat loads could be attributed to heat gain of the coolant side from the ambient. Possible reasons for the difference between the two estimates are heat gains through the exterior surfaces of the cooling channel from the surroundings. Though the coolant side was enclosed by a high density polyethylene plastic (HDPE) for insulation purposes, extra insulation may have been necessary. The heat load for the coolant was on the average, 2 watts greater than that calculated on the solution side. Considering a thermal conductivity of 0.3 W/m-K for HDPE, the heat gain via pure conduction from the ambient using a ΔT of 12 K was estimated to be 1.5 watts. Thus, it is probable that the gains are predominately due to conduction through the HDPE. Because the difference between these two estimates was within reasonable limits, further efforts to quantify the discrepancy was not undertaken.

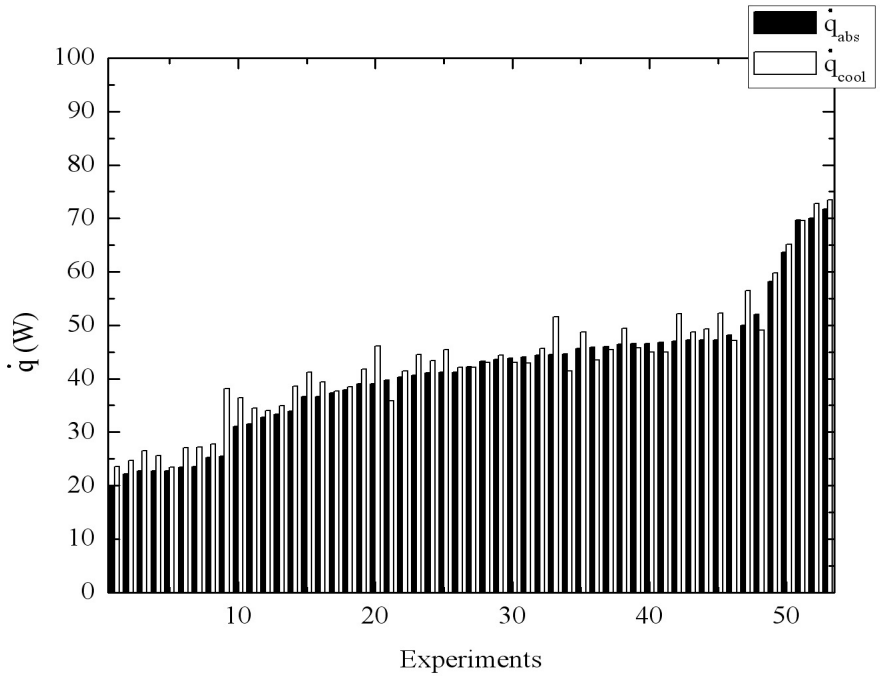

Fig. 8. Comparison of heat transferred from the absorber with heat transferred to the coolant for the 150 µm smooth channel

Shown in Fig. 9 is the difference in strong solution concentration, X_{ss}, using either Eq. 2 (X_{ss} Sample) or Eq. 3 (X_{ss} Predicted) for all data analyzed for the 150-µm absorber. As noted earlier, the sample concentration was found using the coriolis flow meter density measurements, along with temperature and pressure measurements. The predicted X_{ss} was compared with the sample value found to ensure that both the mass flow rates and Coriolis flow measurements were in agreement in yielding approximately the same X_{ss}. The average difference between these values was 6.74 percent for all microchannel structure data used. Results presented in the following chapter were found using the sample concentration.

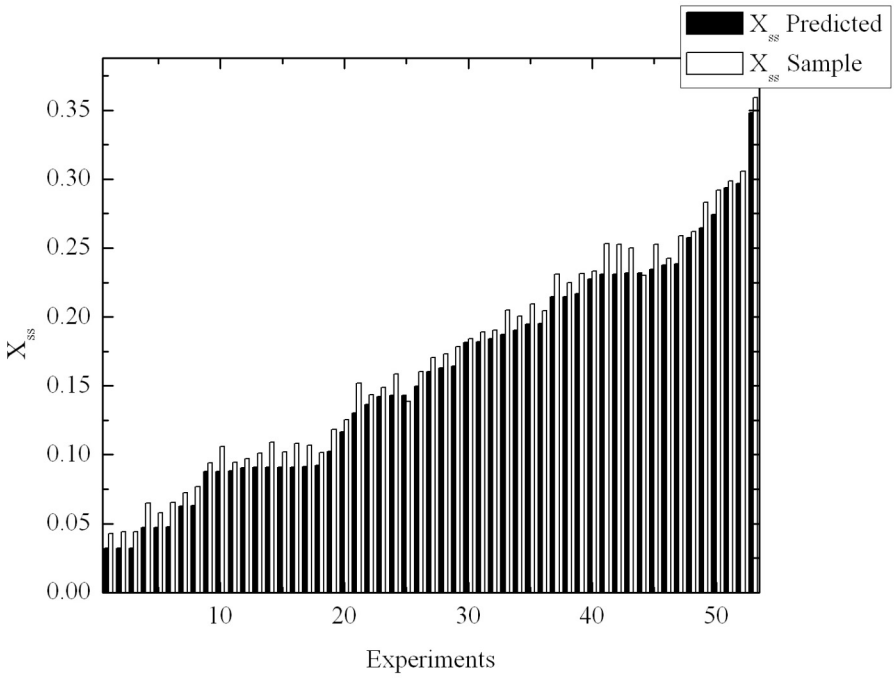

Fig. 9. Comparison of exit concentration found from the sample measurements and predicted using Eq. 3 for all experiments used in analyzing the 150-µm smooth channel geometry

6 RESULTS AND DISCUSSION

This chapter presents heat as well as mass transfer results obtained for various test conditions indicated in Table 3 in Chapter 4. Flow variables include the weak solution flow rate, varied from 10 g/min to 30 g/min, and the vapor flow rate, which was varied from 1 g/min to 3 g/min. The corresponding Reynolds number ranges for the weak solution and vapor flows for the smooth geometries are indicated in Table 5, where both solution and vapor Re are based on the microchannel cross section. The coolant side flow rate was held fixed at 268.5 g/min, corresponding to a Re = 370 , and the inlet temperature held constant at 10.6 ^{o}C. The weak solution inlet mass concentration was either varied from zero to 15 percent (for the 150-μm absorber) or held fixed at 15 percent (for the other absorber geometries). The inlet temperature of the weak solution was measured at the coriolis flowmeter and was held nominally constant at 22.5 ^{o}C. The inlet temperature of ammonia vapor was measured in the gas plenum and held nominally fixed at 22.4 ^{o}C.

Table 5. Microchannel Reynolds number for smooth channels

Nominal channel depth (μm)	Vapor Reynolds number Re_v (1,2 and 3 g/min)	Weak solution Reynolds number Re_{ws} (10, 20 and 30 g/min)
150	173, 346, 520	15, 30, 45
400	171, 342, 514	15, 30, 45
1500	162, 324, 486	14, 28,4 3

Representative average uncertainty estimates are indicated for each series of plots in the graphs in order to preserve clarity of presentation. Some graphs do not

have error bars for data; these graphs are cross-plots from other graphs in which error estimates are already indicated. Data for the 150-μm microchannel absorber are presented for a working pressure of 2.5 bar and 4 bar absolute. All other geometries were tested at a pressure of 4 bars absolute. Reference to pressure henceforth will be made with an absolute reference and will not be explicitly mentioned. Results are typically presented for a ratio of vapor to weak solution flow, $\frac{\dot{m}_v}{\dot{m}_{ws}}$, henceforth referred to as flow rate ratio. Data presented in the following section are for conditions of complete absorption within the test section, as verified by visual observations of the exiting strong solution flow in the clear exit section.

Only data for 10 g/min and 30 g/min weak solution flow rates are presented and discussed in this chapter; the 20 g/min flow rate trends are similar to those of the 30 g/min case and are hence documented in appendix 4.

6.1 Preliminary Proof of Concept Experiments

Jenks and Narayanan [16] performed feasibility experiments on a constrained liquid film microchannel bubble absorber. Experiments were performed for the smooth 150 μm at a pressure of 1 bar and a fixed inlet temperature of the weak solution, for weak solution flow rates from 10 to 30 g/min, inlet mass concentrations from 0 to 15 percent, and gas flow rates between 1 and 3 g/min. Results indicated that the overall heat transfer coefficient changed little for lower inlet weak solution concentrations and for lower gas flow rates; in general, these values ranged from 600 to 1100 W/m^2-K.

Visualization at the exit of the absorber revealed the presence of periodic ammonia bubbles, occurring in varying sizes and periods, indicating that improvements to the current design were necessary to ensure complete absorption within the microchannel. These improvements were manifested in the form of blocking the last third of the gas flowing into the microchannel, as was shown in Fig. 4, in order to ensure complete absorption within the microchannel. It was believed that bubbles injected in the latter portion resulted in inadequate residence time for this section of the absorber. Due to the higher liquid concentrations and thus, higher resistance to mass transfer in this section, bubbles injected there may escape the absorber exit before complete absorption could occur. Thus, the latter third portion of the channel was blocked to vapor flow.

6.2 Effect of Porous Plate Hole Pattern

Qualitative studies were performed to document the effect of patterned holes on the top plate on bubble formation within the microchannel. It was conjectured that spacing the holes appropriately may improve absorption and inhibit bubbles exiting the absorber. Figure 10 shows the bubble formation within the microchannel for different plates. Three types of plates were considered: (a) a 0.5 μm-pore size sintered stainless steel plate (Fig. 10 a) used for the proof-of-concept studies of Section 6.1, (b) a triangular hole pattern (Fig. 10 b and c), and (c) a staggered hole pattern (Fig. 10 d and e). The patterned plates were made using PEEK® with 150 μm diameter holes drilled into plate surface. The staggered hole plate had 57 holes and the fractal plate has a total of 36 holes. The spacing between holes within a column was 1.4 mm and

the inter-column spacing was 10.7 mm. Note that the exit velocity of vapor through the holes in the three plates could not be matched due to the unknown number of holes in the sintered porous plate. However, for the visualization experiments, the total vapor mass flow rate was held constant at 0.5 g/min. In addition, the size of the holes was significantly larger for the patterned plates due to manufacturing constraints. For the visualization experiments, the heat exchanger was replaced by a clear acrylic block, which formed one wall of the microchannel. Because there was no cooling water channel used in this visualization study, a large weak solution flow rate of 36 g/min along with a low vapor flow rate was used.

Qualitative visualization, shown for the three plates in Figs. 10a, 10c, and 10e indicated that a larger number of smaller size bubbles entered into the microchannel with the use of the sintered plate. The patterned plates produced larger bubbles, leading to a smaller net interfacial area for absorption. The hydrophobic nature of PEEK® might be a contributing factor to the differences in the bubble activity shown in Figs 10c and 10e compared to that in Fig. 10a. Another factor could have been the velocity of bubble injection, which could not be kept constant between the three plates. Note that this is likely to be the major factor influencing the bubble sizes observed for the patterned plates, see Figs. 10c and 10e, with larger bubbles resulting in the plate with fewer holes. Based on the results of the visualization study, further experiments to obtain quantitative data were performed using the sintered porous plate.

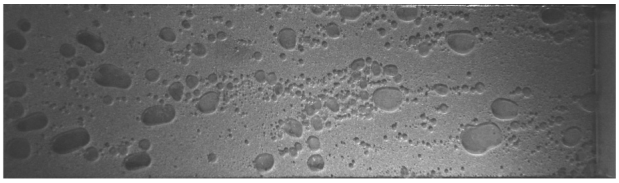

(a)

(b)

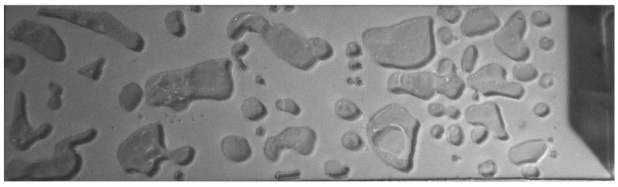

(c)

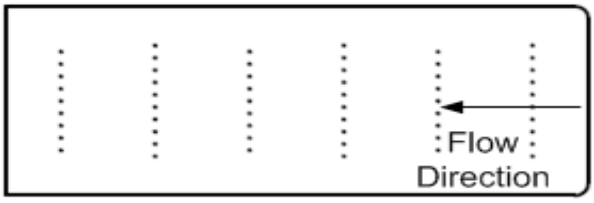

(d)

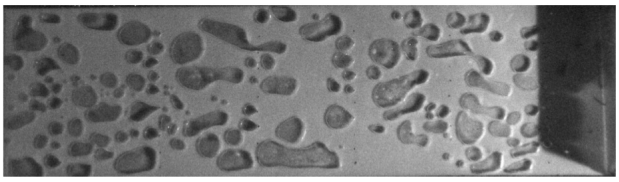

(e)

Fig. 10. Effect of plate hole pattern and material on bubble size and distribution (a)sintered stainless steel plate with 0.5μm holes, (b,c) triangular hole pattern, (d,e) staggered hole pattern. The solution flow rate was 36 g/min, and the ammonia gas flow rate was 0.5 g/min

6.3 Mass Concentration Effects

6.3.1 Exit Concentration

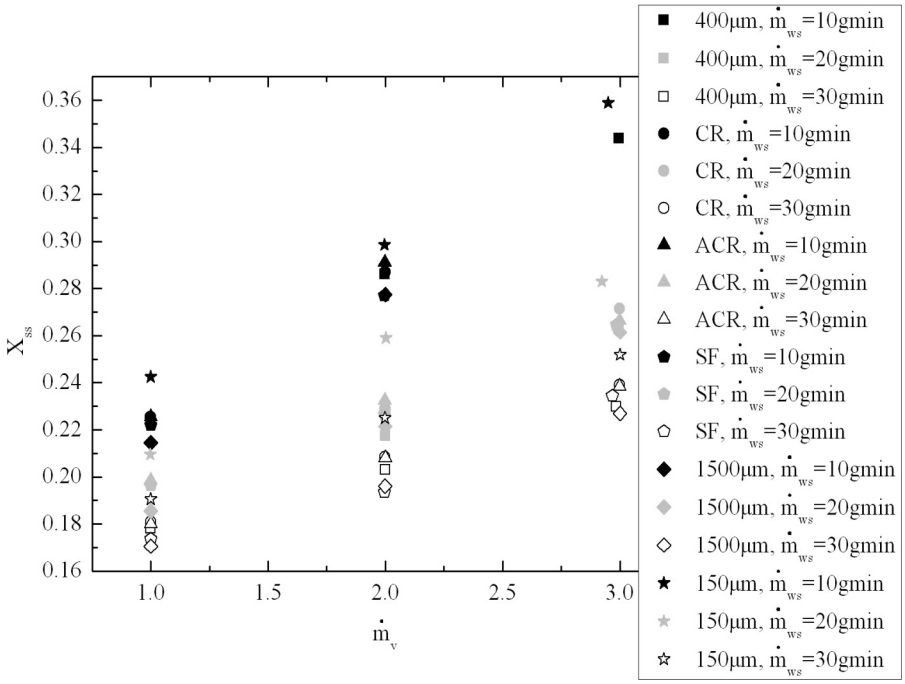

Fig. 11. Variation of strong solution concentration with vapor flow rate (g/min) for various geometries

Figure 11 shows the effect of ammonia vapor mass flow rate on the exit concentration for all weak solution mass flow rates and geometries considered. Ideally, for a given weak solution and vapor mass flow rate, the exit concentration should remain fixed for all channel geometries considering data was only taken for complete absorption. However, due to deviations from the desired fixed inlet concentration of 15 percent for the channel geometry study, the exit concentration varies accordingly. The most extreme variance is found for the weak solution mass

flow rates of 20 g/min and the 150μm channel, for which a difference of 3 percent exists. The exit concentrations presented in this figure were found using the measured temperature, pressure, and density of the strong solution. The obvious trend shows that for an increase in vapor flow rate, there is an increase in exit concentration, where the same result can be achieved by reducing the weak solution flow rate for a constant vapor flow. Close inspection reveals that all structured geometries (CR, ACR, SF) and the 1500 μm channel could not achieve complete absorption for the highest mass flux of vapor $\dot{m}_v$=3 g/min and lowest solution flow rate $\dot{m}_{ws}$=10 g/min, and thus, no data was taken for these structures. This alone may be an indicator that the 150μm and 400 μm channels are superior to the other channel geometries. As indicated by Fig. 11, concentration gains of 20 percent were possible for the 150 μm and 400 μm channels for the largest vapor and lowest weak solution flow rates.

6.3.2 Inlet Concentration Effects

Figure 12a shows the overall heat transfer coefficient, U, for various flow rate ratios in the 150 μm absorber for a system pressure of 2.5 bar. Note that the coolant channel dimensions were kept identical for all experiments in order to determine the effect of structured surfaces on the absorber microchannel heat transfer coefficient. The overall heat transfer coefficient for the heat exchanger was based on the heat exchange area on the coolant side, which remained at 10 cm x 2 cm.

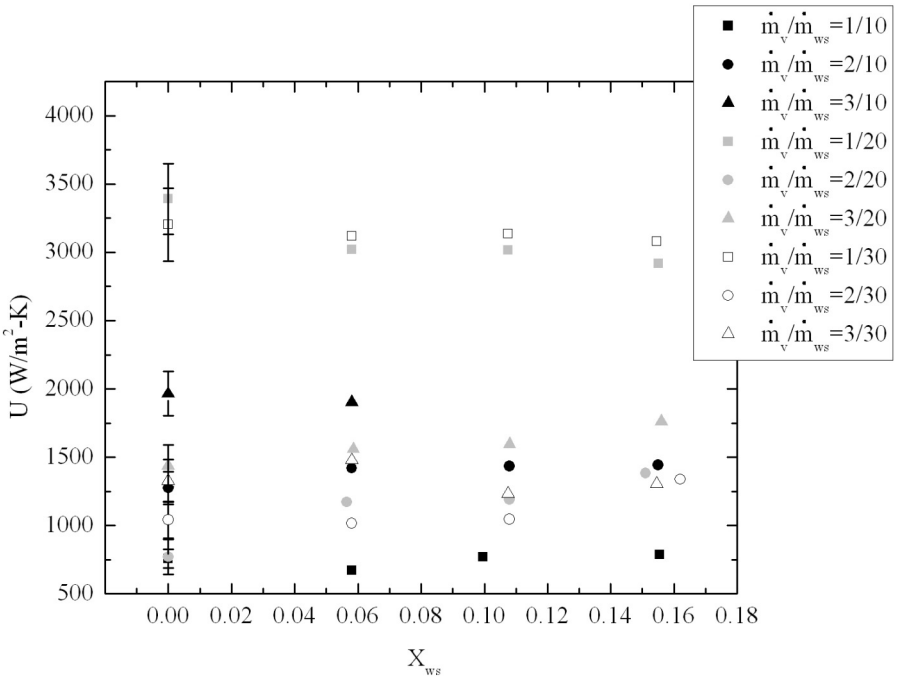

12 (a)

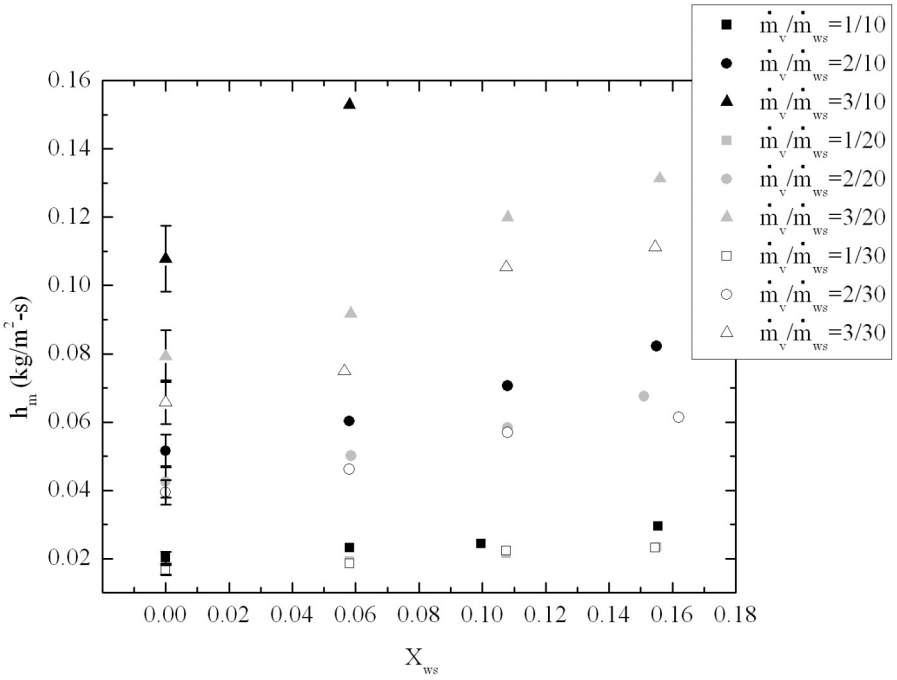

12 (b)

Fig. 12. Effect of X_{ws} on (a)U and (b)h_m for all flow ratios, a system pressure of 2.5 bar and 150μm smooth channel depth

There appears to be little to no effect of the inlet concentration variation on U. Note that for the highest flow rate ratio of mv/mws= 3/10, incomplete absorption was observed for weak solution mass concentrations larger than five percent. Considering only heat transfer attributes, the lowest flux ratios, namely, mv/mws of 1/20 and 1/30, appear to be the most desirable operating flow rate ratios within the parameter range presented.

Whereas it is expected that high heat transfer coefficients are achieved using microchannel flows, the combined heat and mass transfer characteristics need to be considered in order to identify the desirable operating conditions. Figure 12b shows the effect of inlet concentration variation on h_m for all flow ratios studied in the 150 μm absorber for a system pressure of 2.5 bar. As shown in Fig. 2b, for a fixed flow rate ratio, the mass transfer coefficient increases with inlet weak solution concentration. This increase is a result of a decrease in mass transfer driving potential, ΔX_{lm} for higher inlet concentrations. For a fixed inlet weak solution concentration and mass flow rate, h_m increases with vapor mass flow rate. Note that the driving potential for mass transfer for lower vapor flow rate is larger for a fixed weak solution flow rate and concentration. A combination of lower vapor flow rate and increased ΔX_{lm} results in a net decrease in h_m; see Eq. 9.

A comparison of Fig. 12a with Fig. 12b indicates that a desirable operating flow rate ratio, considering both heat and mass transfer effects is exhibited in the highest ammonia flux case of mv/mws= 3/10. Although the 1/20 and 1/30 cases have a higher U than the 3/10 flow rate ratio, they do not exhibit high mass transfer coefficients.

6.4 Channel Depth Effects

Figure 13a shows the overall heat transfer coefficient variation with microchannel depth. The experiments for the data shown in this figure were performed at a pressure of 4 bar and an inlet mass concentration of weak solution of 15 percent. At the lowest flow ratios of 1/20 and 1/30, with an increase in channel depth, the overall heat transfer coefficient decreases. Because the coolant side resistance remains constant for different solution microchannels, a decrease in the overall heat transfer coefficient is directly proportional to a decrease in the solution side convective heat transfer coefficient. Interestingly, for larger mass flow ratios, a substantial increase in U is observed from 150 μm to 400 μm absorber, after which U drops for the 1500 μm case. For example, for the mass flow ratio of 3/30, U increases from 1,090 W/m^2-K for the 150 μm absorber to 3,850 W/m^2-K for the 400 μm absorber and then decreases to a value of 1,760 W/m^2-K for a 1500 μm absorber. This suggests that there may exist an optimum channel depth for flow rate ratios larger than 1/20. The causes for this trend are not completely clear; however, one plausible explanation is put forth here. From a heat transport perspective, at least three competing effects are to be considered: (a) a reduction in the heat exchange area due to potential of vapor contact with bottom microchannel wall, and (b) enhanced mixing in the local solution due to the injected vapor, and (c) reduced heat transport from the liquid-vapor interface to the heat exchange surface due to increased liquid layer thickness and the corresponding heat transfer resistance. In condensation within a tube, there exists a thin liquid layer in between the co-flowing vapor and liquid. However, in the present absorber configuration, because ammonia vapor is injected in a cross-stream direction, there is

a potential for vapor to impinge on the bottom wall and thereby be in direct contact with the heat exchange surface. Such a situation has been verified by visualization experiments for the 150 μm channel absorber; see Fig. 10a. In reality, a combination of factors (b) and (c) occurs and it is not possible to distinguish between their individual effects on U.

Consider a situation in which there exists identical vapor and weak solution flow rates for all three microchannel absorbers (say, for example, a flow rate ratio of 3/30). On an average over the entire absorber, a fixed vapor flow rate implies that there will be larger amount of vapor in contact with the heat exchange surface for a 150-μm absorber compared with the 400-μm and 1500-μm absorbers based on volume constraints for incompressible fluids. Thus, the area for heat exchange is reduced, and hence U for a 150-μm absorber is lower than for the 400-μm absorber. For the 1500-μm absorber, although the vapor contact area with the heat exchange area is expected to be lower than that for the 400-μm absorber, there is an added resistance to heat transfer due to the additional liquid layer between the local liquid-vapor interfaces. From the results, it is seen that this increased liquid resistance has a greater effect than the reduced vapor contact with the heat exchange area. Hence there is a net decrease in the solution-side heat transfer coefficient, and thus a decrease in U compared with the 400 μm absorber is observed.

Figure 13b shows the effect of channel depth on the mass transfer coefficient, h_m for the same conditions as in Fig. 13a. Two distinct trends are observed. For the low vapor flow rates of 1 g/min, the effect of channel depth on h_m is negligible.

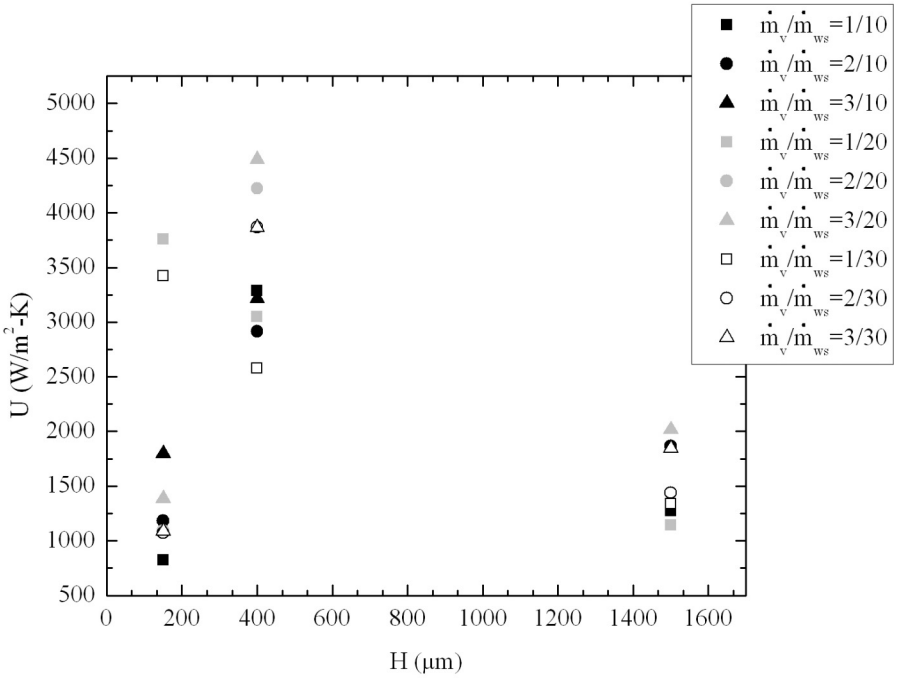

13 (a)

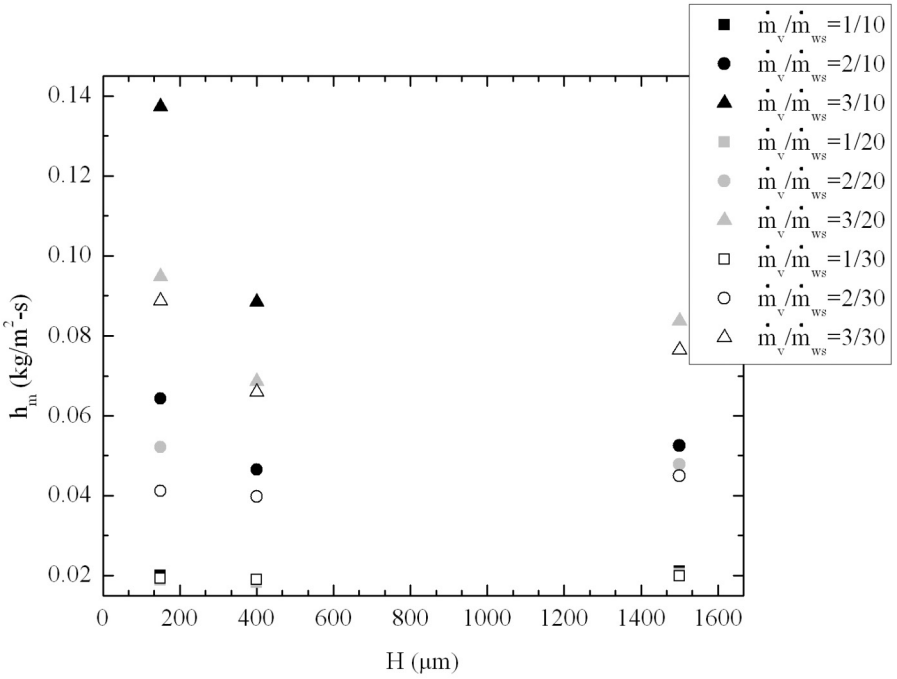

13 (b)

Fig. 13. Effect of smooth channel depth on (a) U and (b) h_m for X_{ws} =15% and a system pressure of 4 bar

Note that these are the conditions for which U decreases with increase in channel depth (see Fig. 13a). For the larger vapor flow rates, h_m decreases quite rapidly from the 150-μm to the 400-μm absorber, and increases gradually from 400-μm to the 1500-μm absorber. This trend is the inverse of that seen for U in Fig. 13a and is a consequence of the difference in temperature change from inlet to exit of the absorbers. For the lower flow rate ratios, this temperature change is not substantial; hence, the saturation concentration at the exit does not vary significantly from that at the inlet. For the higher flow rate ratios, a smaller mass transfer driving potential exists for the 150-μm absorber compared with the 400-μm absorber as a result of the higher temperature at the exit for this absorber, and thereby, a lower exit saturation concentration.

A comparison of U and h_m trends (Figs. 13a, and 13b, respectively) indicates that for fixed h_m and vapor flow rate, the corresponding U is higher for the 400-μm absorber. For example, consider a h_m of approximately 0.09 (kg/m^2-s). This includes the flow rate ratio of 3/10 for the 400-μm channel, as well as the flow rate ratios of 3/20 and 3/30 for the 150 μm channel. For these conditions, Fig. 13a indicates that U for the 400-μm absorber is considerably larger than that for the 150-μm absorber.

The three factors that were put forth to explain the heat transfer trends also affect the mass transfer performance of the absorbers. Increase in vapor contacting the heat exchange area results in net decrease in interfacial area for mass transfer between the liquid and vapor. Increased mixing of the fluid surrounding the vapor results in a lower resistance to mass transfer on the liquid side. Increased liquid layer thickness results in an increased resistance to mass transfer on the liquid side. Consider the

situation in which there exists identical vapor and weak solution flow rates for all three microchannel absorbers (say, for example, a flow rate ratio of 3/30). Thus, if the mass transfer coefficient was calculated based on the net interfacial areas between the vapor bubbles and the liquid, it would be expected that the mass transfer coefficient of the 400-μm absorber be smaller than that of the 150-μm absorber. Also, the competing effects of increase in interfacial area and increased mass transfer resistance on the liquid side for the deeper absorber channels would cause a decrease in h_m with channel depth. Thus, the trends shown in Fig. 18b indicate that the h_m for 150-μm is substantially larger than for the 400-μm absorber. As mentioned earlier, the temperature difference between the inlet and exit of the absorbers causes the driving potential to decrease for the 150-μm absorber compared with the 400-μm absorber. Because the heat transfer rate in the 400-μm absorber was substantially larger for the identical flow rate ratio compared with the 150-μm channel, the exit temperature on the solution side was also lower; thereby the log-mean concentration difference in the absorber was lower than for the 150-μm absorber. Also, because the flow rate of vapor was fixed in both cases, this translates to a net lower mass transfer coefficient for the 400-μm absorber.

Based on the above discussion, the 400-µm absorber seems to be the most desirable geometry considering both heat and mass transfer attributes among the absorber dimensions varied in this study. The flow ratio of 3/10 yields the most desirable flow conditions for both 150-µm and 400-µm absorbers. Whereas h_m at this flow rate ratio for the 400-µm absorber is 64 percent that of the 150-µm absorber, the corresponding U is 79 percent larger compared with the 1500-µm absorber. Perhaps a microchannel depth that has the most desirable heat and mass transfer characteristics lies in between these two channel depths for this flow rate ratio.

6.5 Microchannel Geometry Comparison

6.5.1 Heat Load

Figures 14-18 detail the results for various geometries for a system pressure of 4 bar and an inlet concentration of 15 percent. Figures 14 a and b present the absorber heat load per unit mass flow rate, $\dot{q}_{abs}/\dot{m}_{ss}$ of the strong solution for weak solution flow rates of 10 and 30 g/min, respectively.

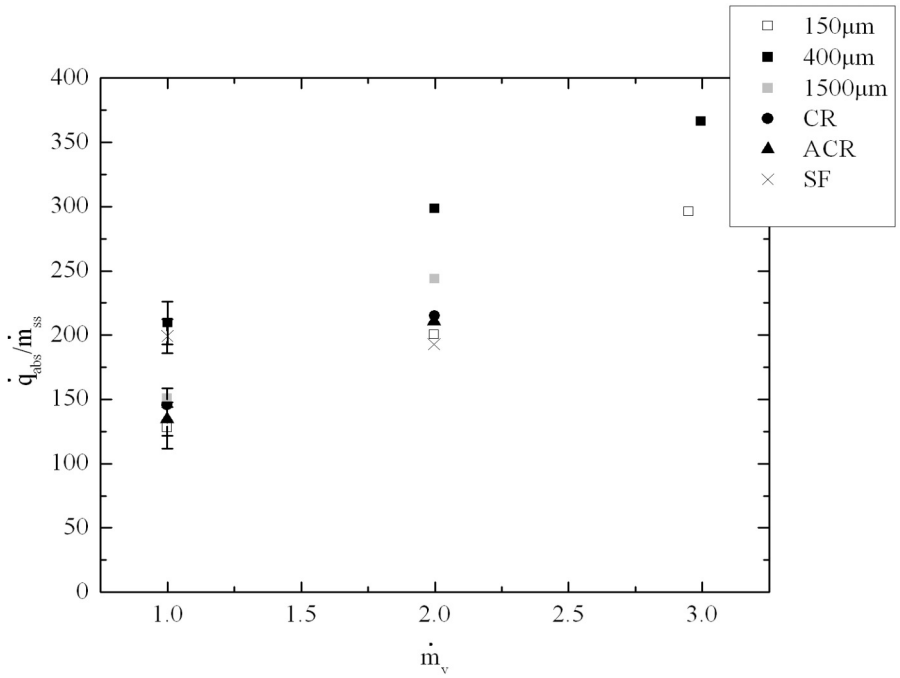

14 (a)

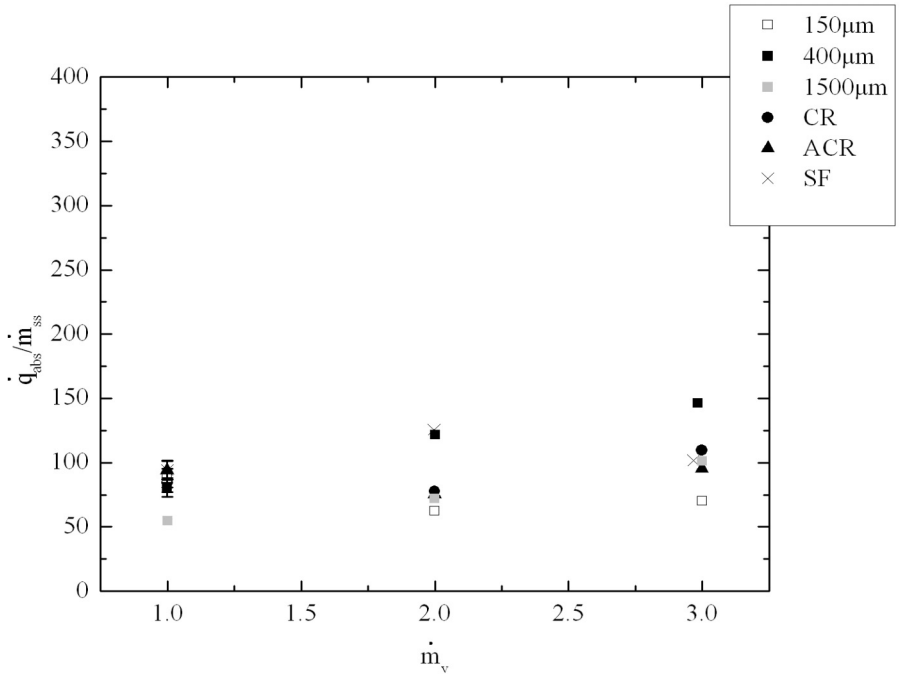

14 (b)

Fig. 14. Variation of absorber heat load per unit mass flow rate of the strong solution with vapor flow rate(g/min) for the six geometries (a) $\dot{m}_{ws}$ =10g/min,(b) $\dot{m}_{ws}$ =30g/min

Clear from both figures, is the reduction of $\dot{q}_{abs}/\dot{m}_{ss}$ for a fixed vapor and increasing weak solution flow rate. Also, as $\dot{m}_v$ increases for constant $\dot{m}_{ws}$, $\dot{q}_{abs}/\dot{m}_{ss}$ also increases. Notice that for low vapor and high solution flow rates in Fig. 14b, all the geometries seem to converge to nearly the same heat load, with the exception of the deepest channel. Predominant in both figures is the high heat load exhibited for the 400μm channel.

6.5.2 Log Mean Temperature and Concentration Difference

Figure 15a and 15b presents the log mean temperature difference ΔT_{lm} and log mean concentration difference ΔX_{lm} for various vapor flow rates and all geometries at a weak solution flow rate of 10 g/min, respectively. The driving potential for heat transfer, ΔT_{lm} is the lowest for the 400-μm channel. However, the driving potential for mass transfer, ΔX_{lm} is highest for the this channel. This is because the nominal inlet weak solution concentration (X_{ws}) and it's saturated value ($X_{ws,sat}$), as well as the exit concentration (X_{ss}) remain fixed, while the saturated concentration at the exit ($X_{ss,sat}$) is ultimately driven up for a lower strong solution temperature, resulting in a higher ΔX_{lm}.

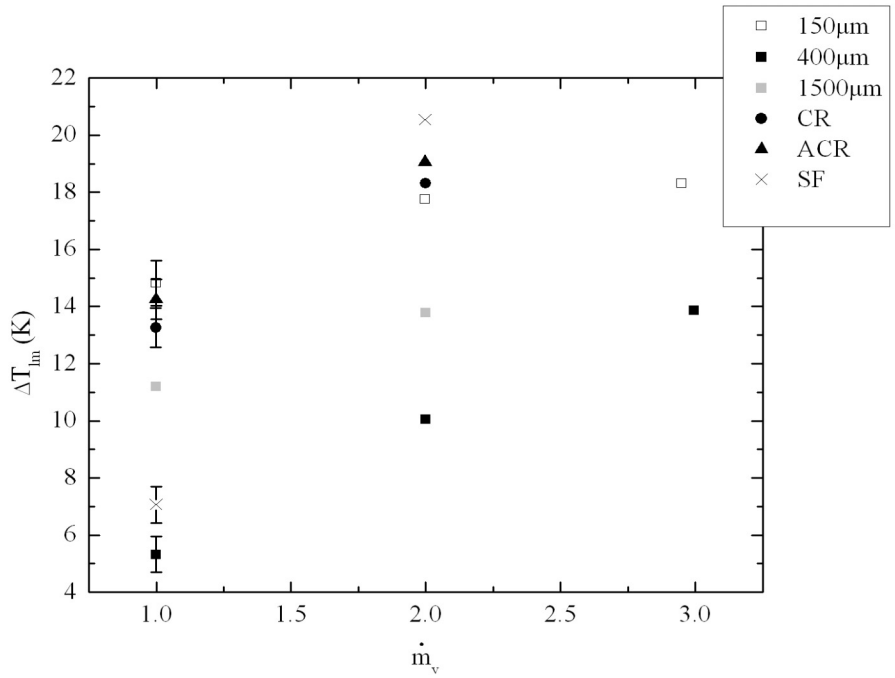

15 (a)

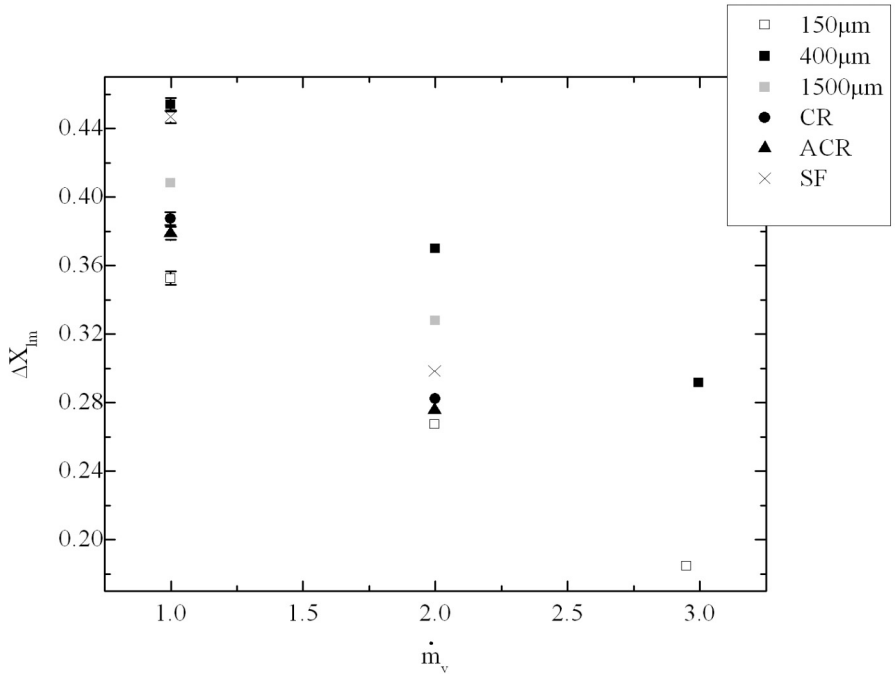

15 (b)

Fig. 15. Effect of vapor flow rate (g/min) on (a)ΔT_{lm} and (b)ΔX_{lm} for the six geometries at a system pressure of 4 bar, X_{ws}=15%, and $\dot{m}_{ws}$ =10 g/min

Figures 16a and 16b are the same as the previous figures, only with a weak solution flow rate of 30 g/min. Similar to the preceding figures the 400-μm channel maintains the lowest ΔT_{lm} for most cases. However, for the lowest vapor flow rate case the SF and 150-μm achieve the lowest ΔT_{lm} which, if the energy transferred to the cooling water was fixed, would be an indicator of superior performance. However, this is not always the case, and as shown in Fig. 14 the heat load varies from one case to the next. In order to get a better idea of overall heat and mass transfer performance, attention must be directed to the overall heat transfer and mass transfer coefficients, U and h_m.

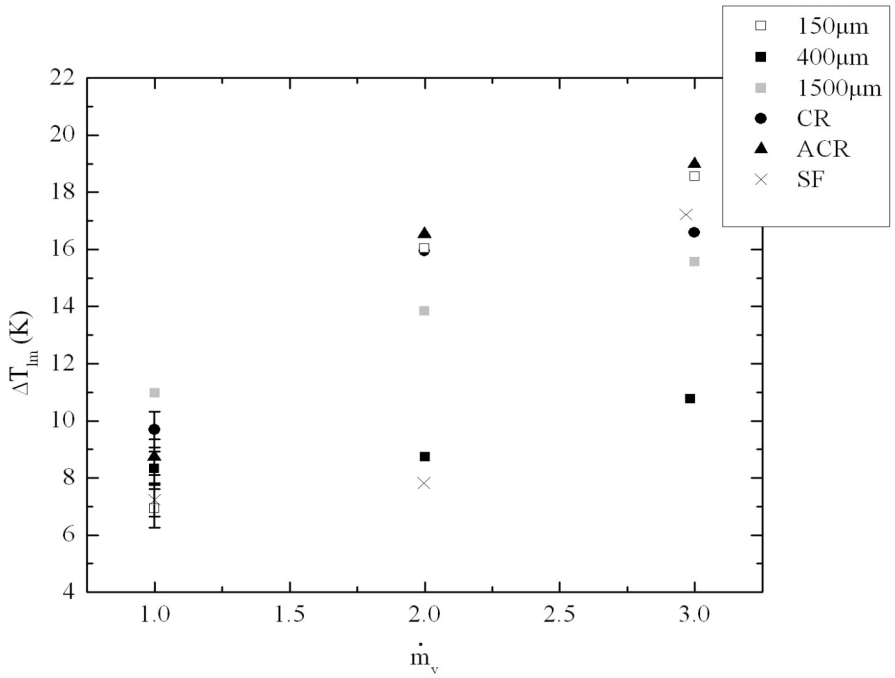

16 (a)

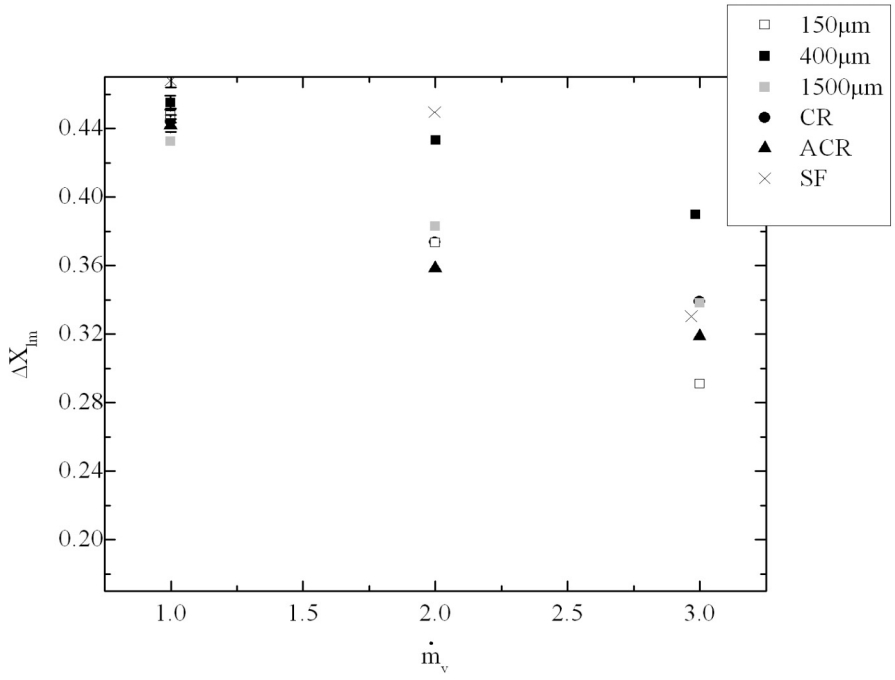

16 (b)

Fig. 16. Effect of vapor flow rate (g/min) on (a)ΔT_{lm} and (b)ΔX_{lm} for the six geometries at a system pressure of 4 bar, X_{ws}=15%, and $\dot{m}_{ws}$ =30 g/min

6.5.3 Overall Heat and Mass Transfer Coefficients

Figure 17a shows the effect of vapor flow rate on U for all microchannels for a weak solution flow rate of 10 g/min. Also shown for comparison is U of the 150-μm, 400-μm, and 1,500-μm absorbers. The trend in U for the 400-μm absorber clearly stands apart; on average over all vapor flow rates, this absorber indicates a 270 percent increase over the 150-μm absorber. The trend in U with vapor flow rate variation is not clear for this absorber, and the slight variations with vapor flow rate are within the reported uncertainty.

The CR and ACR absorbers, as well as the 150-μm and 1500-μm absorbers show a gradual increase in U with increasing vapor flow rate. At the low vapor flow rate of 1 g/min, the CR absorber exhibits a 27 percent increase in U and the 1500-μm absorber a 54 percent increase in U compared with the 150-μm absorber. In contrast, U for the ACR absorber is slightly lower than that of the CR absorber and approximately the same as that of the 150-μm absorber. This is a consequence of the smaller number of ribs in the ACR absorber which results in less frequent renewal of the hydrodynamic and thermal boundary layers on the heat transfer surface. In addition, the low solution flow rate and the large aspect ratio of this absorber could have been contributing factors for the lower heat transfer coefficient of the ACR compared with the CR absorber at the low vapor flow rate of 1 g/min. The difference in U between these absorbers becomes negligible for the 2 g/min vapor flow rate. Note that the vapor flow rate of 3 g/min for all structured absorbers and the 1500-μm absorber at this weak solution flow rate resulted in incomplete absorption as indicated by visual observation at the exit of the absorber test section and hence, is not shown.

The increasing trend in U for the 150-μm, CR, and ACR absorbers can be put forth based on the three competing effects discussed earlier. With an increase in flow rate, the potential for vapor contact with the walls increases, thereby decreasing the heat transfer rate. At the same time, mixing is enhanced significantly due to injection of more vapor into the absorber. For the 400-μm absorber, these competing effects seem to largely balance each other resulting in little variation with vapor flow rate. However, the enhanced mixing seems to offset reduction in heat transfer area for the 150-μm, CR, and ACR absorbers, resulting in a net gradual increase in U with vapor flow rate.

In contrast to the trends seen for the 150-μm, CR and ACR absorbers, U for the SF absorber is very large (2,700 W/m^2-K) at a low vapor flow rate of 1 g/min, and decreases dramatically to 900 W/m^2-K at a vapor flow rate of 2 g/min. At the lower vapor flow rates, it is possible that solution covered the tip of the ribs thereby enhancing the surface area over the smooth 150-μm absorber by 15 percent. However, with an increase in vapor flow rate, it is possible that the injected vapor covered the tips of the ribs, thereby reducing the effective area for convective heat transfer by 20 percent, and hence the solution-side and overall heat transfer coefficients. Note that at this low solution flow rate of 10 g/min, the liquid solution inertia may be insufficient to shear the vapor pinned to the top of the ribs for the larger vapor flow rate of 2 g/min.

The effect of vapor flow rate on mass transfer coefficient for a weak solution flow rate of 10 g/min is shown in Fig. 17b for all absorbers. The mass transfer coefficient at the low vapor flow rate of 1 g/min is similar for all absorbers. With an

increase in vapor flow rate, the mass transfer coefficient of each absorber increases. At a vapor flow rate of 2 g/min, the mass transfer rate of the 150-μm absorber is the largest and the trends seen in h_m are inverse of that seen in Fig. 17a for U. Because the vapor flux rate is fixed, this implies that ΔX_{lm} is in inverse proportion to h_m for the absorbers. With an increase in vapor flow rate, the difference between the mass transfer coefficient of the 150-μm and 400-μm absorbers increases.

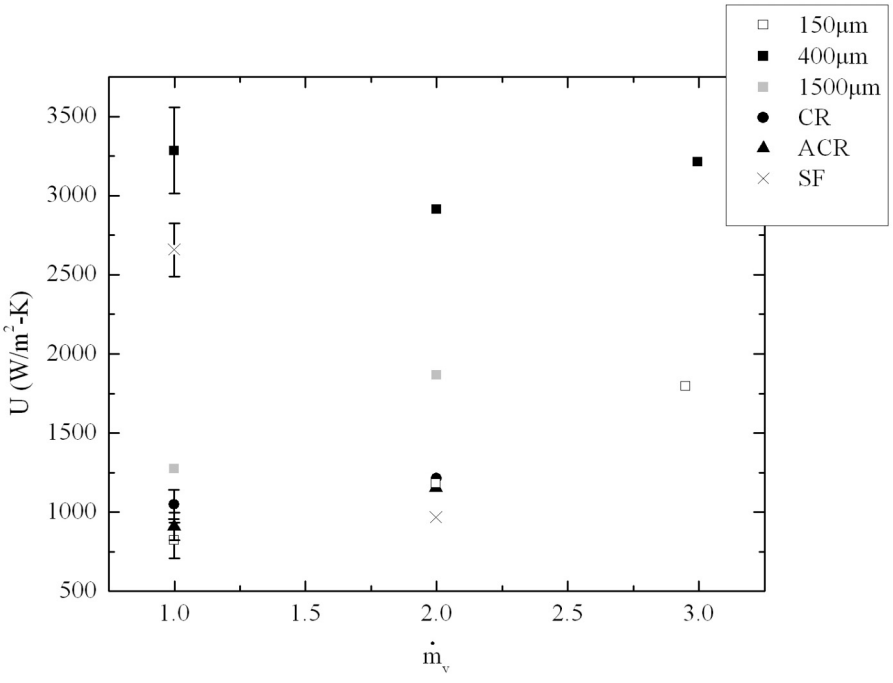

17 (a)

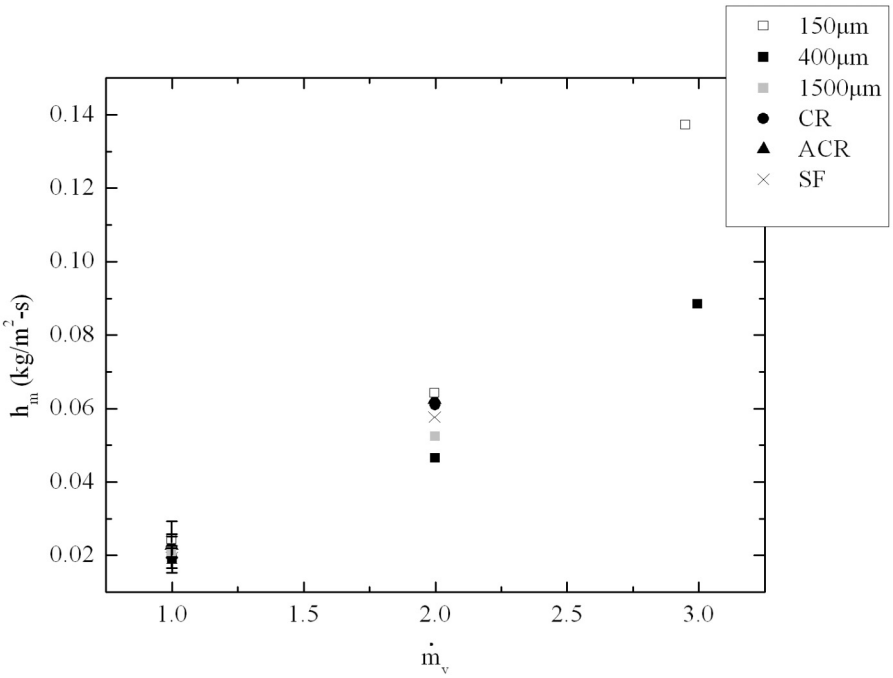

17 (b)

Fig. 17. Effect of vapor flow rate (g/min) on (a)U and (b)h_m for the six geometries at a system pressure of 4 bar, X_{ws}=15%, and $\dot{m}_{ws}$ =10 g/min

Figure 18a shows the variation of U with vapor flow rates in a similar manner as in Fig. 17a, but for a larger weak solution flow rate of 30 g/min. Data have also been obtained for a 20 g/min vapor flow rate but are not presented here for brevity; these data also show similar trends to that indicated in Fig. 18a. At the outset, it is clear that the trend of variation of U with vapor flow rate for most absorbers is very different from that shown in Fig. 17a for the lower solution flow rate of 10 g/min. At a low vapor flow rate of 1 g/min, the 150-μm and SF absorbers exhibit the largest U, followed by the ACR, 400-μm, CR, and 1500-μm absorbers, in that order. This trend is to be expected for smooth-bottom-wall absorbers because at a low flux ratio of 1/30, the flow approaches a single-phase laminar flow; channels with smaller hydraulic diameters have larger heat transfer coefficients. However, the trend changes at a high

vapor flow rate. For example, at 3 g/min, the 400-μm absorber has a U of 3750 W/m^2-K as compared with 1200 W/m^2-K of the 150-μm absorber. The substantial decrease in U of the 150-μm absorber can be attributed to the increase in the amount of vapor contacting the heat exchange surface, as discussed previously in relation to channel depth variation.

Also of interest, is the insensitivity of U for vapor flow rates of 2 g/min and 3 g/min for the 150-μm and 400-μm absorbers. It is possible that at these vapor flow rates, the competing effects of vapor contact with the heat exchange area, mixing enhancement caused by vapor injection, and liquid layer resistance, balance almost exactly at both vapor flow rates. More plausible is the explanation that the overall heat transfer coefficient is limited by the combination of the conduction resistance across the stainless steel wall material between the microchannel and coolant, and the coolant side heat transfer coefficient, for the 400-μm absorber. On the other hand, it may be limited by the low absorber-side heat transfer coefficient for the 150-μm absorber. The combined conduction and coolant-side convective resistance per unit heat flux was kept constant among all absorbers tested and was $7 \cdot 10^{-4}$ m^2-K/W. If the absorber-side convective resistance were small, the overall heat transfer coefficient would be 1422 W/m2-K.

The ACR absorber U is 25 percent larger than the CR absorber at low vapor flow rate of 1 g/min; however, the trend is reversed for the largest vapor flow rate of 3 g/min, where U for ACR is 42 percent lower than that of the CR absorber. Both of these absorbers show a substantial decrease in U with increase in vapor flow rate from 1 g/min to 2 g/min and a very gradual increase from 2 to 3 g/min. Among the

structured microchannels, the trend of U with vapor flow rate for the SF channel is particularly worth mentioning. At 1 g/min, the U is the largest (along with the 150-μm absorber) of all absorbers. With an increase in vapor flow rate to 2 g/min, U further increases to 4,500 W/m2-K, followed by a dramatic decrease to 1400 W/m2-K at a vapor flow rate of 3 g/min. The reasoning behind this trend follows that given for the 10 g/min weak solution flow rate. At the first two vapor flow rates, the inertia of the flow is sufficient to shear the vapor bubbles that accumulate on the top of the ribs, whereas vapor has sufficient velocity to contact the top of the ribs for the last flow rate, reducing the effective heat exchange area, and hence, the heat transfer coefficient.

One trend that remains consistent between the 10 g/min flow condition (see Fig. 17a) and the 30 g/min condition in Fig. 18a is that of U variation for the 1500-μm absorber. At a vapor flow rate of 1 g/min, U is 1300 W/m^2-K, and it increases gradually to 2000 W/m^2-K at vapor flow rate of 3 g/min. It seems that the enhancement of mixing is more dominant than the increase in vapor contact with the heat exchange surface and increase in the liquid layer resistance for this channel. Nevertheless, U for this absorber at any vapor flow rate is significantly lower than that of the 400-μm absorber.

Figure 18b presents h_m variation with vapor flow rate for a weak solution flow rate of 30 g/min for all absorber geometries studied. The trends are similar to that seen in Fig. 17b for the 10 g/min weak solution flow rate. The values of h_m are lower for each absorber compared with Fig. 17b due to the larger flow rate causing a lower ΔX_{lm}.

Comparing Fig. 18a with Fig. 18b, in light of the limiting characteristic in U for the 400-μm and 150-μm absorbers, and the absence of such a limit in h_m, it is clear that these channels are heat transfer limited. Due to the high limit for the 400-μm channel and the low limit for the 150-μm channel, it is conjectured that the heat transfer is limited on the solution side for the 150-μm channel and on the coolant side for the 400-μm channel.

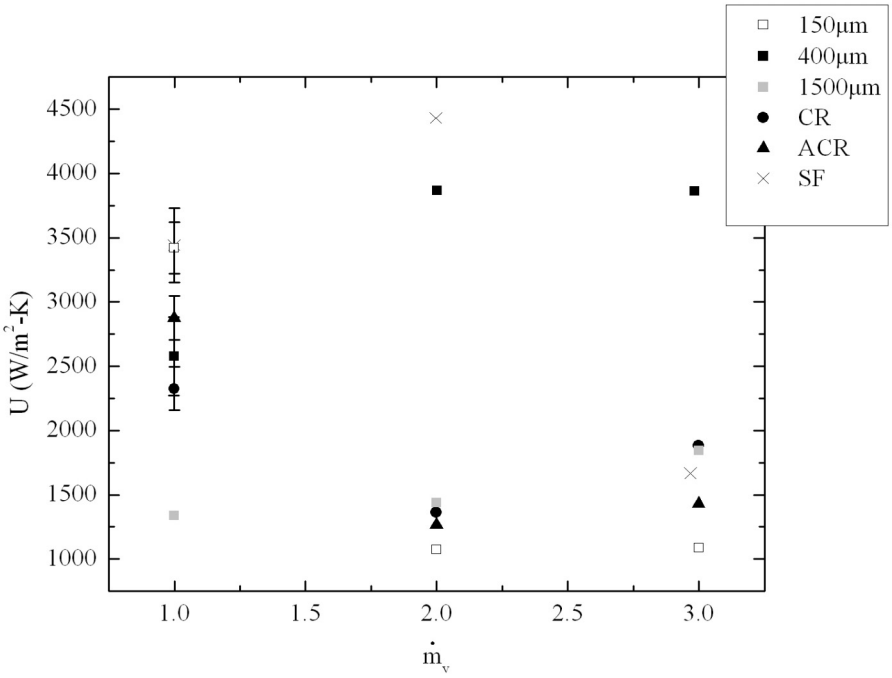

18 (a)

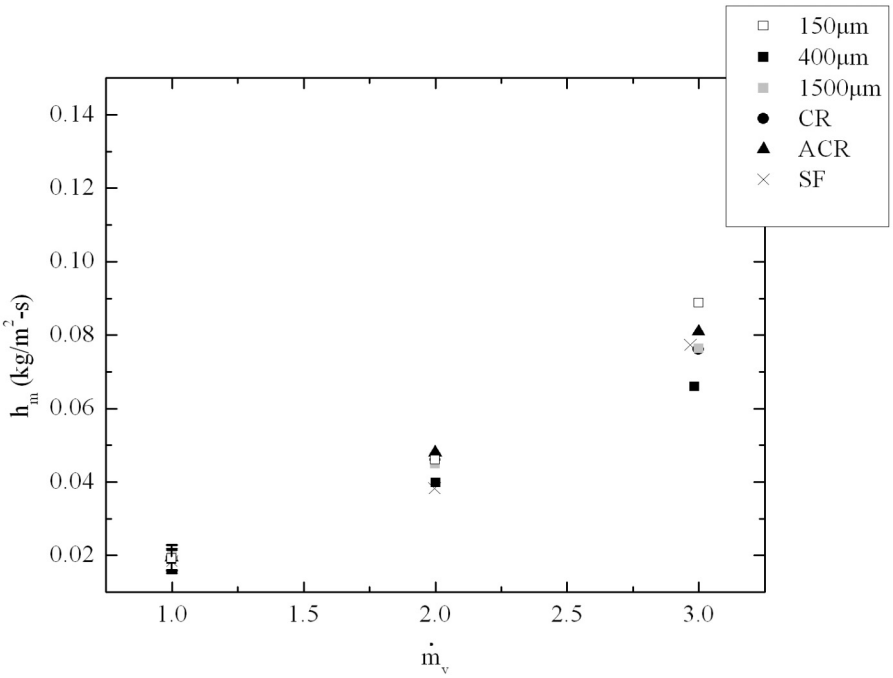

18 (b)

Fig. 18. Effect of vapor flow rate (g/min) on (a)U and (b)h_m for the six geometries at a system pressure of 4 bar, X_{ws}=15%, and $\dot{m}_{ws}$ =30 g/min

6.6 Effect of Heat of Absorption

In order to better understand the effect of the heat of absorption on the heat and mass transfer coefficients, it is instructive to plot these coefficients versus a ratio of the source to heat rates, $\dot{s}/\dot{q}$. The term $\dot{s}$ refers to the source rate accounting for the additional heat generation due to the ammonia absorption within the hot side of the heat exchanger.

Figure 19a shows U versus $\dot{s}/\dot{q}$ for the 150-μm absorber at a working pressure of 2.5 bar and for various flow rate ratios and inlet concentrations. It is clear that U has a large value of around 3000 W/m^2-K for a low $\dot{s}/\dot{q}$; however, when this quantity approaches unity and beyond, U tends to lower values. With the exception of the flow rate ratio of 1/10, for $\dot{s}/\dot{q}$ >1, U is bounded between 1000 W/m^2-K and 1500 W/m^2-K.

As expected, a large U is achieved for the lowest flow rate ratio cases, 1/20 and 1/30. The 10 g/min weak solution flow rate conditions show and increase in U as the vapor flow increases. The U is much lower than the 1/20 and 1/30 cases for the 10 g/min cases because the high influx of vapor reduces the overall heat transfer area, and also the solution flow rate is much lower. For all of the cases, other than 1/20 and 1/30, and increase in flow ratio results in a net increase in U, the trend being most obvious for the 10 g/min cases. Figure 19b shows h_m versus $\dot{s}/\dot{q}$ for the 150-μm absorber. For a low $\dot{s}/\dot{q}$ value, h_m is quite low, and is highest as $\dot{s}/\dot{q}$ approaches unity, coincidently corresponding to the highest flow rate ratio cases. As the flow rate ratio increases, h_m increases just as U increases in Fig. 19a.

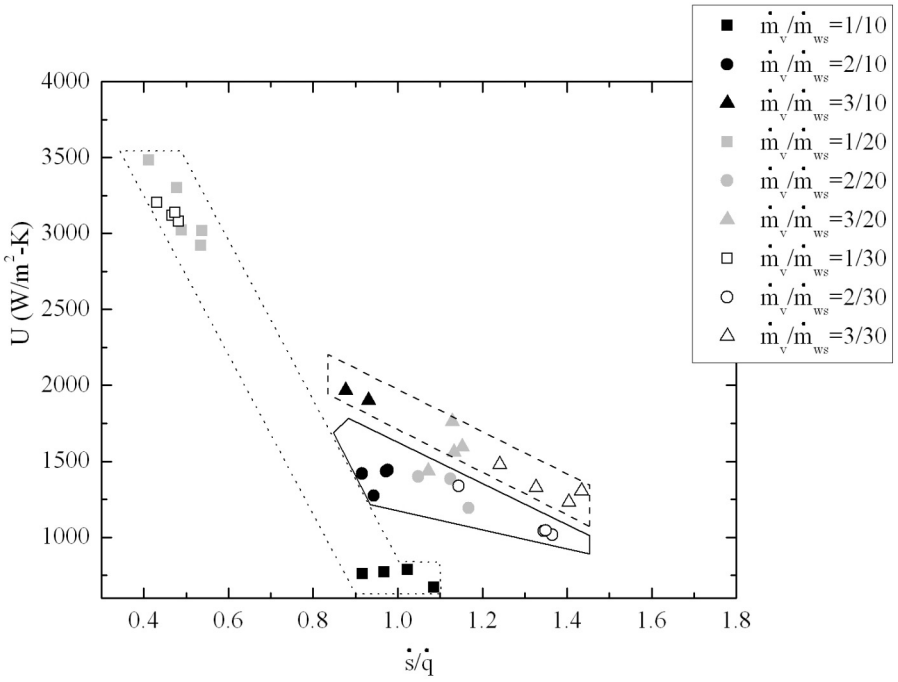

19 (a)

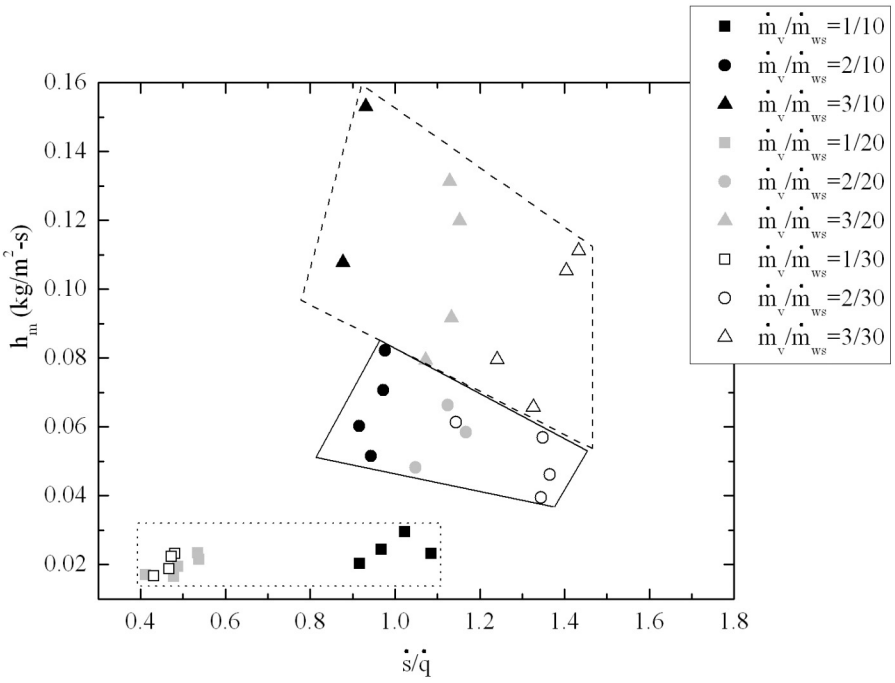

19 (b)

Fig. 19. Effect of the heat generated to heat removed ratio on (a)U and (b)h_m for all $\dot{m}_{ws}$ and X_{ws}, a system pressure of 2.5 bar, and 150μm smooth channel depth

7 Model Development

Due to the nature of the global experiments performed in this study, it is difficult to truly understand what might be occurring locally within the absorber. If a model can be developed that accurately predicts local absorption and heat transfer rates, the difficulty in performing experimental parametric studies could potentially be eliminated. A model of this absorber is an imperative tool that will better predict absorber performance and size. Presented in this section is the development of a 1-D model to predict the concentration and temperature distribution along a smooth absorber microchannel. Preliminary results obtained by assuming complete absorption of vapor into each differential control volume of the absorber are presented. Such a model is valid on a global basis over the entire absorber for the experimental

conditions reported in the thesis because no vapor bubbles were seen exiting the absorber. Further, an approach to numerical modeling of incomplete absorption within a control volume is also presented. Parameters that need to be determined to complete this model are identified.

7.1 Model Geometry

Figure 20 shows schematically the absorber idealized as a heat exchanger. A differential control volume within the hot-side and cold-side of the heat exchanger is indicated along with the energy fluxes in and out of this control volume. Recall that because there is heat generation within the control volume on the hot side, an additional source term, $\dot{s}'''$ within each control volume must be accounted. For the control volume on the cold side, the traditional energy fluxes without this source term apply. The forgoing analysis is simplified for a one-dimensional case and assumptions are presented therein.

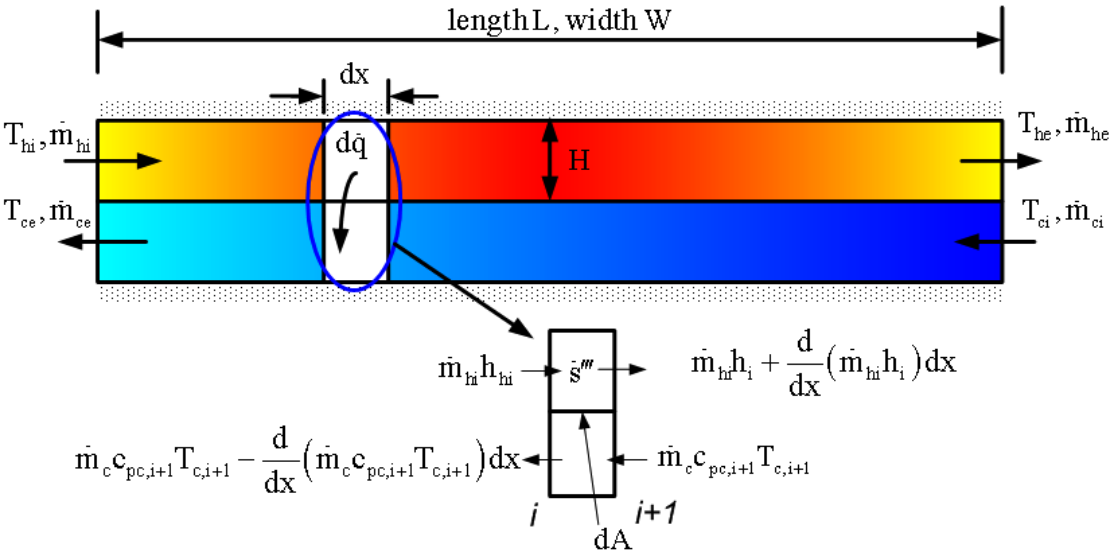

Fig. 20. Control volume for heat exchanger with generation of energy on one side- this is not the correct schematic

7.2 Governing Equations

General assumptions for the numerical model are as follows:

1) Steady State
2) One Dimensional
3) Constant props (on coolant side)
4) Absorption occurs instantaneously

Assumption three was used to estimate coolant density and specific heat at inlet/exit temperature averaged values.

The continuity equation can be simplified for both sides of the heat exchanger shown in Fig. 20, assuming steady-state and 1-D, to

$$\frac{d(\rho u)}{dx} dxdydz = d\dot{m}_v \tag{17}$$

Where the boundary condition is the inlet mass flow rate.

Additionally, the energy equation can be simplified for each side (cold and hot) using the following assumptions:

1) Neglect viscous dissipation
2) Neglect pressure work term
3) Average thermal conductivity on solution side with instant absorption of NH_3
4) Axial conduction is negligable

Given the aforementioned assumptions, the cold side energy equation can be reduced to

$$\tilde{n}c_p u\frac{dT}{dx} - \frac{d\dot{q}''}{\Delta z} = 0 \tag{18}$$

Using the enthalpy form of the energy equation, the hot side can be reduced to

$$\frac{d(\rho uh)}{dx} + \frac{d\dot{q}''}{\Delta z} = \dot{g}''' \tag{19}$$

where $\dot{g}'''$ is the volumetric generation of heat on the solution side. The boundary conditions for Eq. 18 and 19 are the coolant and weak solution inlet temperatures and flow rates, respectively.

Equations 18 and 19 are convection equations that can be discretized and solved numerically given the known inlet temperatures to the absorber. Note that in Eq. 19, the solution side velocity and density are continually changing in the region of vapor injection and absorption. The spatial flow acceleration achieved via mass injection is accounted for in the continuity equation, and fluid properties such as density and enthalpy of the solution are determined from the Ibrahim & Klein [17] ammonia-water property estimation routines mentioned in the results and discussion section. In order to couple the equations both of these reduced energy equations, the heat removed from the hot side must enter the cold side. This is taken into account in the discretization.

7.3 Discretization

The continuity equation, Eq.17, is discretized using a forward difference and reduces to

$$\left[(\rho u)_{i+1} - (\rho u)_i\right]dA - d\dot{m}_v = 0 \tag{20}$$

The exiting strong solution concentrations is found from

$$x_{ss} = \frac{\dot{m}_{ws} x_{ws} + d\dot{m}_v}{\dot{m}_{ss}} \tag{21}$$

The energy equation on the solution side, Eq. 19, can be discretized and reduced as follows:

$$\left[(\rho uh)_{i+1} - (\rho uh)_i\right]_S = \left(\dot{g}'''\Delta x - \frac{d\dot{q}'''\Delta x}{\Delta z}\right) \tag{22}$$

where the convection term is approximated using forward differencing. The coolant side energy equation discretization yields

$$\rho c_p u\left[T_{i+1} - T_i\right]_C = -\frac{d\dot{q}'''\Delta x}{\Delta z} \tag{23}$$

Equation 19 is approximated similar to Eq. 18, however, some attention should be given to why the sign on the heat flux term (coupling term) is negative. It would seem that if heat is removed from the solution side and added to the coolant side, the signs of $d\dot{q}''$ would be different, and they are. However, because the numerical solution marches from left to right, essentially marching forward along the hot side flow, but backward in the flow direction the coolant side (going from hot coolant outlet to cold coolant inlet), heat flux must be subtracted from the coolant side. At each incremental control volume heat transfer rate from the solution to the coolant can be found from

$$q'' = U(Ts_i - Tc_i) \tag{24}$$

where U is the overall heat transfer coefficient,

$$U = \frac{1}{\frac{1}{h_s} + \frac{t}{k_{ss}} + \frac{1}{h_c}} \tag{25}$$

The convective heat transfer coefficients can be found from

$$Nu = \frac{hD_h}{k} = 5.39 \tag{26}$$

where Nu is the Nusselt number, a constant for the high aspect ratio geometry with uniform heat flux and laminar flow [20]. Additionally, the volumetric generation term can be approximated by

$$\dot{g}''' = \frac{(hd\dot{m})_{NH3}}{dV} \tag{27}$$

A flow chart of the calculation procedure is given in Fig. 21. Property estimation algorithms by Daniels [21] are used at each control volume to determine the changing properties of the solution side due to the changing concentration of ammonia.

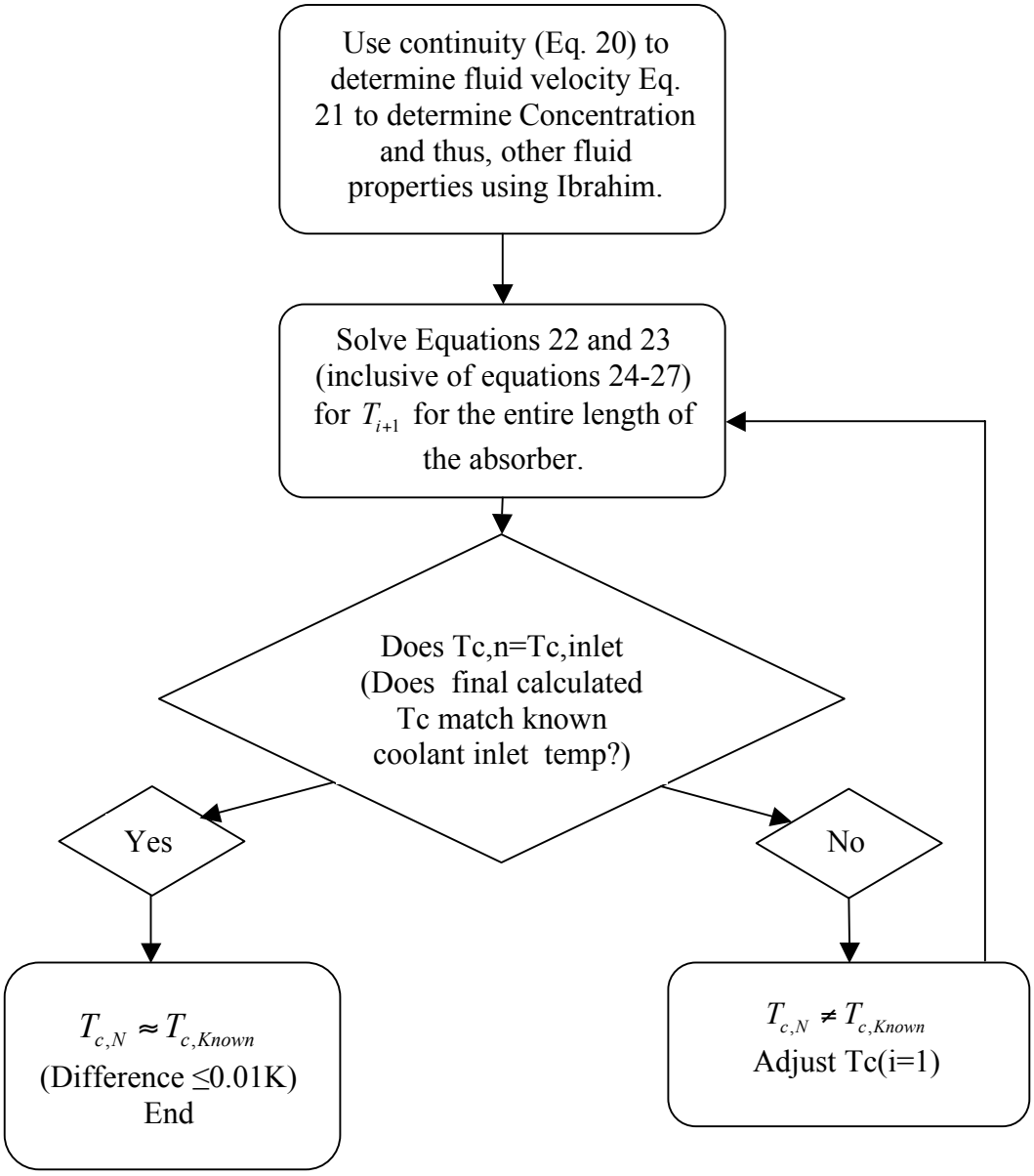

Fig. 21. Flowchart of algorithm for finding temperature/concentration profiles

7.4 Model Results

7.4.1 Validation and Grid Independence

The following figures correspond to the known solution and coolant inlet temps, 295.7K and 283.6K respectively, as well a fixed inlet concentration of 15 percent and pressure of 4 bar. The geometry for the coolant side was 10 cm x 2 cm x 870 μm. In order to validate the model, the numerical scheme was simplified further to maintain constant properties on both the hot (solution) and coolant side. There was no ammonia gas was introduced (no generation term), and as such, the solution side velocity and properties remained constant. The aforementioned simplifications made it possible to compare the numerical solution with the analytical solution given by [20]:

$$\Delta T_i = \left(T_{ws} - T_{co}\right)\exp\left(-U \cdot dA\left(\frac{1}{\dot{m}_s c_{p,s}} + \frac{1}{\dot{m}_c c_{p,c}}\right)\right) \tag{28}$$

$$\Delta T_i = T_s(x) - T_c(x) \tag{29}$$

Given fixed mass flow-rates of solution (30 g/min) and coolant (268.5 g/min), ΔT_{exact} can be compared with $\Delta T_{numerical}$. Figure 22 shows the comparison with a constant solution side concentration of 15 percent. Note that in order to solve ΔT_{exact}, $\Delta T_{numerical}$ must first be solved in order to obtain ΔT at the solution side inlet. The ΔT profile across the entire length of the absorber can then be predicted via the exact analytical solution and compared with the numerical profile. As the grid is refined from 10 to 1000 control volumes, the numerical solution slowly approaches the analytical solution, indicating a grid independent solution.

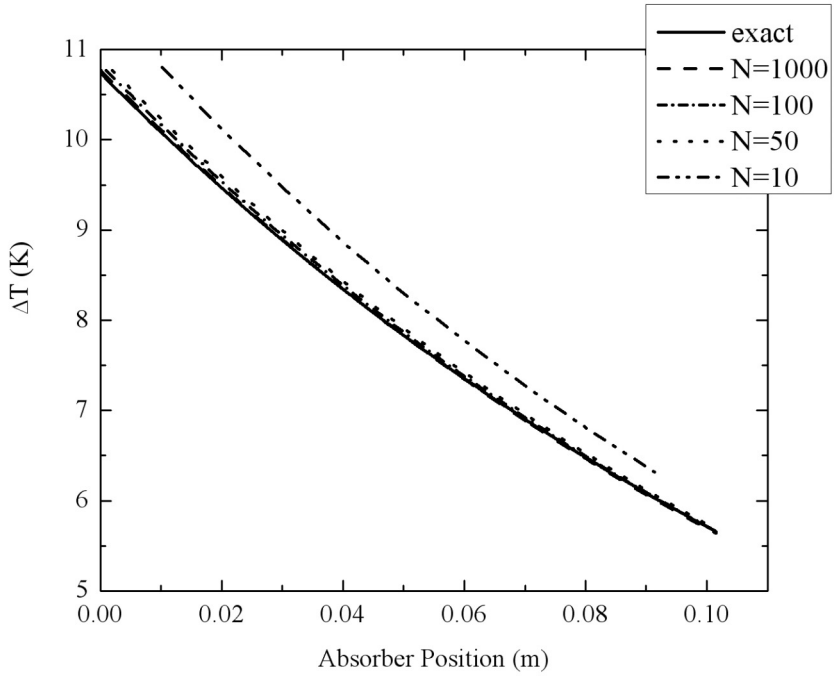

Fig. 22. ΔT versus axial absorber location for the numerical solution with N=10, 50, 100, 1000 control volumes as compared with the analytical (exact) solution for 150 μm channel at a pressure 4 bar and 15 percent inlet concentration

7.4.2 Parametric Studies

Of primary interest for this study is the heat and mass transfer performance during actual absorption. Introduction of ammonia vapor to the solution side generates energy and, under some circumstances, yields a higher outlet solution temp than the inlet. This behavior does not exist for a typical heat exchange analysis, with the hot side fluid usually cooling down from inlet to exit. Figure 23 details the effects of increasing the vapor flow rate on the solution and coolant temperature profiles. When the vapor flow rate increases, so to does the generation term. For $\dot{g}/\dot{q} > 1$, the exit temperature is higher than the inlet temperature of the solution (hot) side due to insufficient removal of heat for the given amount of generated heat.

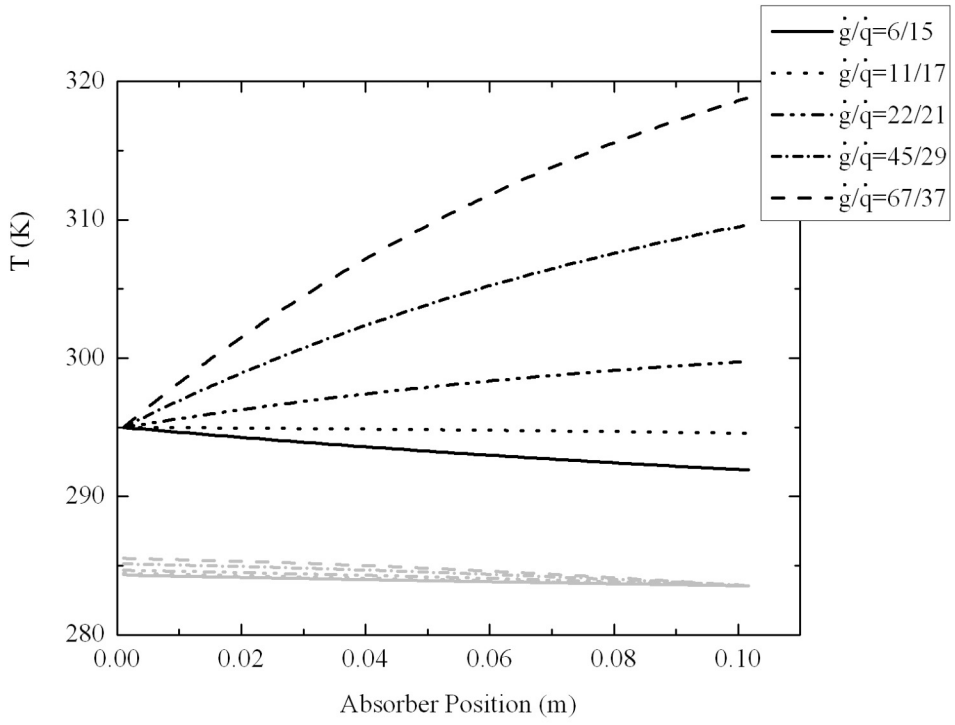

Fig. 23. Temperature profiles for the solution side (black) and coolant (gray) side fluids for various source/heat ratios, ġ/q̇ along the horizontal length (solution flow path) of the absorber

Figure 24 shows the effect of increasing the weak solution flow rate for a fixed ammonia vapor mass flow rate of 1 g/min. A higher $\dot{m}_v / \dot{m}_{ws}$ results in an increase in the exit temperature. The source term is constant for these three cases because the mass flow rate of the vapor is fixed, thus, the increase in exit temperature is due to the reduction in flow rate of the solution.

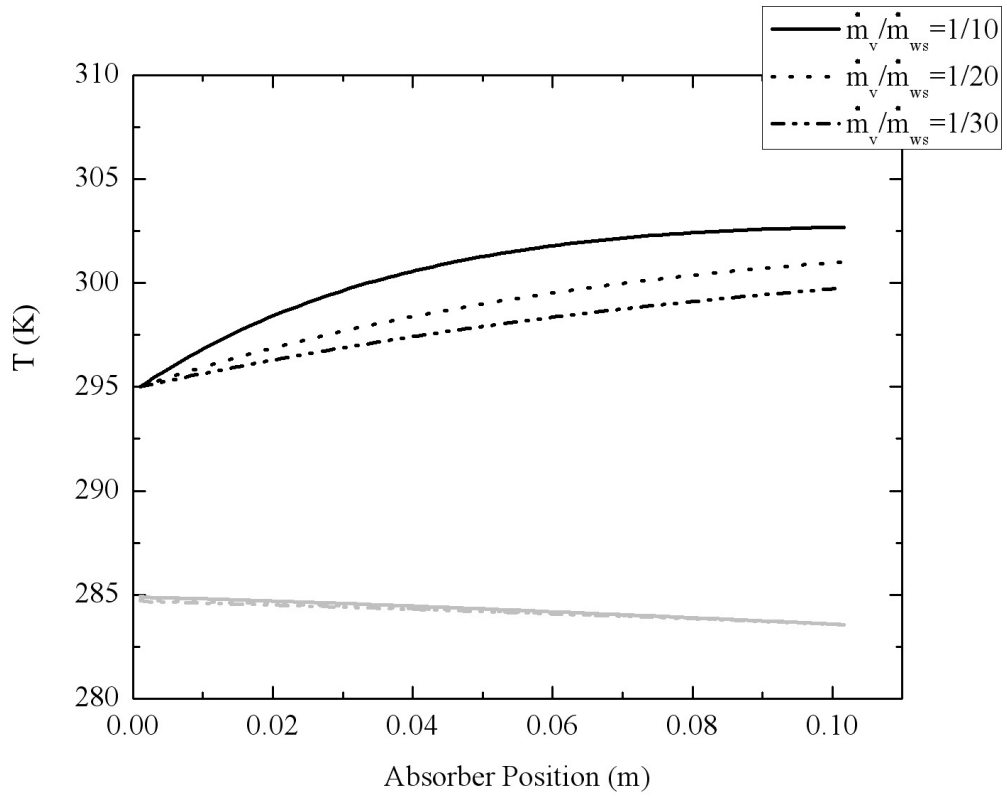

Fig. 24. Temperature profiles for the solution side (black) and coolant side (gray) fluid for $\frac{\dot{m}_v}{\dot{m}_{ws}} = \frac{1}{10}, \frac{1}{20}, \frac{1}{30}$

In order to determine mass transfer attributes of the absorber, the concentration along the length of the channel must be known. Figure 25 shows the concentration profile for all the mass flow rate ratios considered in this study, nine in all. Note that for the equal flow rate ratios of 1/10, 2/20, 3/30, the profiles overlap and are not distinguishable from one another. These profiles correspond to an exit concentration of 22.5 percent. Table 6 shows a comparison between the model and experimental results for the studied flow rates. The discrepancy between the exit concentration, X_{ss}

is primarily due to experimental measurement error, as well as the inlet concentration/flow rate drift from the nominal values.

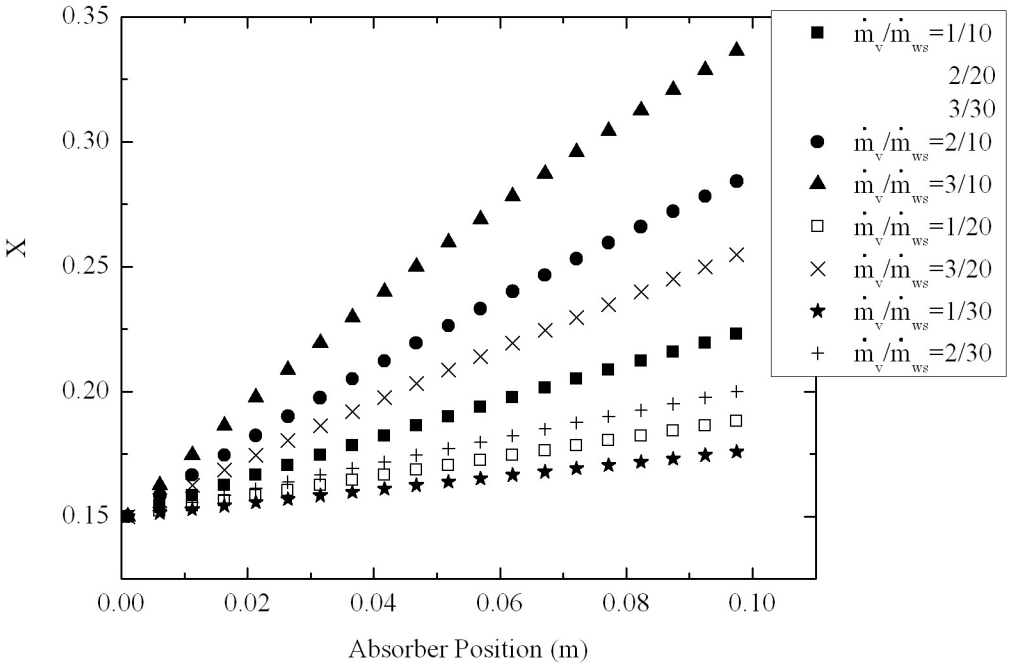

Fig. 25. Concentration profiles for all the flow rate ratios considered in this study

Table 6. Concentration comparison between model and experiment

$\dot{m}_v/\dot{m}_{ws}$	Experimental X_{ss}/X_{ws}	Model X_{ss} (X_{ws}=15%)
1/10	23.5/15.7	22.57
2/10	30.2/15.5	28.88
3/10	35.9/15.5	34.24
1/20	20.7/15.5	18.96
2/20	24.5/15.6	22.57
3/20	28.3/15.6	25.86
1/30	18.9/15.6	17.68
2/30	22.05/15.9	20.2
3/30	25.1/15.7	22.57

8 SIZING ESTIMATES

Given the maximum mass flow ratio for vapor and weak solution used in this study, namely, 3 g/min vapor and 10 g/min weak solution, scale up for any given vapor flow rate can be achieved. Typical vehicular and residential refrigeration cycles require 2.5kW and 10.6kW loads, respectively, at the evaporator (see Fig. 26). Based on these heat loads, the mass flow of vapor can be found from

$$\dot{m}_v = \frac{\dot{q}_{evap}}{h_{fg}} \tag{30}$$

The area of the scaled up absorber can be found from:

$$\frac{A_2}{A_1} = \frac{\dot{m}_{v,2}}{\dot{m}_{v,1}} \tag{31}$$

Where subscripts 1 and 2 represent the current absorber and the scaled-up absorber, respectively.

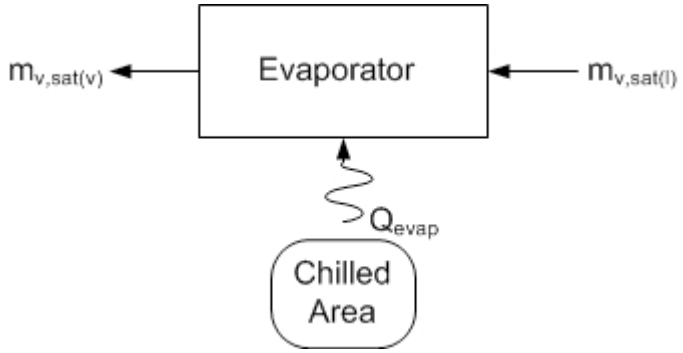

Fig. 26. Heat load at the evaporator

Assuming that the ammonia enters the evaporator as a saturated liquid and exits as a saturated vapor, the area can be determined from Eq. 31 given a system pressure and evaporator heat load. A system pressure of 5.5 bar at the evaporator

yields a 775 cm^2 and 3284 cm^2 absorber area for a vehicular and residential load, respectively. If the absorber was designed such that the cooling fluid flowed between two solution streams, compact absorbers could be realized. Given the type of arrangement shown in Fig. 27, the vehicular absorber dimensions could be 4 cm x 14 cm x 28 cm, and the residential absorber dimensions, 4 cm x 29 cm x 58 cm. A residential heat pump of roughly 1 m^3 could adequately hold the aforementioned absorber.

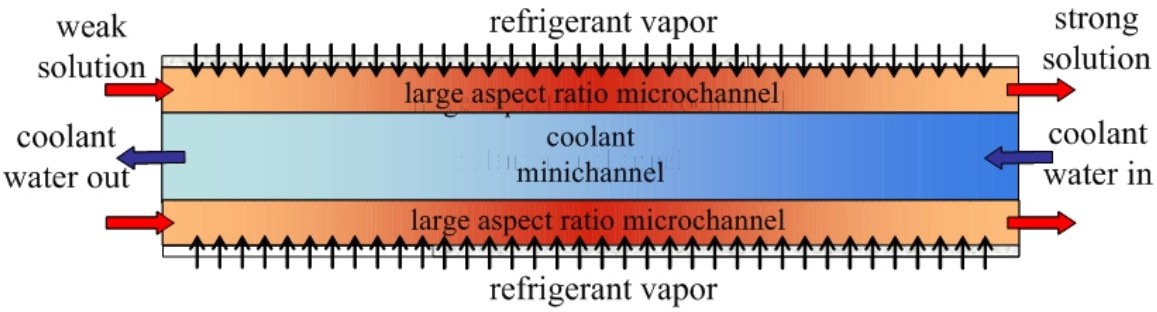

Fig. 27. Dual-sided bubble absorber

9 CONCLUSIONS AND RECCOMENDATIONS

Presented in this study was the investigation of the performance of a constrained microscale film ammonia-water bubble absorber under a variety of test conditions. Cooling water at a constant inlet temperature and mass flow rate flowed counter to the ammonia-water solution in a fixed-depth channel of 0.88 mm. Experimental variables included inlet concentrations of 0,5,10 and 15 percent, system pressures of 1, 2.5 and 4 bar, inlet weak solution mass flow rates of 10, 20 and 30 g/min, and ammonia vapor mass flow rates of 1, 2, and 3 g/min. Also, six different microchannel geometries were studied, three with smooth heat transfer surfaces and three with structured surfaces. The three smooth surfaces consisted of a 150 μm, 400 μm and 1500 μm deep solution side channel, while the structured surfaces consisted of a cross ribbed, angled cross ribbed, and streamwise finned geometry with nominal depths of 150 μm. Additionaly, a visualization study was performed for three different porous plates used to bubble ammonia vapor into the microchannel. A 0.5 μm pore size sintered stainless steel porous plate was used along with two different straight hole designs made from Peek® plastic. The porous plate achieved the largest net interfacial area of the bubbles for mass transfer, and as such, this plate was used for all experiments.

Measured global variables such as inlet and exit temperatures, pressures, and densities were used to characterize the absorber's heat and mass transfer performance for the various inlet concentrations, vapor/weak solution mass flow rates and microchannel geometries considered.

It was found that the inlet concentration has little to no effect on the overall heat transfer coefficient (U), however, increasing it results in an increase in the mass transfer coefficient (h_m). The 150 μm smooth microchannel exhibited it's highest U for low flow rate ratios of 1/20 and 1/30, but correspondingly, the lowest h_m existed for these flow cases. It was concluded that the best flow rate ratio was 3/10 due to both the enhanced heat and mass transfer performance.

Channel depth effects were scrutinized for the smooth microchannels for a system pressure of 4 bar and inlet concentration of 15 percent. The overall heat transfer coefficient dropped for increasing channel depth for the lowest flow ratio cases of 1/20 and 1/30, as would be expected for a single-phase flow. Higher flow rate ratios produced trends that showed a U increase from 150 μm to 400 μm, followed by a drop at 1500 μm, suggesting that there exists an optimum channel depth. The mass transfer coefficient was found to have the opposite trend of U for the three depths, and for a fixed h_m the corresponding U was highest for the 400 μm. Three competing effects were believed to govern the heat and mass transfer: (a) a reduction in the heat exchange area due to potential of vapor contact with the bottom microchannel wall, and (b) enhanced mixing in the local solution due to the injected vapor, and (c) reduced heat transport from the liquid-vapor interface to the heat exchange surface due to increased liquid layer thickness and the corresponding heat transfer resistance.

All six channel geometries were compared for a system pressure of 4 bar and inlet concentration of 15 percent. At a weak solution flow rate of 10 g/min, the 400 μm smooth channel showed an average U that was 270 percent higher than the 150 μm smooth channel. At the highest flow rate ratio, 3/10, the only microchannels that

achieved complete absorption as indicated by a single phase liquid exiting the absorber, were the smooth 150 μm and 400 μm microchannels. The U for the streamwise-finned microchannel was fairly large, 2700 (W/m^2-K) for a vapor flow rate of 1 g/min but dropped considerably to 900 (W/m^2-K) for higher vapor flow rates.

Increasing the weak solution flow rate to 30 g/min showed different trends from the 10 g/min cases. The largest U was exhibited by the 150 μm smooth channel for a vapor flow rate of 1 g/min, followed by the streamwise-finned channel. As the vapor flow rate was increased, U decreased for the 150 μm smooth channel and also the three structured channels, but the 400 μm channel showed an increase. These channels approached limits and it was conjectured that the high limit for the 400 μm versus the low limit for the 150 μm is the result of heat transfer limiting on the coolant side and solution side, respectively. All geometries studied showed a linear increase in h_m for a corresponding increase in vapor flow rate. Through all of the experimental studies, it was shown that the 400 μm smooth channel was the best performer in terms of heat and mass transfer.

A numerical model was developed that predicts absorber temperature and concentration profiles along the length of a microchannel bubble absorber. The model showed expected profiles for various weak solution and vapor flow rates, however, these were found under the assumption of instantaneous absorption. A model was proposed that accounts for mass transfer rates and bubble size reduction throughout the solution space. It is believed this model will play a role as a design tool for determining appropriate microchannel sizes that yield completed absorption.

Finally, absorber sizing estimates were made for the highest mass flow ratio case, 3/10. Using this approach, the absorber can be scaled up for various required evaporator loads dependent upon the application (residential or vehicular units). Absorber dimensions for a vehicle were estimated at 4 cm x 14 cm x 28 cm, and the residential absorber dimensions, 4 cm x 29 cm x 58 cm.

Continuing research on a microscale bubble absorber is required to fully understand the local processes governing the heat and mass transfer. Particle Image Velocimetry, PIV , in conjunction with local temperature measurements via thermal imaging using an infrared camera would prove beneficial in understanding local phenomena. Also of import might be to expose the absorber to some form of actual cycle operating conditions, dependent of course upon the refrigeration application. This could be followed up with an integration of the bubble absorber into a closed loop absorption refrigeration cycle.

REFERENCES

[1] Foley, G., DeVault, R., Sweetser, R., 2000, "The Future of Absorption Technology in America," Proceedings of the 2000 Advanced Building Systems Conference. Oak Ridge National Laboratory.

[2] Garimella, S., 2005, "Binary-Fluid Heat and Mass Transfer In Microchannel Geometries For Minuaturized Thermally Activated Absorption Heat Pumps," *Microscale Heat Transfer*, Kakac et al. eds., Springer, Netherlands, pp. 339-368.

[3] Meachum, M.J., and Garimella, S., 2004, "Ammonia-Water Absorption Heat and Mass Transfer in Microchannel Absorbers with Visual Confirmation," *ASHRAE Transactions: Symposia,* AN-04-7-4, pp. 525-532.

[4] Goel, N., and Goswami, D. Y., 2005, "A Compact Falling Film Absorber," *Journal of Heat Transfer*. ASME, Vol. 127, pp. 957-965.

[5] Goel, N., and Goswami, D. Y., 2007, "Experimental Verification of a New Heat and Mass Transfer Enhancement Concept in a Microchannel Falling Film Absorber," Journal of Heat Transfer, Vol. 129, pp. 154-161.

[6] Staicovici, M.D., 2000, "A phenomenological theory of polycomponent interactions in non-ideal mixtures. Application to NH_3/H_2O and other working pairs," *International Journal of Refrigeration*, Vol. 23, pp. 153-167.

[7] Helbing, U., Würfel, R., and Fratzscher, W., 2000, "Comparative Investigations of Non-adiabatic Absorption in Film Flow and Bubble Flow," *Chemical Engineering Technology*, Vol. 23, pp. 1081-1085.

[8] Kang, Y.T., Atsushi, A., and Kashiwagi, T., 2000, "Analytical Investigation of two different absorption modes: falling film and bubble types," *International Journal of Refrigeration*, Vol. 23, pp. 430-443.

[9] Lee, K.B., Chun, B.H., Lee, J.C., Hyun, J.C., and Kim, S.H., 2002, "Comparison of Heat and Mass Transfer in Falling Film and Bubble Absorbers of Ammonia-Water," *Experimental Heat Transfer*, Vol. 15, pp. 191-205.

[10] Lee, K.B., Chun, B.H., Lee, J.C., Lee, C.H., and Kim, S.H., 2002, "Experimental analysis of bubble mode in a plate-type absorber," *Chemical Engineering Science*, Vol. 57, pp.1923-1929.

[11] Lee, J.C., Lee, K.B., Chun, B., Chan, H., Ha, J., and Kim, S.H. 2003, "A study on numerical simulations and experiments for mass transfer in bubble mode absorber of ammonia and water," *International Journal of Refrigeration*, Vol. 26, pp. 551-558.

[12] Herold, K.E., Radermacher, R., and Klein, S.A. 1996, *Absorption Chillers and Heat Pumps* CRC Press, Boca Raton, FL.

[13] Huang, C.H., 2005, "Theoretical model of absorption of ammonia by fine water spray," *Environmental Engineering Science.* Vol 22: 4, pp. 535-541.

[14] Summerer, F. Ziegler, F., Riesch, P., and Alefeld, G., 1996, "Hydroxide Absorption Heat Pumps with Spray Absorber," Vol 102:11, pp. 1010-1016.

[15] Venegas, M., Arzoz, D., and Rodriguez, P., 2003, "Heat and Mass Transfer in $LiNO_3$-NH_3 Spray Absorption System," *Int. Comm. Heat and Mass Transfer*. Vol. 30:6, pp. 805-815.

[16] Jenks, J., and Narayanan, V., 2006, "An Experimental Study of Ammonia-Water Bubble Absorption in a Large Aspect Ratio Microchannel," Paper # IMECE2006-14036, Proceedings of the 2006 IMECE, Chicago, IL.

[17] Ibrahim, O.M., Klein, S.A., 1993, "Thermodynamic Properties of Ammonia-Water Mixtures," *ASHRAE Trans.: Symposia,* Vol. 21, 2, 1495.

[18] Narayanan, V., Kanury, A. M., and Jenks, J., 2007, "Modified Heat Exchanger Analysis Accounting for Heat Generation," Paper HT2007-33444, Proceedings of the 2007 ASME-JSME Thermal Engineering Summer Heat Transfer Conference, Vancouver, British Columbia, Canada, July 8-12, 2007.

[19] Figliola, R. S., and Beasley, D. E., 2000, *Theory and Design for Mechanical Measurements*, Third edition, John Wiley & sons, Hoboken, NJ.

[20] Incropera, F.D., and DeWitt, D.P., 2002, *Fundamentals of Heat and Mass Transfer*, Fifth Edition, John Wiley & sons, Hoboken, NJ.

[21] Daniels, B., Liburdy, J. (Adivsor). Property estimation Matlab code using empirical correlations from [17] provided courtesy of G. Mouchka.

[22] Treybal, R.E., 1980, *Mass Transfer Operations*, Third Edition, McGraw Hill, New York, NY.

APPENDICES

Appendix 1 Standard Operating Procedure

SOP: Ammonia-Water Absorption Experiment
Updated: 7/15/06

Startup:

1) **Ensure all primary valves are closed**
   - A) **Close 3-way valve before Sierra Gas Flow meter/controller (GFM) by positioning handle perpendicular to flow**
   - B) **Close 2-way after GFM in similar manner**
   - C) **Close need valve at test section inlet by turning clockwise**
   - D) **Close 2-way at Corriolis Flow Meter (CFM) exit**

2) **Pressurize system/Open loop To Sump**
   - A) **Pressurize Inlet/Outlet Tanks using Air press. Reg.**
   - B) **Open valve to sump air inlet to pressurize.**
   - C) **Ensure the 3-way valves next to sump are pointed towards eachother (allows for flow from the inlet tank to the Test section and then to the sump)**

3) **Purge System with Nitrogen (*Optional*)**
   - A) **Turn on nitrogen supply tank and set pressure regulator to 20 psi**
   - B) **Turn GFM 3-way valve on for Nitrogen by turning black handle so that it points towards incoming Nitrogen**
   - C) **Ensure GFM is set two purge valve mode (password is 0000)**
   - D) **Turn on 2-way valve at GFM exit—Purge for 30 seconds**
   - E) **Turn off 2-way followed by 3-way—Purge completed—close Nitrogen supply tank.**

4) **Supply Anhydrous Ammonia**
   - A) **Supply pressure from Anhydrous Ammonia tank**
     NOTE: This pressure must be set to a slightly higher pressure then operating system pressure to ensure no backflow to GFM.
   - B) **Turn GFM 3-way towards the direction of Ammonia gas flow**
   - C) **Ensure GFM is set to automatic valve mode at desired mass flow set point. DO NOT TURN ON GFM EXIT 2-WAY AT THIS POINT.**

5) **Supply Weak Solution**
   - A) **Turn on solonoid valve**
   - B) **Turn on Micro-Pump to desired power (10-40%)**
   - C) **Open 2-way valve at CFM exit**
   - D) **Supply Ammonia Gas to test section, open 2-way valve at GFM exit.**

E) Open needle valve at Test section inlet until desired CFM mass flow is achieved—system is now in operation.
F) Upon reaching steady state, turn off solonoid valve (supplies solution to the sump for sampling)

6) Check Sump solution (Strong solution) Density after primary data collection.
A) Turn off pump, switch gas to Nitrogen
B) Turn top sump valve 180^{o} (pointing up)
C) Turn solonoid valve on
D) Turn pump on
E) Record density of CFM readout upon reaching steady value, pump all solution
Out to outlet tank.

7) Empty Tank for each new inlet concentration
A) Open PVC two way valves and allow pressure driven discharge.

Shutdown:
1) Close test section inlet needle valve
2) Close GFM exit two way valve
3) Turn off pump power supply
4) Set GFM to "Valve Closed" operation
5) Close CFM 2-way
6) Close GFM 3-way
7) Close NH3 supply tank

Appendix 2 Heat Load and Concentration Calc. Comparison

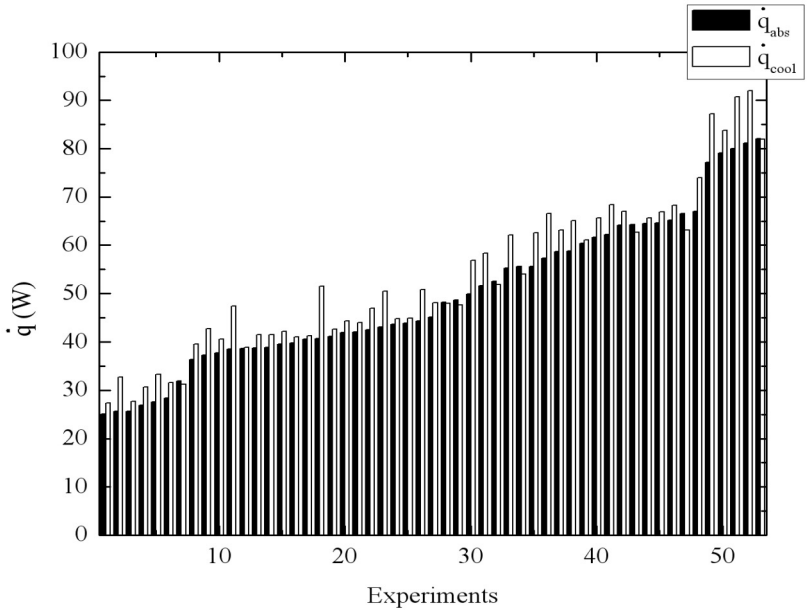

Fig. A1 . Comparison of heat transferred from the absorber with heat transferred to the coolant for all 400 μm, 1500 μm, CR, ACR, and SF channels

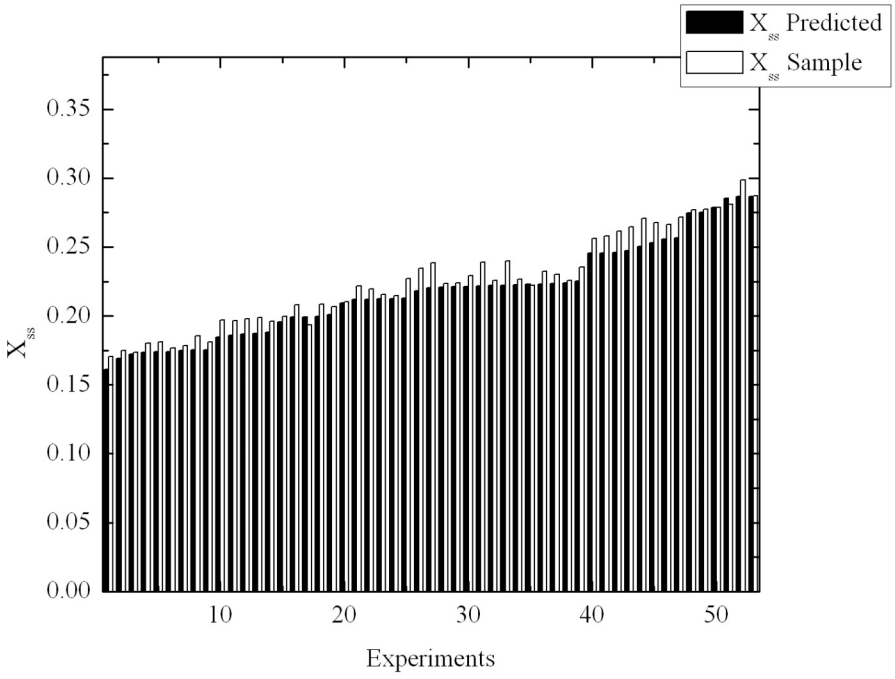

Fig. A2. Comparison of exit concentration found from the sample and predicted for all experiments used for 400 μm, 1500 μm, CR, ACR, and SF channels

Appendix 3 Pressure Differential Across Bubble Plate

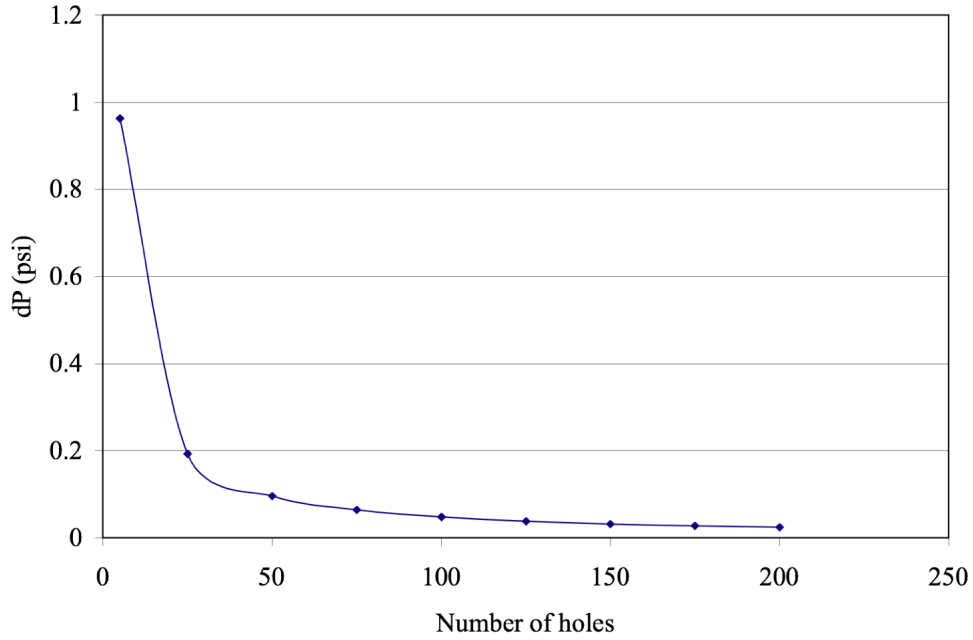

Fig. A3. Pressure drop across the bubble plate versus number of drilled holes for 150 µm diameter smooth holes using Bernoulli's equation with the added friction factor correction term

Appendix 4 m_{ws}=20 g/min graphs

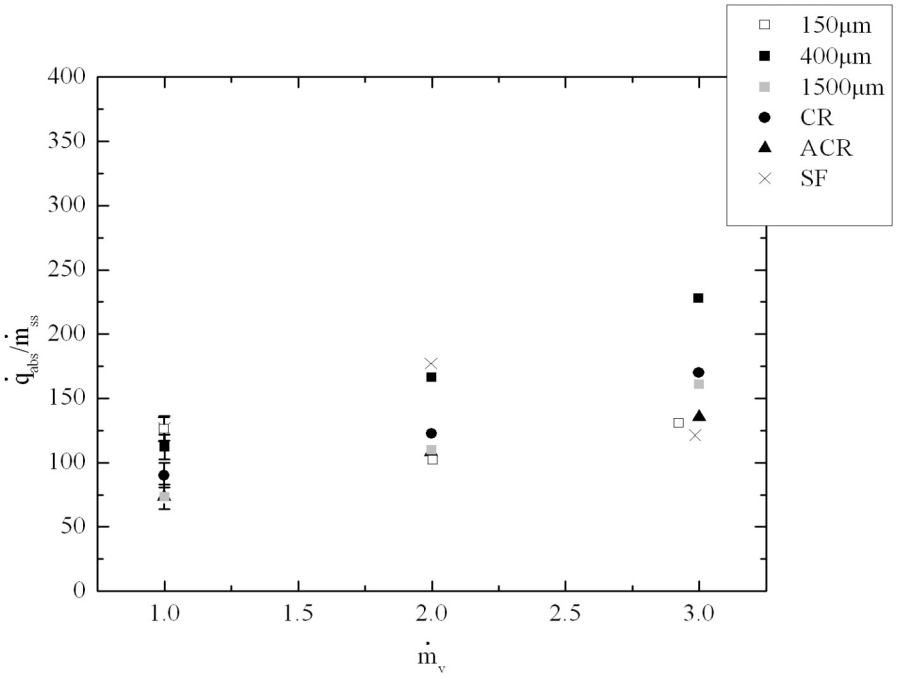

Fig. A4. Heat load for P=4 bar, X_{ws}= 15 percent, m_{ws}=20 g/min

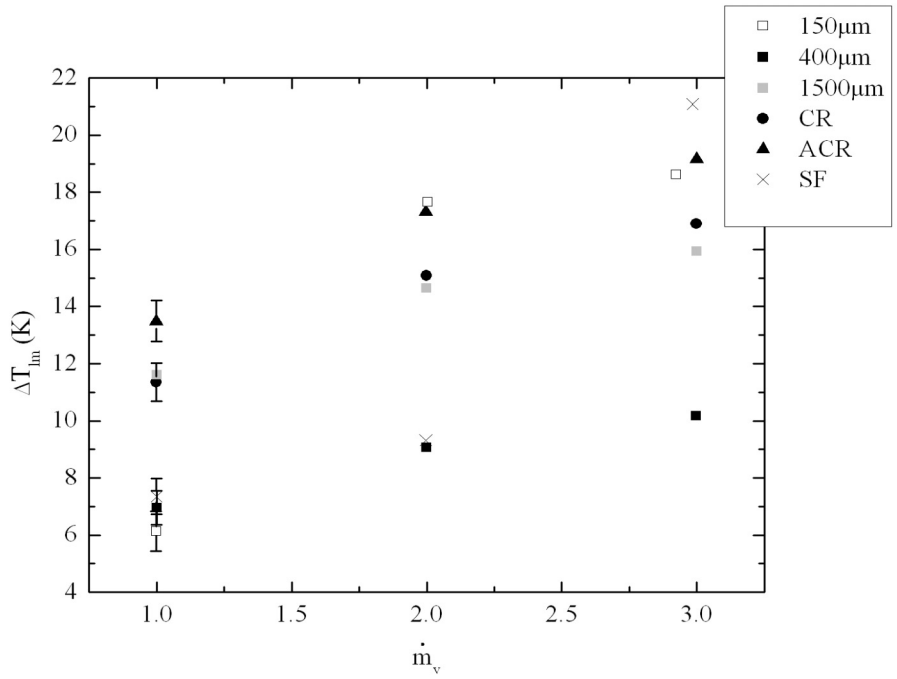

Fig. A5. ΔT_{lm} for P=4 bar, X_{ws}= 15 percent, m_{ws}=20 g/min

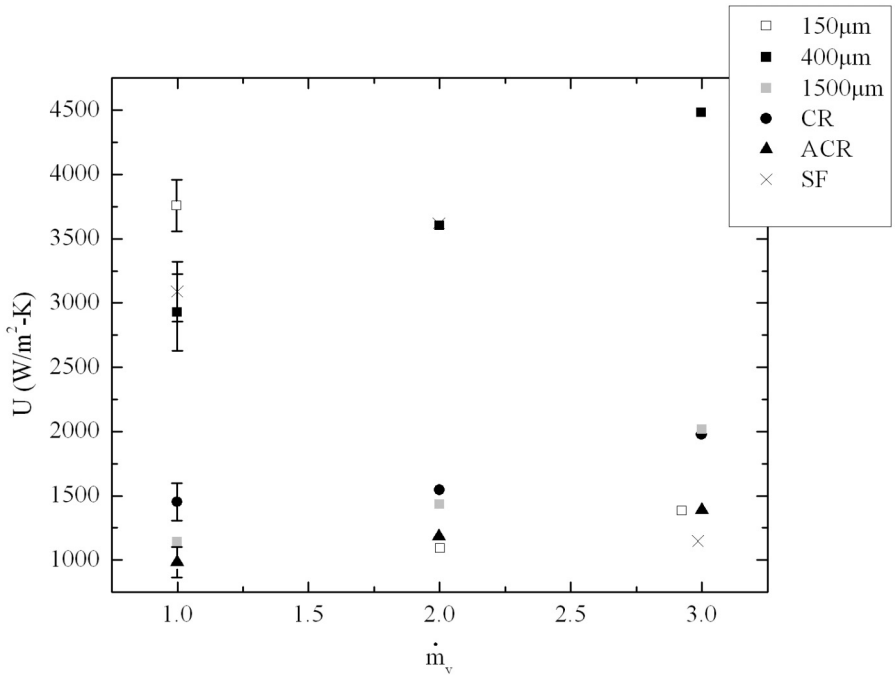

Fig. A6. Overall Heat Transfer Coeff. for P=4 bar, X_{ws}= 15 percent, m_{ws}=20 g/min

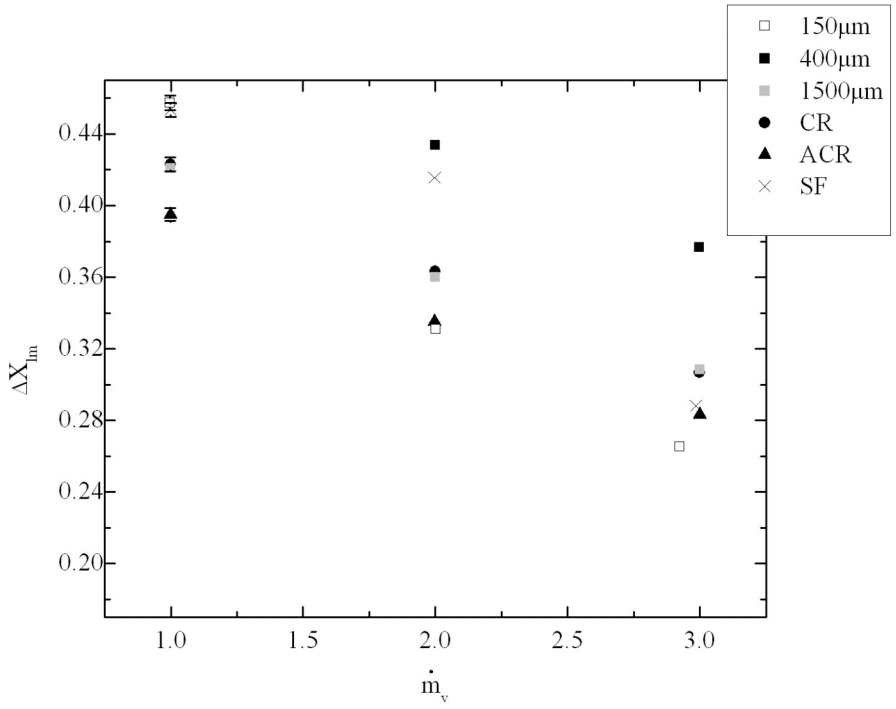

Fig. A7. ΔX_{lm} for P=4 bar, X_{ws}= 15 percent, m_{ws}=20 g/min

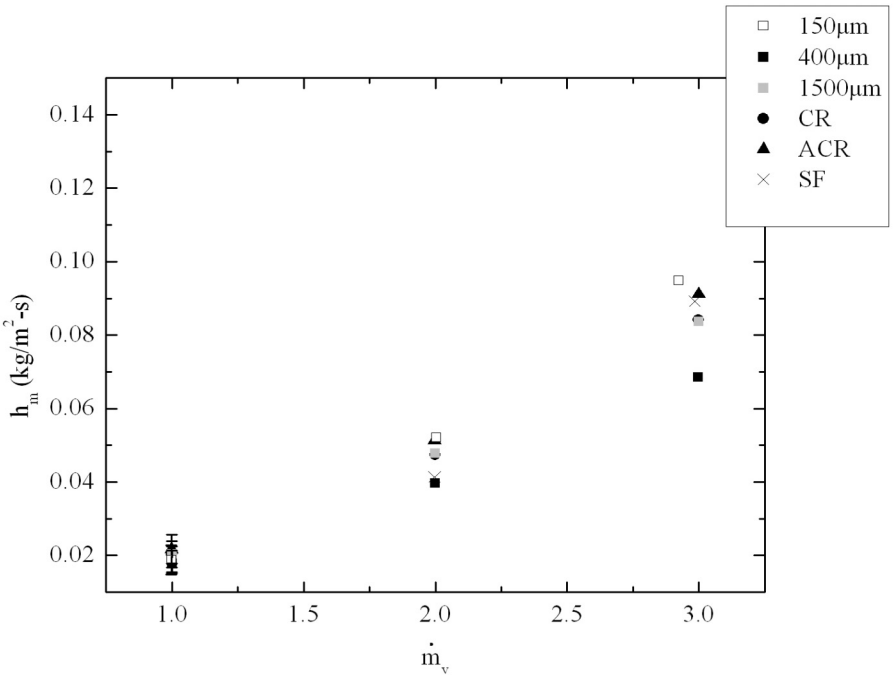

Fig. A8. Mass transfer coefficient for P=4 bar, X_{ws}= 15 percent, m_{ws}=20 g/min

Appendix 5 Uncertainty Analysis

Uncertainty analysis was performed for the experimental data using either the Kline-McClintock method or sequential perturbation. The sequential perturbation method was used for calculated values that had derivatives which were cumbersome to determine. In general, the uncertainty for any given measurement (temperature, pressure, mass flow rate) was found from

$$U_{tot} = \sqrt{(\hat{a})^2 + (t_{v,95}P)^2} \tag{A1}$$

where, β is the bias error defined by a combination of precision error for data taken for calibration and the bias error associated with the device used to calibrate the particular instrument used in actual data collection. Additionally, curvefit errors for each calibration were taken into account. Using the aforementioned values, the total bias error, also called the calibration error associated with the instrument could be found from

$$U_{calib} = \sqrt{(\hat{a}_{calibrator})^2 + (t_{v,95}P_{calib})^2 + (U_{curvefit})^2} \tag{A2}$$

The precision errors are based on the t-statistic curve for a 95 percent confidence interval and P is given by

$$P = \frac{Std}{N^{1/2}} \tag{A3}$$

where Std is the standard deviation of the data, and N is the total number of data points taken.

As previously mentioned, the Kline-McClintock method was used for many of the calculated quantities and was found from taking the partial of all variables in a given equation. Given a calculated value, say Y, where

$$Y = f(x_1, x_{21}, x_3 \ldots\ldots x_n) \tag{A4}$$

Given the uncertainties previously found for each variable in Y, the total uncertainty in Y can be found from

$$U_Y = \pm\sqrt{\sum_{i=1}^{n}\left(\frac{\partial Y}{\partial x_i} u_{x_i}\right)^2} \tag{A5}$$

Uncertainty in values such as ΔT_{lm}, and ΔX_{lm} were found via the method of sequential perturbation.

Calibration for pressure and temperature was performed using a NIST traceable reference gauge. The mass flow rate calibration of the coriolis flow meter was performed using a computer automated cache and weigh method. Using a solenoid valve, the automate process provided for a precision calibration as indicated by Fig. A9.

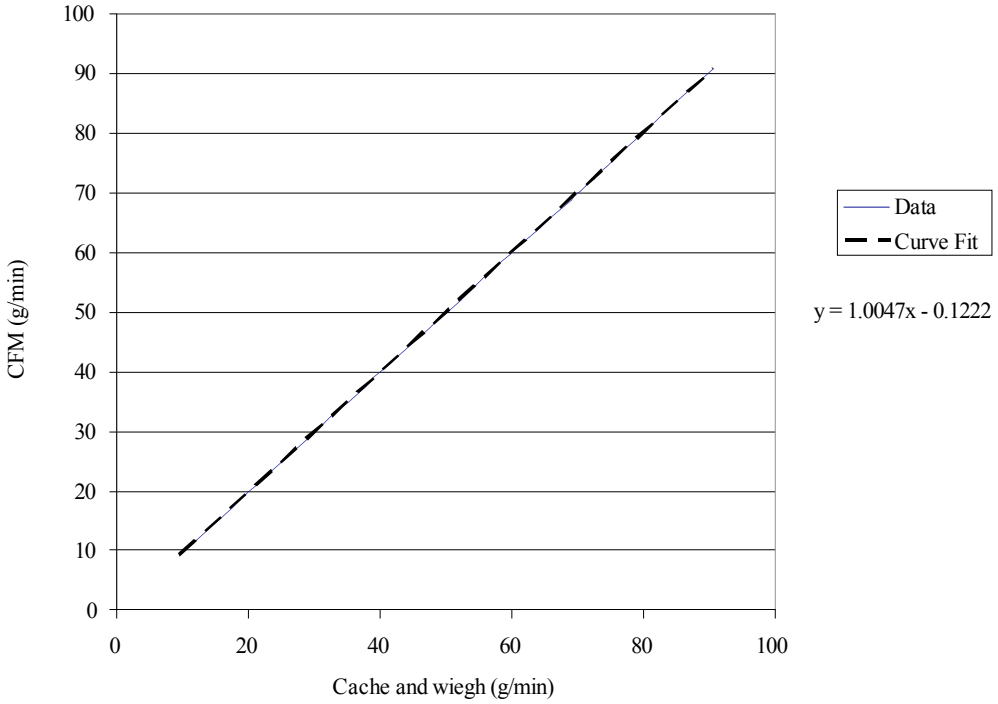

Fig. A9. Calibration curve for the coriolis flow meter (CFM) using a cache and weigh method.

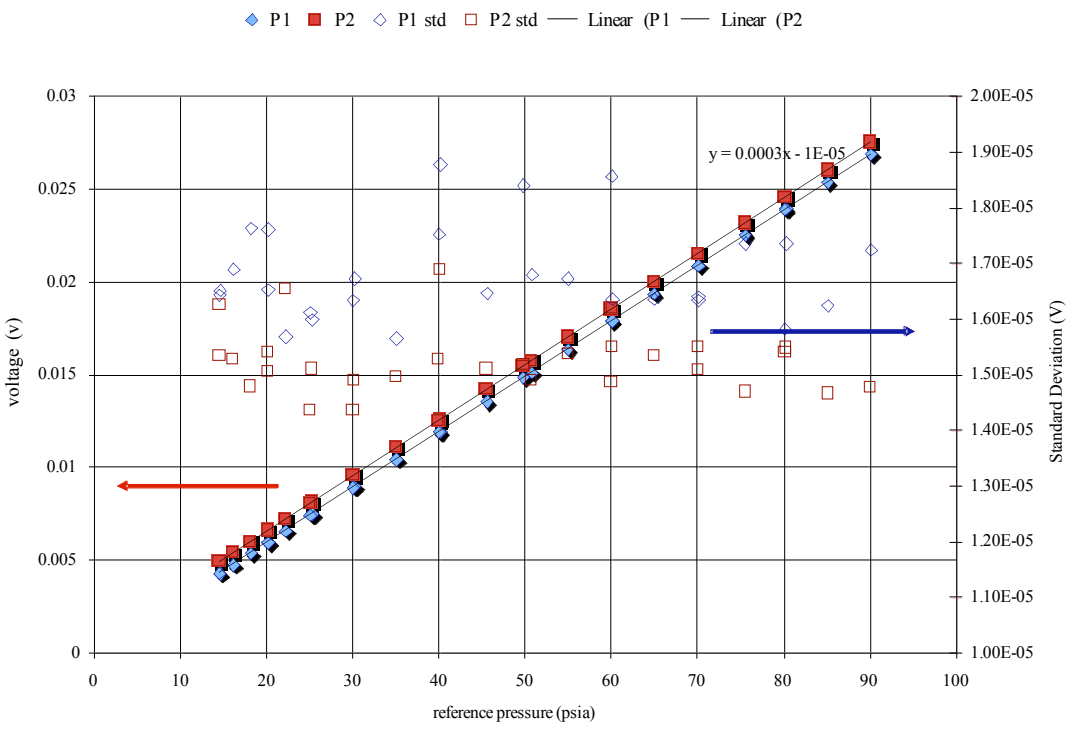

(A10a)

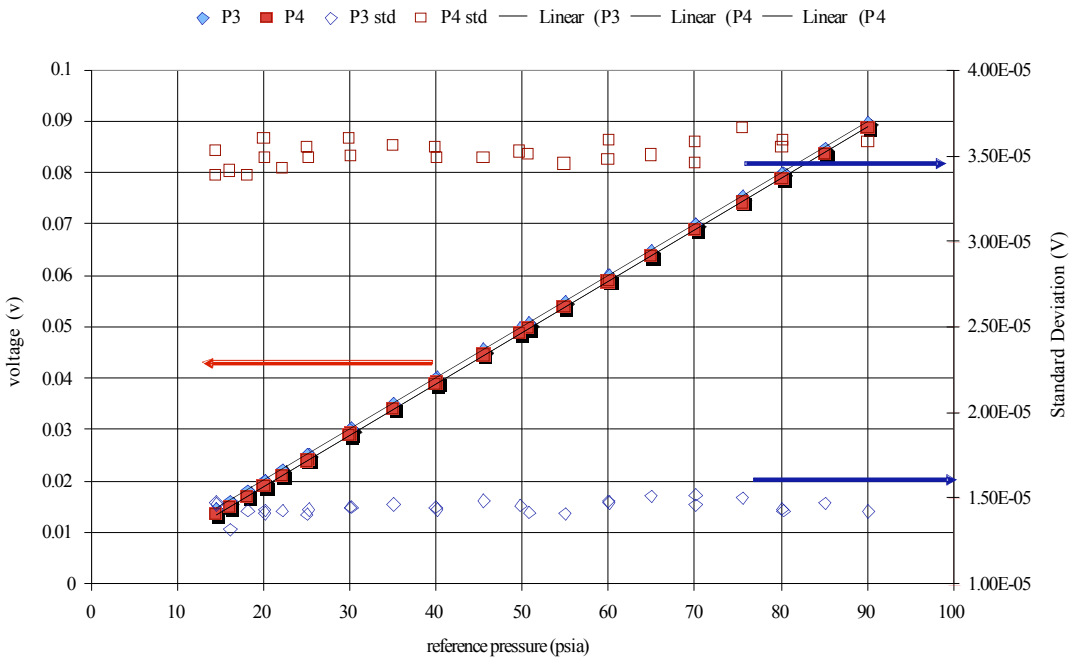

(A10b)

Fig. A10. Pressure calibration plot of measured voltage versus reference gauge pressure for (a) P1 (solution inlet) and P2 (solution exit) and (b) P3 (Vapor) and P4 (CFM) including standard deviation

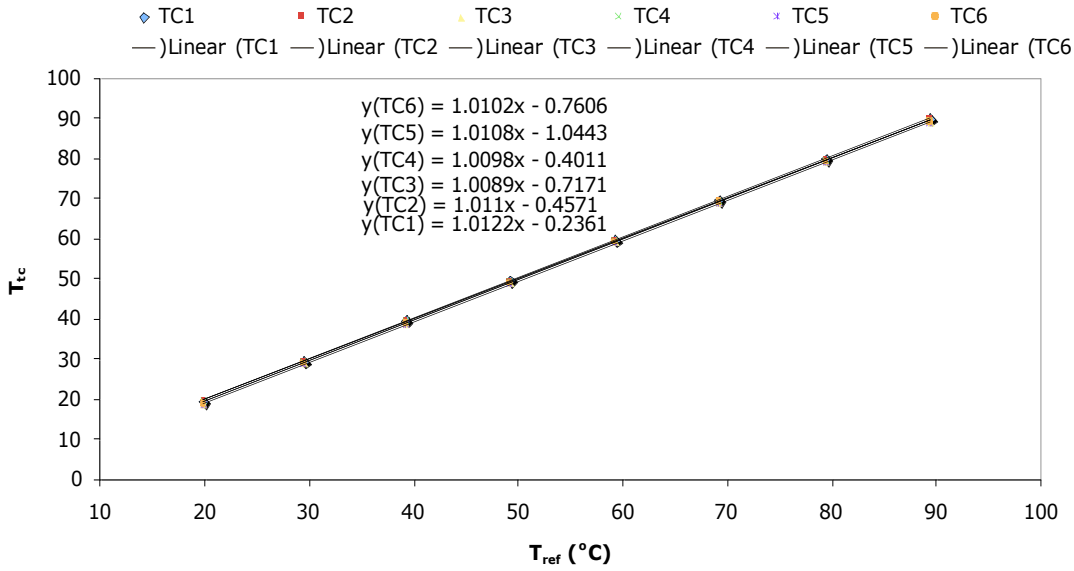

Fig. A11. Temperature calibration plot of thermocouple (TC) values versus reference gauge values

Respective average uncertainty values for measured data are shown in table A1. Average uncertainty values for data presented in the "Results and Discussion" chapter are shown in table A2, along with the method used to find the uncertainty. The largest uncertainties were exhibited in the final calculation namely, h_m and U, due to the propagation of all of the preceding errors. The mass transfer coefficient, h_m, had an average uncertainty of 7.7 percent, while the overall heat transfer coefficient, U, had and average uncertainty of 9.9 percent.

Table A1. Average uncertainty values for measured variables

Instrument	$\overline{U}_{calibration}$	$\overline{U}_{precision}$	$\overline{U}_{total}$
P1 (P_{ws}) (psia)	0.055	0.007814	0.055662
P2 (P_{ss}) (psia)	0.057	0.006565	0.057679
P3 (P_{cfm}) (psia)	0.080	0.015325	0.083297
P4 (P_{vap}) (psia)	0.081	0.004429	0.081614
TC0 (T_{vap}) (^oC)	0.370	0.007979	0.370126
TC1 (T_{ws}) (^oC)	0.351	0.01976	0.352094
TC2 (T_{ss}) (^oC)	0.345	0.026666	0.346472
TC3 (T_{co}) (^oC)	0.361	0.003901	0.361025
TC4 (T_{ci}) (^oC)	0.339	0.004652	0.339034
TC5 ($T_{exit\text{-}tank}$) (^oC)	0.346	0.015285	-
TC6 (ambient) (^oC)	-	0.004907	-
TC7 (ambient) (^oC)	-	0.005056	-
TC8 (T_{cfm}) (^oC)	0.867	0.008109	0.867213
$\dot{m}_{cfm}$ ($\dot{m}_{ws}$) **(g/min)**	0.121	0.006901194	0.12125499
$\dot{m}_{gfm}$ ($\dot{m}_{vap}$) **(g/min)**	7.07 percent of measured value (manuf. error)	0.001518	0.134018231
ρ (density) (kg/m^3)			Manuf. Error: ±0.5 kg/m^3

Table A2. Average uncertainty values for calculated quantities and the method used

Value	Uncertainty Method	$\overline{U}_{total}$
$\dot{m}_{ss}$ **(g/min)**	Kline-McClintock (KM)	0.184688
$\mathbf{X_{ws}}$	Sequential Perturbation (SP)	0.001416
$\mathbf{X_{ss}}$	SP	0.001748
$\mathbf{h_{vap}}$ **(kJ/kg)**	KM in EES	0.961823377
$\mathbf{h_{ws}}$ **(kJ/kg)**	KM in EES	3.743324675
$\mathbf{h_{ss}}$ **(kJ/kg)**	KM in EES	1.816233766
$\dot{q}_{abs}$ **(W)**	KM	3.426005
$\mathbf{\Delta T_{lm}}$ **(K)**	SP	0.694725
U $\mathbf{(W/m^2\text{-}K)}$	KM	173.7931
$\mathbf{\Delta X_{lm}}$	SP	0.004599
$\mathbf{h_m}$ $\mathbf{(kg/m^2\text{-}s)}$	KM	0.052566
$\mathbf{A_{hx}}$ $\mathbf{(m^2)}$	KM	2.63E-06

Appendix 6 Proposed Model with Mass Transfer

The model described previously outlines a numerical model that predicts temperature and concentration profiles assuming total absorption of ammonia vapor within each control volume. Missing in the current model is the actual mass transfer rate of ammonia within each control volume. This is a vital piece of information that ultimately leads to the required geometry of the microchannel that allows for complete absorption within the absorber. The following discussion seeks to incorporate this mass transfer model.

Shown in Fig. A12 is a series of control volumes for the solution side of the absorber. Realistically, absorption does not occur instantaneously when the ammonia flows into the microchannel. On the contrary, bubbles are injected at a fixed rate at control volume i and then flow downstream, slowly shrinking as they absorb into solution for each incremental control volume. Also, within each incremental control volume, new bubbles are introduced at the same constant rate and size as in the first control volume. Therefore, various bubble sizes can exist in a control volume and thus, different bubble to liquid mass transfer rates can occur along the channel.

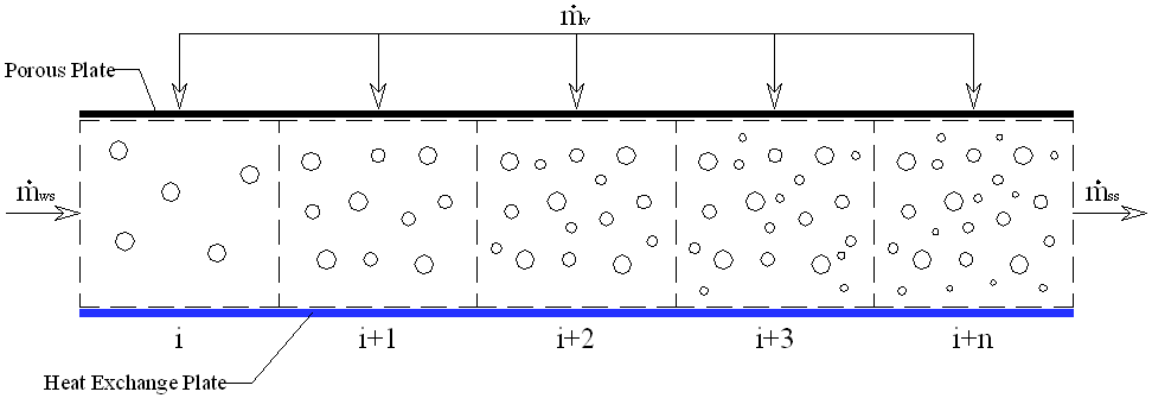

Fig. A12. Control volumes showing bubble injection and absorption along the microchannel

Equations Governing Mass Transfer

In the forgoing proposed model, which is inclusive of local mass transfer rates, the following assumptions are made:

1) Mass transfer is uniform at the bubble interface
2) The ammonia bubbles are perfect spheres
3) Ammonia is an ideal gas
4) Bubble injection occurs uniformly over porous plate

The mass absorption rate for a fixed set of equally sized bubbles can be determined from

$$\dot{dm}_a = n_b K_l A_b \tilde{n}_l (x_i - x_l) \tag{A6}$$

where the area of a bubble is

$$A_b = \partial d_b^{\,2} \tag{A7}$$

and the interface concentration can be approximated as

$$x_i \approx f(T_{lb}, P) \tag{A8}$$

using correlations from Ibrahim and Klein [17].

The mass transfer coefficient, K_l is related to the Sherwood number, much like the heat transfer coefficient is to the Nusselt number,

$$K_l = \frac{Sh_l D_l}{d_b} \tag{A9}$$

The Sherwood number can be found from a correlation given by Treybol for bubble vapor absorption of highly soluble gases [22] as

$$Sh_l = 2 + 0.0187\,\mathrm{Re}_b^{\,0.779}\, Sc^{0.546} (d_b g^{0.333} D_l^{\,-0.666})^{0.116} \tag{A10}$$

where the Schmidt number is a ratio of the momentum to mass diffusivities

$$\mathrm{Sc} = \frac{v}{D} \tag{A11}$$

and the Reynolds number for the bubble is defined using the slip velocity as

$$\mathrm{Re}_b = \frac{\rho_v v_{slip} d_b}{\mu_b} \tag{A12}$$

J. Lee*, et. al.* [11] found that for an orifice Reynolds number $\mathrm{Re}_o < 2100$ the initial bubble diameter for an injected bubble is given by

$$\mathrm{d_b} = 0.0287 \mathrm{d_o}^{1/2}\, \mathrm{Re_o}^{1/3} \tag{A13}$$

where the orifice Re is given by

$$\mathrm{Re_o} = \frac{\tilde{n}_v \mathrm{v_o d_o}}{\grave{\imath}_o} \tag{A14}$$

The number of bubbles entering through the porous plate can be approximated as follows: The number of bubbles entering for some time period is

$$\frac{\mathrm{n_b}}{\Delta \mathrm{t}} = \frac{\frac{\mathrm{V_{tot}}}{\Delta \mathrm{t}}}{\mathrm{V_b}} \tag{A15}$$

where V_{tot} is the total volume of vapor injected into a control volume for a given time period found from the liquid residence time

(A16)

and also noting that

(A17)

and

$$V_b = \frac{\partial d_b^{\,3}}{6} \tag{A18}$$

Therefore, using Eqs. A16-A17 and inserting into to Eq. A15 results in

$$n_b = \frac{\dot{V}_{vap}\,dt}{V_b} = \frac{\dot{V}_{vap}\,dx}{V_b u_l} \tag{A19}$$

where the volumetric flow rate can be found from

$$\dot{V}_{vap} = \frac{d\dot{m}_v}{\tilde{n}_v} \tag{A20}$$

and

$$d\dot{m}_v = \frac{\dot{m}_v}{N} \tag{A21}$$

The bulk vapor concentration is determined from the amount of ammonia that is absorbed and is given by

$$x_{lb} = \frac{d\dot{m}_a + \dot{m}_{ws} x_{ws}}{\dot{m}_{ss}} \tag{A22}$$

The density of the liquid can be found similarly to the concentration from the Ibrahim and Klien [17] ammonia water property estimation previously mentioned

$$\tilde{n}_l = f(x_{lb}, T_{lb}, P) \tag{A23}$$

The liquid velocity is found from

$$u_l = \frac{\dot{m}_{ss}}{\tilde{n}_l A_c} \tag{A24}$$

In order to determine the temperature distribution along the absorber, the same equations (Eqs 22-27) from section 7.3 describing the energy transfer can be used.

The above equations lay the foundation for bubbles that are initially injected through the porous plate into a control volume, however, some attention should be given to the control volumes that follow the first (downstream control volumes). Recall that, aside from the first control volume, ammonia bubbles that are not completely absorbed and are of various sizes flow from one control volume to the next. The reduction of their area, along with the changing concentration and temperature must be taken into account. Given a fixed size of a group of bubbles flowing from the previous control volume (pcv), the absorption rate of these bubbles in the current control volume is given by

$$d\dot{m}_{a,pcv} = n_b K_l A_{b(i+1)} \rho_l (x_i - x_l) \tag{A25}$$

Note again that their may be several different size groups, and thus, several different absorption rates occurring. These must be tracked through the use of a recursion scheme.

In order to determine $A_{b(i+1)}$ and account for reduction of surface area with absorption, the diameter of the bubble can be found from

$$d_b(i+1) = \left(\frac{6(V_b(i) - dV_b)}{\partial} \right)^{1/3} \tag{A26}$$

The volume of the ammonia gas absorbed is found through the equation of state

$$dV_b = \frac{(d\dot{m}_a \frac{\Delta x}{u_{l(i)}}) R T_m}{P_v} \tag{A27}$$

Finally, the total mass absorption rate is given by the absorption rate from the new bubbles injected from the porous plate and the bubbles from the previous control volume

$$d\dot{m}_a(i+1)=d\dot{m}_{a,inj} + d\dot{m}_{a,pcv} \quad \text{(A28)}$$

A flow chart showing the structure of the algorithm is given in Fig. A13. The initial input includes the inlet temperatures, inlet mass flow rates, inlet concentration and system pressure. Additionally, the outlet temperature of the counter flowing cooling water must be guessed such that the energy transfer between the hot and cold sides can be determined. The mass absorbed, bulk liquid concentration, liquid density and velocity are first calculated using Eqs. A6-A24. The cooling water temperature and solution enthalpy are then computed. The algorithm must then incorporate a recursion scheme to account for the various bubble sizes that will exist in the following control volumes. The program then loops through the entire length of the solution space (length of the absorber). At the outlet of the solution side, which is also the inlet of the coolant side, the temperature of the coolant found from the model is compared with that which is known. If the two are within some specified convergence criterion the program terminates, but otherwise, adjusts the coolant outlet temperature and re-iterates starting from the beginning.

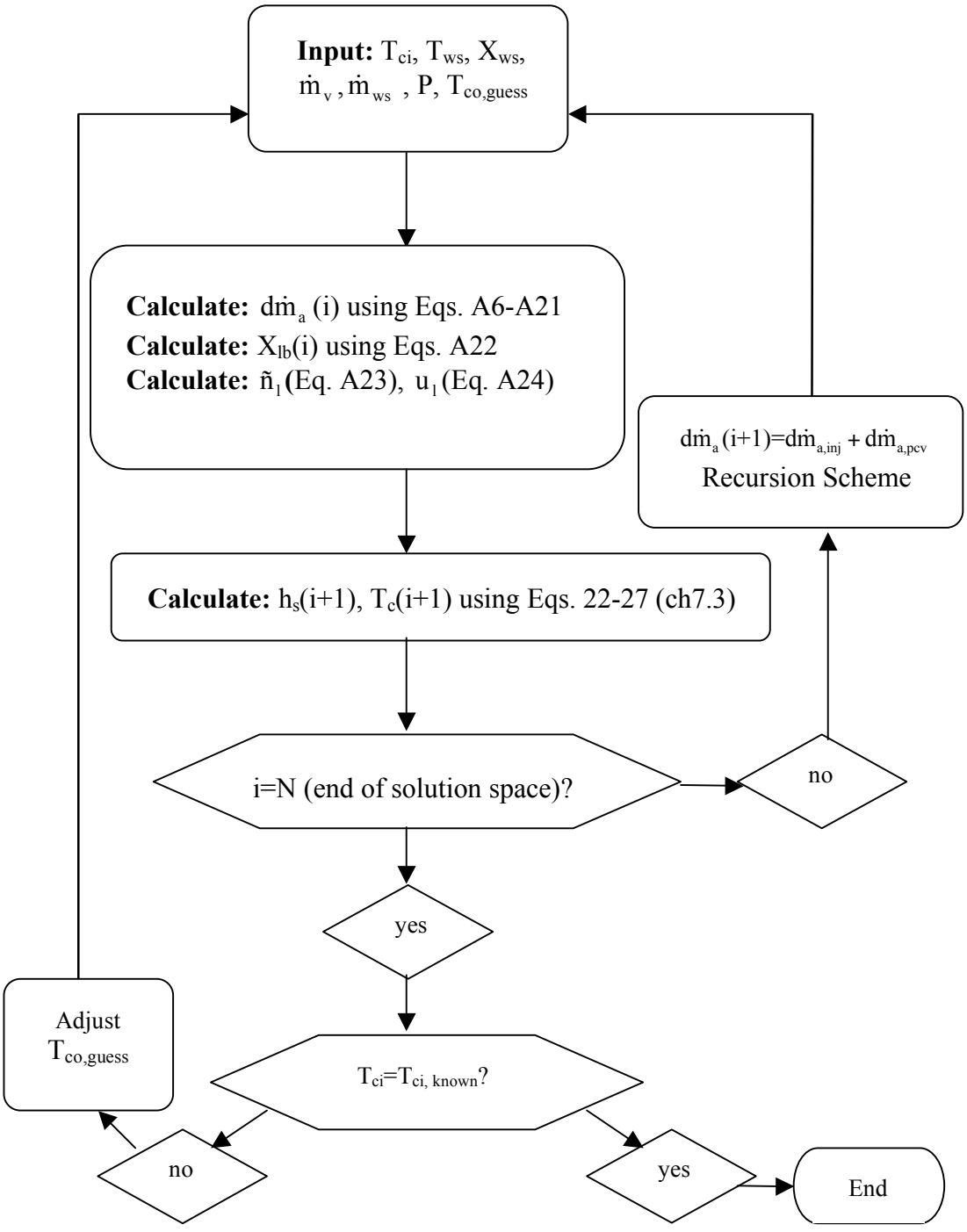

Fig. A13. Flow chart of proposed model inclusive of mass transfer

Appendix 7 Matlab® Predictive Numerical Model

PART I:

```
clear
%This code contains required input values and solves the continutiy
%equation along with determing the concentration of ammonia as it
changes
%with influx of ammonia gas, required properties are stored in single
%column matrices Jenks 3.1.07

P=4;     %System pressure
Tsi=295.7; %Fixed inlet Temperature of solution (hot)
Tso=310; %Exit temp of solution, not actual, just used to get
estimate of thermo-props.
Tci=283.6; %Fixed inlet temp of counterflowing coolant water (k)
Tco=288; %Guessed value of coolant outlet for estimating thermo props
Tv=295.6;%Temperature of Vapor (k)
mvg=2;% gas flow (g/min)
mv=(mvg/60)/1000;  %vapor flowrate (kg/s)
W=1.905/100;  %width of MC (m)
L=10.16/100; %length of mc (m)
depth=150E-6;  %depth of microchannel in (m)
depthc=870E-6; %depth of minichannel in (m)
Ap=((10.16/100)*(W)); %7 MAY NOT BE RIGHT MEASURE P_PLATE LENGTH
Estimate of surface area (L*W) [m^2] of porous plate in contact with
gas/liquid
Ax=(depth)*(W);  %Estimate of microchannel cross sectional area (m^2)
Am=(depthc)*(W); %cross sectional area of cooling minichannel
Ahx=(L)*(W);%Bottom surface area of channel for heat exchange with
coolant
N=100; %number of control volumes
dAhx=Ahx/N;
Dhs=(4*Ax)/((2*(depth))+(2*W)); %hydrualic diamter of microchannel
(m)
Dhc=(4*Am)/((2*(depthc))+(2*W)); %hydrualic diamter of minichannel
(m)
t=(((.125*2.54)/100)-(depth)); %thickness of stainless steel
sperating coolant from solution side (m)
dz=(L)/N;       %control volume length in (m) for N cv's
mwsi=10;%weak solution flow rate (g/min)
mws=mwsi/60000; %mass flow of solution entering absorber (kg/s)
mc=268.5/60000; %mass flowrate of the cooling water (kg/s)
Xs=0.15; %inlet mass fraction of ammonia in solution
Xv=0.99; %mass fraction of ammonia in inlet gas stream
kaves=0.4628; %(W/m^2-K) average k between pure ammonia and water
(using mass averaging) for range of temps (20-50C)
kavec=0.585; %Estimate of k for water at 10C.
kss=16; %Estimate of stainless steel thermal conductivity (W/m-k)
Cpavec=4187; %Estimate of cooling water at 10C J/kg-K (EES)
rhoc=1000;   %denisty of coolant water(kg/m^3)

for i=1:L/dz
        trackX(i)=Xs;
```

```
        trackmws(i)=mws;

        %MASS and Concentration Calcs.:
        Z=dz*i;
        trackZ(i)=Z;
        rho=density(P,(Tsi+Tso)/2,Xs);%uses property estimation
subroutine to find density of the ammonia/water mixture
        rhos(i)=rho;
        Us(i)=mws/(rho*Ax); %velocity of solution
        Uc(i)=mc/(rhoc*Am); %velocity of coolant
        dma=(mv/Ap)*(1.905/100)*dz;%ammonia absorbed (assuming
instant absorption for this case mv,CV=dma) into a control volume
(kg/s)
        if Z>0.1016
            dma=0; %This stops mass flow of vapor from porous plate
at a certain point Z in the channel, in this case, the entire length
of the channel is used
        end
        mss=(mws)+dma; %mass flow of solution exiting CV
        Xs=((mws*Xs)+(dma*Xv))/(mss); %concentration prediction

         %Other Thermo Properties and coefficients required:
         MW1=17;     %   Ammonia molecular weight
         MW2=18;     %   Water molecular weight
         MW=1/((Xs/MW1) + ((1-Xs)/MW2)); %molecular wieght of the
mixture
         x=(Xs/MW1)*MW; %mol fraction
         x2(i)=x;%track mol fraction for later
         mws2(i)=mws; %indexing mws for later use
         mws=mss;
         X2(i)=Xs;
         mss2(i)=mss; %just indexing mss for later use
         dma2(i)=dma; %just indexing dma for later use
         x2(i)=x; %just indexing x for later use
         MW3(i)=MW; %just indexing MW for later use
         p=P/10; %non-dimensional pressure
         tv=Tv/100; %non-dimensional temp
         hv=(Hmg(Xv,p,tv)*8.314*100*(1/17))*1000;% ammonia gas (J/kg)

         qgen(i)=(dma*hv)/(W*dz*depth); %(W/m^3) (volumetric
generation of heat)
         As(i)=rhos(i)*Us(i);%rhos(i)*TrackCps(i)*Us(i); %This is a
coefficient in the solution discretization
         Ac(i)=rhoc*Cpavec*Uc(i); %This is a coefficient in the
coolant discretization
         i=i+1;

end
```

PART II:

```
clear
%This code uses values obtained from PART I to compute the
temperature profiles for the solution and coolant sides of an
ammonia-water bubble absorber. Jenks 3.01.07
tic
Proj575A
Ts(1)=295; %Known inlet solution temp (marching forward in space)
inlet to outlet
%@Ts(2)=Ts(1); %FIX this
Tc(1)=283.6; %This is the coolant exit temp initial guess (marching
backward in space) outlet to inlet (in counterflow w/ solution side)
%@Tc(2)=Tc(1) %FIX this
ts(1)=Ts(1)/100;
%@ts(2)=Ts(2)/100;
hs(1)=(Hmf(x2(1),p,ts(1))*8.314*100*(1/MW3(1)))*1000;%J/kg
%@hs(2)=(Hmf(x2(2),p,ts(2))*8.314*100*(1/MW3(2)))*1000;
Nus=5.39; %Nusselt number from Incropera Heat and Mass Transfer 5th
ed.
Nuc=5.39;
diff_Tc=1; %initializing convergence criterion
error=.05; %alowable error in Tc outlet
while diff_Tc>error %convergence criterion
    for j=1:N-1
        ts=Ts(j)/100; %average non-dim temperature solution side
        Cpnh3=(Cp(1,ts)*8.314*(1/17))*1000; %specific heat of pure
liquid ammonia J/kg-K
        Cph20=(Cp(2,ts)*8.314*(1/18))*1000; %specific heat of pure
water J/kg-K
        Cpaves=(Cpnh3*(trackX(j)))+Cph20*(1-trackX(j)); %mass average
of specific heats J/kg-k
        TrackCps(j)=Cpaves;
        Hs=(Nus*kaves)/Dhs; %solution side convective heat transfer
coef (W/m^2-K)
        Hc=(Nuc*kavec)/Dhc; %coolant convective heat transfer coef
(W/m^2-K)
        U=800;%1/((1/Hs)+(t/kss)+(1/Hc)); %overall Heat transfer
coeff (W/m^2-K)
        dq(j)=(U*(Ts(j)-Tc(j))); %heat removed per cv (W/m^2)

        %%%DISCRETIZATION%%%%
        hs(j+1)=((((qgen(j)*dz)-
(dq(j)*dz/depth)))+(As(j)*hs(j)))/(As(j+1));
        %hs(j+1)=((dq(j)*dAhx)-(mws2(j)*hs(j))-
(dma2(j)*hv))/(mws2(j+1));
        %Ts(j+1)=(((As(j-1))*Ts(j-1))+(2*((dz*qgen(j))-
(dq(j)))))/(As(j+1)); %Discretization for solution (HOT) side
        qs=(mws2(j)*hs(j))+(dma2(j)*hv)-(mws2(j+1)*hs(j+1));
        %Tc(j+1)=Tc(j)-((dq(j)*dAhx)/(mc*Cpavec));
        Tc(j+1)=(((Ac(j))*Tc(j))-(dq(j)*dz/depthc))/(Ac(j+1));
        %%Discretization for coolant side-->subtracting dq because we
are marching backwards
        H=(hs(j+1))/(8.314*100*(1/MW3(j+1))*1000);
        x=x2(j+1);
        options=optimset('Display','off');
```

```
        Ts(j+1)=100*(fsolve(@(T) (-H+x*(Gif(1,p,T)-T*dGTf(1,p,T))+(1-
x)*(Gif(2,p,T)-T*dGTf(2,p,T))+Gex(x,p,T)-T*dGTe(x,p,T)),1,options));

        delta_T(j)=Ts(j)-Tc(j);%For comparison with an exact solution

    end
    %To achieve convergence, must alter the guessed coolant outlet
temp: Tc(1)
    dif_Tc=(Tci-Tc(N));
    if dif_Tc>0
        Tc(1)=Tc(1)+.03;
        %Tc(2)=Tc(1);
    end
    if dif_Tc<0
        Tc(1)=Tc(1)-.03;
        %Tc(2)=Tc(1);
    end
    diff_Tc=abs(Tci-Tc(N));
end
    %delta_TexactB(1)=Ts(1)-Tc(1);
    for k=1:N-1
        %Exact solution based on modified HX analysis:
        s_dot=mv*hv; %source term estimation (not including hws)
(generation) in W
        A=(s_dot)/(L*mws2(k)*TrackCps(k));
        B=U*W*((1/(mws2(k)*TrackCps(k)))-(1/(mc*Cpavec)));
        delta_Texact(k)=(A/B)+(((Ts(1)-Tc(1))-(A/B))*exp(-
B*trackZ(k)));
        %Exact Solution without source term (incropera):
        delta_TexactB(k)=(Ts(1)-Tc(1))*(exp((-
U*trackZ(k)*W)*((1/(mws2(k)*TrackCps(k)))-(1/(mc*Cpavec)))));
    end
qc=mc*Cpavec*(Tc(1)-Tc(N))
qs=(mws2(1)*hs(1))+(mv*hv)-(mws2(N)*hs(N))
qs2=sum(dq)*dAhx

toc
```